A New Hybrid Lattice-Tweezer Experiment for Quantum Simulation with Ytterbium Atoms

Charles Etienne Staub

München 2024

A New Hybrid Lattice-Tweezer Experiment for Quantum Simulation with Ytterbium Atoms

Dissertation an der Fakultät für Physik
Ludwig-Maximilians-Universität München

vorgelegt von

Charles Etienne Staub

aus Göttingen

München, den 8. Mai 2024

Tag der mündlichen Prüfung: 20. Juni 2024
Erstgutachterin: Prof. Monika Aidelsburger
Zweitgutachter: Prof. Adam Kaufman
Weitere Prüfungskommissionsmitglieder: Prof. Dmitri Efetov, Prof. Jan von Delft

Zusammenfassung

Diese Arbeit dokumentiert den Aufbau eines neuen Experiments zur Quantensimulation mit kalten Ytterbium Atomen. Das entscheidende Merkmal dieses Experiments ist das Vorhandensein sowohl eines optischen Gitters als auch eines Tweezer-Arrays. Die Quantensimulation mit ultrakalten Atomen hat sich im Laufe der letzten Jahre rasant weiterentwickelt. Angeregt durch neue Fragen der Quantenvielteilchenphysik und in Anbetracht des Potenzials für die Entwicklung von Quantencomputern mit neutralen Atomen, haben diese Experimente versucht, eine immer präzisierere Kontrolle über die atomaren Freiheitsgrade zu erlangen. In diesem Zusammenhang haben sich zwei komplementäre Ansätze entwickelt. Optische Gitter haben sich als äußerst erfolgreich erwiesen, um große, defektfreie Systeme aus kalten Atomen herzustellen, während Tweezer Arrays ein enormes Maß an lokaler Kontrolle ermöglichen, da sie einzelne Atome einfangen und anordnen können. Der hybride Ansatz zum Aufbau eines Quantensimulators, der in dieser Arbeit verfolgt wird, vereint die Vorteile dieser beiden komplementären Ansätze.

Ytterbium hat für diese neuen Ansätze der Quantensimulation zunehmend an Bedeutung gewonnen- vor allem aufgrund seiner komplexen Energieniveaustruktur. Sein ultra-schmaler Uhrenübergang wird für den Bau der weltweit präzisesten Atomuhren verwendet, während seine Kernspin-Freiheitsgrade sowohl zur Entwicklung von Wechselwirkungen mit einzigartigen Symmetrieeigenschaften verwendet werden als auch um robuste Qubits für Quantencomputer zu erzeugen. In unserem Experiment haben wir den vorhandenen Werkzeugkasten für die Quantensimulation mit Ytterbium erweitert, indem wir zwei neue magische Wellenlängen für den Grundzustand ($^1S_0$) und den metastabilen angeregten Zustand ($^3P_0$) des ultra-schmalen Uhrenübergangs gemessen haben. Gleichzeitig haben wir die Tune-out Wellenlänge für den Grundzustand dieses Übergangs gemessen sowie auch den Wert der Polarisierbarkeit des angeregten Zustands bei dieser Wellenlänge bestimmt.

Diese Wellenlängen ermöglichen neue zustandsabhängige Adressierungs- und Präparationsschemata, insbesondere im Rahmen eines hybriden Ansatzes zur Quantensimulation. Ein besonders interessanter Anwendungsfall ist die Simulation von Gittereichtheorien. Hier ist eine sehr genaue Abstimmbarkeit nötig, um lokal eichinvariante Wechselwirkungen zwischen Eich- und Materiefreiheitsgraden zu implementieren, die durch die Grund und Anregungszustände des Uhrenübergangs kodiert werden können. Diese Arbeit endet mit einer Übersicht der Möglichkeiten, die sich in diesem Zusammenhang durch unser Gitter-Tweezer-Experiment bieten.

Abstract

This thesis documents the construction of a new experiment for quantum simulation with cold ytterbium atoms. The defining feature of this experiment is the presence of both an optical lattice and a tweezer array. Quantum simulation with ultracold atoms has, in recent years, advanced at a rapid pace. Inspired by new questions in quantum many-body physics and the potential for quantum computing with neutral atoms, these experiments have sought to obtain an ever greater degree of control over the atomic degrees of freedom. In this context, two complementary approaches have emerged. Optical lattices have been immensely successful at creating large, defect-free systems of cold atoms, while tweezer arrays afford an enormous degree of local control by being able to trap and arrange individual atoms. The hybrid approach to building a quantum simulator pursued in this thesis brings together the benefits of both of these complementary approaches.

Ytterbium has become increasingly important to these new approaches in quantum simulation - in large part due to its intricate level structure. Its ultra-narrow clock transition has been used to build the world's most precise atomic clocks, while its nuclear spin degrees of freedom can be used to engineer interactions with unique symmetry properties or to realize robust qubits for quantum computing. In our experiment, we have expanded this ytterbium toolbox by measuring two new magic wavelengths for the ground ($^1S_0$) and metastable excited state ($^3P_0$) of the ultra-narrow clock transition. At the same time we also measured the tune-out wavelength for the ground state of this transition and determine the value of the excited state polarizability at this wavelength.

These wavelengths provide the opportunity for new state-dependent addressing and preparation schemes, particularly within a hybrid approach to quantum simulation. One particularly intriguing use-case lies in the simulation of lattice gauge theories. Here, tremendous tunability is required to implement locally gauge invariant interactions between gauge and matter degrees of freedom, which can be encoded using the ground and excited states of the clock transition. This thesis ends by exploring the possibilities afforded in this context by our lattice-tweezer experiment.

Contents

Introduction

This thesis is concerned with the interaction of light and matter on very small scales and at very low temperatures. To give some intuition for just how cold, we briefly consider the following examples: The coldest temperature ever recorded on earth was measured at −89.2°C, or 184 K, in the year 1983 at a Soviet research station in Antarctica [1]. This is positively mild when compared to the 77 K at which nitrogen liquifies or the 10 K that characterize interstellar space. Far below even these frigid temperatures, we reach the μK, or even nK, that are routinely achieved in experiments with cold atoms, such as the one described in this thesis. What necessitates these cold temperatures?

Ground-breaking research over the past two decades has found that dilute gases of alkali or alkaline-earth-like (AEL) atoms such as rubidium (Rb) or ytterbium (Yb), when cooled to these extreme temperatures, can be made to exhibit behavior mimicking or *simulating* that of an enormous variety of different physical settings [2]. This includes everything from the electrical properties of solid state materials such as insulators and semi-conductors [3] to the kind of fundamental processes encountered in high-energy particle physics [4–6]. Furthermore, these ultracold gases themselves exhibit interesting behavior that lacks any classical counterpart [7]. The great ambition of cold atom quantum simulators is therefore to offer a deeper understanding into existing, often times, numerically intractible problems of modern physics, as well as to enable new insights into the properly quantum mechanical behavior of many-body systems. This ambition has animated physicists to develop a large number of experimental tools to probe and control these ultracold quantum gases. It is the aim of this thesis to combine a number of these existing tools and develop some new ones to help further this ambition of quantum simulation.

The majority of the experimental tools developed in this context rely on the interaction of laser light with atoms. This kind of light can, for example, be used to cool atoms by scattering photons of the right frequency [8]. It is a basic insight of thermodynamics that the temperature of an object is related to the internal motion of its constituent atoms and molecules [9]. The more energetic the motion, the hotter the object. Laser cooling works to slow down this motion, reducing the temperature of atoms with every scattered photon. Laser light can also be used to trap these atoms once they are cold [10]. In this regard, the two most relevant experimental tools for our thesis are optical lattices [11, 12] and optical tweezer arrays [13].

Optical lattices are created by interfering laser beams to generate a periodic, standing-wave potential. Depending on the lattice wavelength, individual atoms can occupy either the peaks or troughs of this potential, leading to large, defect-free and homogeneous arrays of ultracold atoms, each separated from its neighbor by no more than a few hundred nanometers. The

interaction and tunneling of atoms in this lattice can be precisely tuned by, for example, adjusting the power of the lattice lasers or by the influence of an external magnetic field [14]. Various regular geometries (such as square, triangular, hexagonal and Kagome) can be achieved by the correct alignment and the right number of lattice beams. With such clean and controllable systems it becomes possible to perform the kind of quantum simulation motivated at the outset of this introduction [2, 3, 15–19]. A paradigmatic model commonly used for this purpose is the Hubbard model [20, 21]. It can be implemented in optical lattices to investigate metal-insulator transitions [15, 22], magnetic ordering [23–25] and superconductivity [26]. Beyond the Hubbard model, cold atoms in optical lattices can also offer insights into the nature of topologically non-trivial quantum many-body systems [7, 27]. Much of this research has been spurred on by the ability to resolve individual atoms at the level of single lattice sites using high numerical aperture objectives [28–35]. This has allowed physicists to probe observables hard to access on other experimental platforms, such as full counting statistics and multi-point correlation functions [36–40]. In combination with AEL atoms, optical lattices have even been used in metrology to engineer the world's most precise atomic clocks [41, 42].

Optical tweezers present an alternative to the large-scale and comprehensive optical lattice approach, by trapping indiviual atoms in tightly focused laser light [43–45]. These tweezers can be arranged into arrays of arbitrary geometries [46, 47] and dynamically re-sorted within less than a second [48–51], making for an extremely versatile and flexible platform. These arrays can be combined with highly-excited Rydberg states to engineer controllable, long-range interactions [52–57]. In recent years, this has acted as a major catalyst for new directions in quantum simulation [58–60], quantum metrology [61–63] and quantum computing with neutral atoms [64–74]. Here, the recent addition of AEL atoms [44, 45, 75] has also granted new opportunities. These atoms permit different kinds of qubits, some with excellent isolation from environmental perturbations and long coherence times [66, 67, 70, 71]. This is particularly important given the pressing challenges faced by neutral atom quantum computers regarding the fidelity and scalability of logical operations. Current research is strongly focused on the development of real-time error correction, as well as strategies for mitigating dissipation and losses [68, 72, 73]. One decisive drawback to tweezer arrays is the lack of tunneling dynamics. This makes it fundamentally ill-suited to simulating Fermi-Hubbard type physics.

To supplement these two approaches of optical lattices and tweezer arrays, this thesis will investigate the state-dependent control of Yb. State-dependent control describes the ability to engineer potentials which independently manipulate and control atoms depending on their internal states. To date, this ability has been exploited to facilitate new cooling and state preparation schemes [76–78], simulate out-of-equilibrium dynamics [79–83], investigate strongly coupled quantum emitters [84] and to realize neutral atom quantum computing protocols [51, 85–88]. In Yb, the ground and long-lived metastable excited state of the clock transition pose a particularly intruiging pair of states for this purpose. In combination with optical lattices and tweezer arrays, these state-dependent potentials can be used to extend the ability of quantum simulators to prepare tailored initial states and engineer complex interactions. Together, these elements allow for lines of research that have previously remained underexplored due to their high degree of experimental complexity. One example of interest is the simulation of lattice gauge theories (LGT) [4], which represent discretized versions of continuous gauge theories,

such as those familiar from classical electrodynamics and quantum field theory. LGTs are particularly intriguing because they provide a powerful framework for studying phenomena in particle physics that are difficult to capture using conventional perturbative methods. A prime example of such a phenomenon is quark confinement, where quarks are bound together to form hadrons (e.g., protons and neutrons), and cannot be isolated as free particles [4]. This non-perturbative behavior is crucial for understanding the fundamental interactions described by quantum chromodynamics (QCD), the gauge theory underlying the strong nuclear force. Beyond particle physics, LGTs have deep connections to open questions in the study of many-body quantum systems, particularly concerning their thermalization properties [89, 90].

This thesis

In this thesis, we present a new quantum simulation experiment with cold ytterbium atoms combining optical lattices and tweezer arrays in a hybrid platform. In so doing we develop a compact experimental apparatus featuring long vacuum lifetimes, flexible magnetic field control and sub-second cycle times. The last of these elements offers a marked improvement over cycle times of traditional ultracold atom experiments, which can run on the order of several (tens) of seconds. This enables us to collect significantly more data within a given timeframe, thus improving the statisical significance of our results. Furthermore, it facilitates the reduction of errors arising due to longer timescale drifts in the experimental apparatus. Within these short cycle times, we demonstrate the fast and efficient loading of ytterbium atoms into a magneto-optical trap (MOT) and subsequent transfer into either an optical lattice or a tweezer array. We show the ability to cool atoms in our optical lattice as well as our tweezer array and verify the trapping of individual atoms in the latter. To probe our atoms, we implement a number of imaging and spectroscopic techniques.

Using this platform, we enlarge the available toolbox for quantum simulation with ytterbium atoms by measuring state-dependent wavelengths for the ground and excited states of the ultranarrow clock transition. We measure two magic wavelengths using high-resolution optical clock spectroscopy. These are wavelengths where the aforementioned states experience the same trapping potential. In addition, we perform the first measurements of the ground state tune-out wavelength by building on a scheme developed by Heinz *et al.* [91].

Lastly, we describe the ability of our hybrid platform to investigate lattice gauge theories (LGTs) in a scheme developed in Surace *et al.* [92] for this precise purpose. We show how the aforementioned state-dependent wavelengths play a crucial role in this scheme and how our experiment is uniquely suited to the simulation of complex LGTs beyond one dimension.

Outline

This thesis proceeds in five chapters:

- In **Chapter 1**, we take a closer look at the quantum simulation toolbox for neutral ytterbium atoms. We present a theoretical discussion of ytterbium's electronic structure,

interactions and the possibility of state-dependent control, as well as a more detailed analysis of optical lattices and tweezer arrays.

- **Chapter 2** then deals with the construction our experimental platform to accomodate these tools. The chapter is divided into major subsystems of the experiment, such as the vacuum chamber, the magnetic field coils or the laser systems. We explain the design philosophy for each subsystem, detail its assembly and describe any tests that were performed to ensure its functionality.

- **Chapter 3** examines a number of experimental methods employed in our experiment. These include different types of imaging schemes as well as a number of spectroscopic and cooling methods. We also characterize our MOT and describe the calibration of our magnetic fields.

- Having established the essentials of our experiment, **Chapter 4** turns to the measurement of state-(in)dependent wavelengths for the ground and excited state of the Yb clock transition. Using spectroscopic methods established in the previous chapter, we measure two magic wavelengths for these states. In addition, we make use of parametric heating in an optical lattice to ascertain the value of the ground state tune-out wavelength. We conclude the chapter by presenting our progress towards a measurement of the excited state tune-out wavelength.

- Finally, **Chapter 5** explores the possibility of simulating lattice gauge theories (LGTs) using our quantum simulation platform. The chapter begins by discussing the essential features of LGTs and then proposes a way in which the state-dependent wavelengths measured in the previous chapter might be combined with our optical lattices and tweezer arrays to simulate quantum electrodynamics (QED) in one and two spatial dimensions. We also offer some perspectives for the simulation of higher-dimensional LGTs and associated phenomena, which are particularly well-suited to our experiment.

Publications

The central results presented in this thesis have been published in the following reference:

- T. O. Höhn*, **E. Staub***, G. Brochier, N. Darkwah Oppong, and M. Aidelsburger, *State-dependent potentials for the $^1S_0$ and $^3P_0$ clock states of neutral ytterbium atoms*, Phys. Rev. A **108**, 053325 (2023)

*These authors contributed equally to this work.

CHAPTER 1

The ytterbium quantum simulation toolbox

In this chapter we take a look into the neutral atom quantum simulation toolbox and examine some of the tools at our disposal. We begin by exploring the electronic properties of the ytterbium atom and motivate its use in our experiment. This will allow us to appreciate how state-dependent potentials can be used to manipulate and control this atomic species (something which we return to in Chapter 4 of this thesis). We then turn to a well-established tool of quantum simulation in a section on optical lattices before concluding this chapter with a discussion of optical tweezer arrays.

1.1 The ytterbium atom

1.1.1 Isotopes

Ytterbium is an rare-earth element, finding its place towards the end of the lanthanide series with an atomic number $Z = 70$. It is naturally occuring in seven stable isotopes, five of which are bosonic [^{168}Yb, ^{170}Yb, ^{172}Yb, ^{174}Yb] and two of which are fermionic [^{171}Yb and ^{173}Yb]. Of these, bosonic ^{174}Yb is the most abundant [94] and is the isotope used throughout the majority of this thesis. Along with its other bosonic counterparts, it is lacking in nuclear spin ($I = 0$) and thus features no hyperfine structure. By contrast, the two fermionic isotopes ^{171}Yb and ^{173}Yb exhibit a non-zero nuclear spin of $I = 1/2$ and $I = 5/2$ respectively. The presence of such a large number of stable isotopes means that ytterbium can be used to create interesting mixtures of different isotopes [95–97].

1.1.2 Electronic structure

At first glance, it may seem odd that an element within this part of the periodic table should be an ideal candidate for ultracold quantum simulation experiments. After all, many of the usual candidates for these type of experiments are found within groups I (alkali atoms) and II (alkaline-earth atoms) of the periodic table. However, just like alkaline-earth atoms, ytterbium features two valence electrons, giving rise to an alkaline-earth-like (AEL) level structure [Fig. 1.1]. The singlet ($S = 0$) and triplet ($S = 1$) configuration of these valence electrons can be exploited for laser cooling, trapping and imaging.

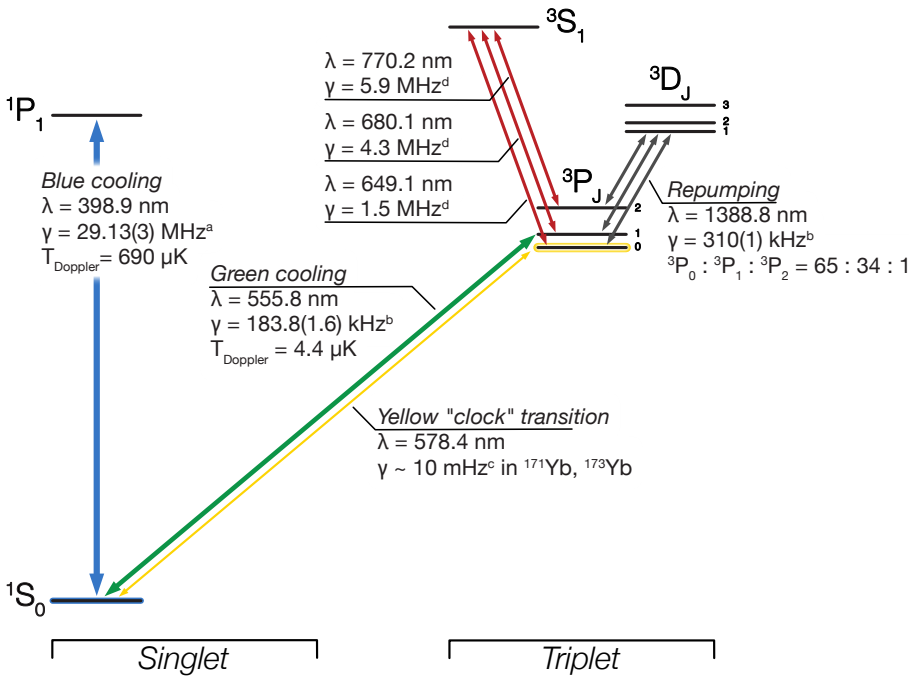

Figure 1.1 | Level diagram of ytterbium. The relevant transitions in our experiment are named and shown with their associated wavelengths λ, and linewidths γ. The blue cooling transition in the singlet manifold is used in our experiment for Zeeman slowing, 2D magneto-optical trapping, cooling and imaging. The green cooling transition is dipole forbidden leading to a narrower linewidth, which exploit to create a low-temperature 3D MOT (Section 3.2). The even narrower yellow clock transition doubly forbidden and used in our experiment for high-resolution atomic spectroscopy (Section 3.3). Values for the spectral properties of each transition are taken from: [a] [98], [b] [99], [c] [100], [d] [101]. The ground and metastable excited state of the clock transition are highlighted in blue and yellow respectively.

Broad blue transition.—Within the singlet manifold, the $^1S_0 \leftrightarrow {}^1P_1$ transition is particularly effective for optical trapping of atoms due to the large radiation force provided by its broad linewidth of $\Gamma = 2\pi \times 29.13\,\mathrm{MHz}$ [98]. In our experiment, we make use of this transition for Zeeman slowing, optical molasses cooling (Section 3.2) and for generating a 2D magneto-optical trap (MOT) to transversely cool and redirect the atomic beam (Section 2.5.1). Its small wavelength of $\lambda = 398.9\,\mathrm{nm}$ [102] makes it particularly well-suited for high resolution optical imaging techniques, while its high scattering rate allows for fast imaging.

Green intercombination transition.—One peculiarity of the AEL level scheme is the existence of narrow intercombination transitions between spin manifolds. These otherwise dipole-forbidden transitions ($\Delta S \neq 0$) are available due to the preponderance of spin-orbit coupling in elements with atomic numbers $Z > 40$, which admixes a small fraction of states from the opposing spin manifold [103]. The first noteworthy transitions in this respect is the $^1S_0 \leftrightarrow {}^3P_1$ transition. Its relatively narrow linewidth of 182.3 kHz [104] is benefical for laser cooling with a Doppler temperature of approximately 4 μK. Still, the transition is broad enough to simultaneously allow for efficient scattering and thus is often used for 3D MOTs of ytterbium, either in a two-stage architecture in combination with the broad blue transition, or by itself, as it the case in our experiment.

Clock transitions.—The second notable set of intercombination transitions are two ultra-narrow transitions from the ground state to the $^3P_0$ and $^3P_2$ states with a linewidth on the order of 10 mHz [100]. The $^1S_0 \leftrightarrow ^3P_0$ clock transition is doubly-forbidden in the sense that it additionally violates the prohibition on $J = 0 \leftrightarrow J' = 0$ transitions. In the fermionic isotopes of ytterbium, only the presence of a non-zero nuclear spin leads to a finite coupling strength for this transition. Here, the hyperfine interaction results in an admixing of the $^3P_1$ state to the $^3P_0$ state. In bosonic ytterbium, the clock transition is completely suppressed and the necessary admixing of $^3P_1$ must be generated using an externally applied magnetic field (see Section 3.3.4 on magnetically induced Rabi spectroscopy). A serendipitous feature of the clock transition is its insensitivity to magnetic fields owing to the lack of total angular momenta in both states of the transition ($\{J, J'\} = 0$). This ensures that the $^1S_0$ and $^3P_0$ nuclear spin manifolds are completely isolated from external magnetic perturbations, making it an ideal candidate for highly sensitive precision spectroscopy and, more recently, for use as a qubit in quantum computing schemes of cold AEL atoms [66, 67, 70, 71]. The decoupling of electronic and nuclear spin degrees of freedom also has important implications for the interaction properties of Yb atoms, which will be discussed in Section 1.1.3. Optical atomic clocks based on ytterbium atoms have exploited these features to attain unprecedented levels of stability and reproducability, with fractional frequency uncertainties at the 10^{-18} level [105–107].

The $^1S_0 \leftrightarrow ^3P_2$ transition is magnetic quadrupole (M2)-allowed and as such, it is permanently accessible, even in bosonic ytterbium. The magnetic sensitivity of this state can be exploited to tune its scattering interactions with the ground state [108] or for single-layer isolation and imaging in quantum gas microscopes using a magnetic field gradient [35, 109, 110]. While this transition has been known in ytterbium for some time [111], it has now also been investigated in strontium (Sr) in recent spectroscopic measurements [112, 113]. In conjunction with its $^3P_0$ counterpart, the $^3P_2$ state has been proposed in the context of quantum computing schemes as an alternative to the nuclear spin qubit discussed above [114]. Experimentally, the control over this qubit poses a significant challenge, since it requires the precise control of two optical frequencies to generate a two-photon Raman transition between the $^3P_0$ and $^3P_2$ state. Despite this difficulty, control over this qubit has recently been demonstrated experimentally, with coherence times on the order of tens of milliseconds and single qubit rotations on the μs level [115, 116].

Repumping transition.—The higher lying triplet D manifold may be used to repump atoms from the long-lived $^3P_0$ and $^3P_2$ states back into the ground state for detection and imaging. In our experiment, we employ the broad $^3P_0 \leftrightarrow ^3D_1$ transition for this purpose, thus allowing us to separately image ground and excited state atomic fraction. Though the $^3D_1$ state has a finite branching ratio into the $^3P_2$ state, this is calculated to be on the percent level [117] and thus negligible compared to the desired decay channels. For completeness, we mention the existence of a finite decay from the $^1P_1$ state into the $^3D_1$ state, though this transition is found to be extremely narrow [101].

1.1.3 Interactions

As we noted in Section 1.1.2, the absence of total electronic angular momentum ($J = 0$) in the $^1S_0$ and $^3P_0$ states leads to the almost complete decoupling of this degree of freedom from the nuclear spin I in these states. As such, the s-wave scattering properties of these states are governed exclusively by the electronic degrees of freedom, independent of the nuclear spin of the participants. This in turn has radical consequences for the interaction dynamics of these states at low energies, since these are now found to be invariant with respect to rotations of the nuclear spin. The latter is governed by the special unitary group SU(N), where $N = 2I + 1$, and thus our interactions are said to be SU(N)-symmetric. More specifically, the interactions are circumscribed by four scattering lengths $a_{gg}, a_{ee}, a_{eg}^{+}, a_{eg}^{-}$ for scattering in the states $|gg\rangle \otimes |s\rangle, |ee\rangle \otimes |s\rangle, (|ge\rangle + |eg\rangle)/\sqrt{2} \otimes |s\rangle, (|ge\rangle - |eg\rangle)/\sqrt{2} \otimes |t\rangle$ where $|s\rangle$ and $|t\rangle$ denote the nuclear spin singlet and triplet respectively [118, 119]. Absent any dependency of these scattering lengths on the nuclear spin, spin-changing collisions are prohibited, a fact which has been confirmed in systems of cold AEAs on experimentally relevant timescales [120–123]. Spin systems of ultracold atoms manifesting SU(N) symmetry play a role in a number of fascinating physical settings [119] and will reappear in Chapter 5 of this thesis, when dealing with lattice gauge theories.

1.2 State-dependent potentials

In this section we show how basic considerations of light-matter interaction provide a recipe for creating state-dependent optical potentials. We also discuss the context in which such potentials have been used in cold atom experiments with a particular focus on the $^1S_0$ and $^3P_0$ states of the Yb clock transition.

1.2.1 Polarizability

Quite generally, we can describe the response of an atom to an external monochromatic electromagnetic field of the form

$$\boldsymbol{E}(\boldsymbol{r}, t) = \boldsymbol{e} E_0(\boldsymbol{r}) e^{-i\omega t} + c.c., \tag{1.1}$$

with polarization $\boldsymbol{e}$ and angular frequency $\omega = 2\pi c/\lambda$, via its ability to induce a dipole moment $\boldsymbol{d}$ (i.e. charge separation) in an atom:

$$\boldsymbol{d} = \alpha \boldsymbol{E}. \tag{1.2}$$

The complex response function α is known as the polarizability and characterizes the strength of the induced dipole moment. This dipole moment in turn, interacts with the external electromagnetic field, giving rise to an interaction potential of the form [10]:

$$V_{ac}(\boldsymbol{r}) = -\frac{1}{2}\langle \boldsymbol{d} \cdot \boldsymbol{E} \rangle = -\frac{1}{2\epsilon_0 c} \mathrm{Re}\,[\alpha]\, I(\boldsymbol{r}). \tag{1.3}$$

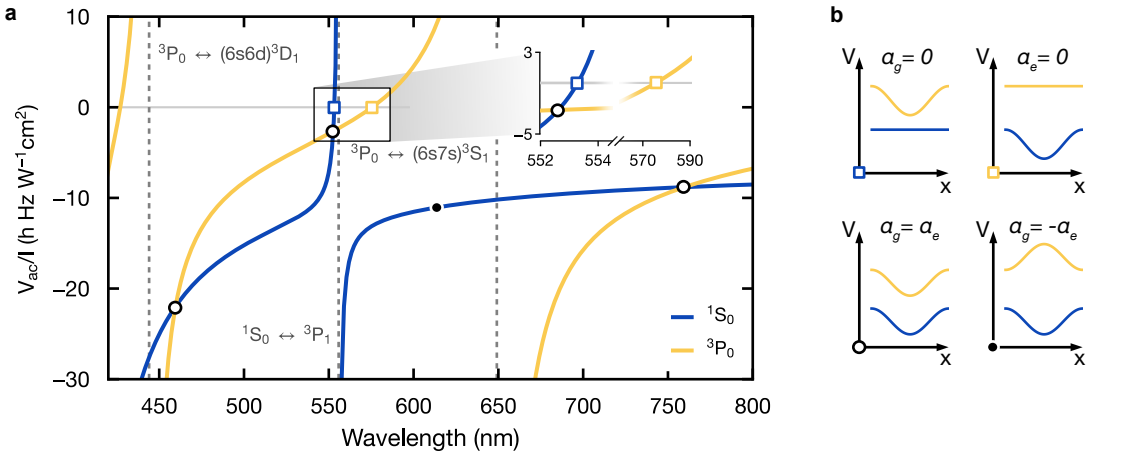

Figure 1.2 | Clock state polarizabilities. (**a**) Wavelength dependecy of the intensity-normalized interaction potential [Eq. (1.3)] for the $^1S_0$ ground state ($|g\rangle$) and $^3P_0$ excited state ($|e\rangle$) of the clock transition, calculated using a simple empirical model (see Section 4.4 for details). We note the presence of several distinct points: empty squares indicate *tune-out wavelengths*, where the scalar polarizability of one state is zero, while the other retains a finite polarizability. The blue and yellow outlines of the points correspond to the $|g\rangle$ and $|e\rangle$ tune-out wavelengths respectively, which reside at $\approx$ 553 nm and $\approx$ 573 nm. Empty circles represent *magic wavelengths*, those where the polarizability of both states is equal in magnitude and sign. Within the plotted wavelength range, magic wavelengths exist close to 459 nm, 553 nm and 759 nm. Conversely, filled circles indicate *anti-magic wavelengths*, with polarizabilities of equal magnitude, but opposite sign. This conditions is met near 619 nm. (**b**) Schematic representation of the potentials $V(x)$ at different state-dependent wavelengths for the states $|g\rangle$ and $|e\rangle$. In clockwise order starting from the top left panel, these are the $|g\rangle$ tune-out, $|e\rangle$ tune-out, anti-magic and magic wavelengths.

Here we make use of the intensity $I = \epsilon_0 c|E_0|^2/2$ and perform a time-average over fast-oscillating terms. In a similar fashion, we can also consider light scattering from the dipole [10]:

$$\Gamma_{\mathrm{sc}}(\boldsymbol{r}) = \frac{1}{\hbar\omega}\langle \dot{\boldsymbol{d}} \cdot \boldsymbol{E}\rangle = \frac{1}{\hbar\epsilon_0 c}\mathrm{Im}\,[\alpha]\, I(\boldsymbol{r}), \tag{1.4}$$

where Γ_{sc} is the scattering rate. It is no accident that the imaginary part of the polarizability gives rise to the dissipative dynamics of the system. This is a consequence of the nature of linear response functions and holds true for a large class of physical processes [124]. The close relation between the reactive [Eq. (1.3)] and the dispersive [Eq. (1.4)] components of the polarizability represents a particular case of the Kramers-Kronig relations [125].

Up to this point, we have made no assumptions regarding the form of the induced dipole moment nor the nature of the polarizability. To apply this discussion to the ytterbium atom in a meaningful way, our description of light-matter interaction must account for a multitude of different atomic transitions, such as those illustrated in the level scheme of the previous section [Fig. 1.1]. This is achieved by considering the polarizability in its most general form as a tensor, which can be expressed as a sum of scalar, vector and tensor components in the following fashion [125–127]:

$$\begin{aligned}\alpha_i(F;\omega) = &\alpha_i^{(s)}(F;\omega) \\ &+ \alpha_i^{(v)}(F;\omega)(i\boldsymbol{E}\times\boldsymbol{E}^*)\cdot\boldsymbol{e}_z\frac{m_F}{F} \\ &+ \alpha_i^{(t)}(F;\omega)\frac{3\left|\boldsymbol{E}\cdot\boldsymbol{e}_z\right|^2-1}{2}\frac{3m_F^2-F(F+1)}{F(2F-1)}.\end{aligned} \tag{1.5}$$

Here i represents the initial state $|i\rangle$ of a given transition and (F, m_F) its corresponding hyperfine and magnetic quantum numbers. In the bosonic isotopes of ytterbium, the lack of a hyperfine structure reduces the complexity of the above expression considerably, eliminating all but the scalar part of the polarizability:

$$\alpha_i^{(s)}(J;\omega) = \sum_{J'\neq J}\frac{2}{3}\frac{\omega_{JJ'}}{\hbar(\omega_{JJ'}^2-\omega^2)}\left|\langle J\|\boldsymbol{d}\|J'\rangle\right|^2, \tag{1.6}$$

summing over all relevant transitions $J \to J'$, where $\omega_{JJ'}$ is the the corresponding transition frequency between fine-structure levels and ω the previously defined angular frequency of the electromagnetic field. Associated to each transition is a reduced dipole matrix element $\langle J\|\boldsymbol{d}\|J'\rangle$. For the $^1\mathrm{S}_0$ ground state ($|g\rangle$), the main contributions to the scalar polarizability stem from the principal blue transition to the $^1\mathrm{P}_1$ state in the spin singlet manifold and the intercombination transition to the $^3\mathrm{P}_1$ state. The $^3\mathrm{P}_0$ excited state ($|e\rangle$) couples to a larger set of higher-lying transitions, thereby complicating the calculation. Furthermore, additional contributions to the polarizability arise from taking into account dipole transitions due to particle-hole excitations from the core [128]. We evaluate Eq. (1.6) over a range of frequencies within the visible spectrum using a number of simplifying assumptions discussed in greater detail in Section 4.4. The resulting intensity normalized potential V_{ac}/I is plotted as a function of the wavelength in Fig. 1.2(a).

1.2.2 State-dependent wavelengths

Within the general trend of each state's polarizability, a number of distinct points deserve our attention.

Magic wavelengths.—Firstly, we note the presence of so-called magic wavelengths where the polarizability of both states is equal in magnitude and sign, i.e. $\alpha_g = \alpha_e$ [indicated by empty circles in Fig. 1.2(a)]. This allows for uniform confinement of ground and excited state in deep optical potentials with vanishing differential ac Stark shift [illustrated schematically in Fig. 1.2(b)]. As such, magic wavelengths are extremely useful for high-precision spectroscopy of the type performed in optical lattice clocks [129–134]. The magic wavelength near 759 nm is particularly well-suited to this kind of application. High amounts of laser power are readily available from commercial laser sources while potential losses from the scattering of trap photons are kept in check by the relatively modest polarizability of each state. We note that for very deep traps, scattering due to two-photon resonances near this magic wavelength lead to non-negligible hyperpolarizability shifts [135, 136]. These are frequency shifts arising from

electric dipole effects scaling with the electric field in fourth order [137] and will resurface in our attempts to measure the excited state tune-out wavelength in Section 4.5. The 759 nm magic wavelength has been investigated experimentally and measured to a high degree of precision for both bosonic and fermionic isotopes of ytterbium [135, 136]. More recently, this wavelength has been employed to trap individual ytterbium atoms in arrays of tightly confined optical tweezers [71, 138]. As part of this thesis, two new and previously unkown magic wavelengths close to 459 nm and 553 nm are investigated and measured (Section 4.1). The first of these is independently corroborated by Norcia *et al.* [139] and used by these authors in a later publication to assemble a target array of nuclear spin qubits for mid-circuit measurements [51]. Of course, magic wavelengths are not limited to the states of the clock transition and experimental work in the domain of quantum computing with ytterbium atoms has made use of magic wavelengths for the $^1S_0$ and $^3P_1$ states of the intercombination transition [51, 67].

Anti-magic wavelengths.—By simply reversing the sign of the magic polarizability condition, we arrive at the anti-magic wavelengths [denoted by a filled circle in Fig. 1.2(a)]. It has been proposed by Yi *et al.* [140] to use the wavelengths to generate sub-wavelength optical lattices and exploit the ensuing accelerated tunneling dynamics for enhanced quantum information applications. Other proposals have suggested anti-magic wavelengths of the ytterbium clock states in the context of artifical gauge fields by combining an anti-magic lattice with an optical superlattice [141].

Tune-out wavelengths.—Last, but not least, we observe a number of zero crossings of the potential for each state. Here, the polarizability of one state vanishes while the other retains a finite polarizability. Wavelengths for which this occurs are known as tune-out wavelengths and allow for state-dependent trapping [142–144] [this is schematically illustrated in the upper two panels of Fig. 1.2(b)]. In alkali atoms, tune-out wavelengths have been investigated experimentally using a number of different techniques including Kapitza-Dirac scattering [145–147], interferometry [148] or modulating schemes [149]. Measurements of tune-out wavelengths in helium have also been used in fundamental tests of quantum electrodynamics [150, 151]. In AEAs these wavelengths are particularly interesting for the two states comprising the clock transition. Here, the long-lived nature of these states, along with the prospect of state-dependent control, has garnered interest in both quantum simulation [152] and quantum computing contexts [153, 154]. Recently, Heinz *et al.* measured the ground-state tune-out wavelength in bosonic ^{88}Sr using a novel modulation scheme relying on parametric heating of a thermal sample of atoms in an optical lattice [91]. This circumvents the need for a degenerate gas and thus considerably reduces the measurement complexity. This method was subsequently used to measure tune-out wavelengths in cold molecules of ^{23}Na^{40}K [155]. During the course of this thesis, we extend this same scheme to ^{174}Yb to perform the first measurement of the ground state tune-out wavelength in this isotope [93](see also Section 4.2). In the final chapter of this thesis, we explain how this tune-out wavelength, together with its excited-state counterpart, can be used to simulate lattice gauge theories in our experiment (Section 5.3).

1.3 Dipole traps and optical arrays

The interaction potential V_{ac} defined in Eq. (1.3) naturally gives rise to a conservative force potential of the form [10]:

$$\boldsymbol{F}(\boldsymbol{r}) = -\boldsymbol{\nabla} V_{ac}(\boldsymbol{r}) = \frac{1}{2\epsilon_0 c}\mathrm{Re}\left[\alpha\right]\boldsymbol{\nabla} I(\boldsymbol{r}). \tag{1.7}$$

This dipole force is proportional to the gradient of the light intensity and can thus be used to optically trap atoms. Dipole traps of this kind are used to great effect to cool atomic samples to degeneracy using a variety of different cooling methods (see Ref. [10] and citations therein). However, early experimental efforts were also conducted into the trapping [43] and cooling [156, 157] of indiviudal atoms in very tightly focused dipole traps known as optical tweezers. In combination with acousto-optic deflectors (AODs), spatial light modulators (SLMs) and digital micromirror devices (DMDs), multiple thousands of these tweezers can be generated and arranged into arbitrary geometries [74, 158]. Furthermore, these devices allow for the dynamical resorting of tweezers which can be used to great effect to generate homogeneously filled, defect-free arrays on short timescales [46, 48, 49]. To harness the full potential of tweezer arrays, long-range distance-dependent interactions, such as those found in Rydberg atoms can be introduced into the arrays. This not only allows for the simulation of interesting many-body Hamiltonians [59, 60, 159], but also the implementation of multi-qubit gates with neutral atoms [73, 160]. In this regard, the trapping of two-valence electron elements in tweezer arrays has only served to extend the available toolbox for quantum simulation and computation with optical tweezers [44, 45]. In our experiment, we will use tune-out tweezer arrays for the $^1\mathrm{S}_0$ and $^3\mathrm{P}_0$ states to realize correlated hopping in an optical lattice. This is a fundamental building block for our planned simulation of lattice gauge theories (see Chapter 5).

The dipole force discussed above can also be used to create optical lattices. These are periodic potentials formed by the interference of two counterpropagating monochromatic laser beams that can be used to trap cold atoms and are a mainstay of modern quantum simulation experiments [3, 15–18, 22]. Optical lattices are an excellent tool for creating large, homogeneous and defect-free systems with tunable tunneling [18]. In our own experiment, we use optical lattices, tuned to the magic wavelength at 759 nm, to perform precision spectroscopy and cool atoms below the Doppler limit (see Section 3.3). Optical lattices also constitute a fundamental part of our proposed simulation of lattice gauge theories where more complex potential landscapes need to be manufactured using a combination of different lattice configurations (Section 5.3.1).

Assuming a Gaussian intensity profile for the lattice lasers, the lattice potential takes the following form [3]:

$$V(r,z) \approx -V_{ac} e^{-2r^2/w(z)^2}\cos^2(kz), \tag{1.8}$$

where (r,z) are radial and axial coordinates, V_{ac} determines the trap depth, $w(z)$ is the $1/e^2$ radius of the beam and $k = 2\pi/\lambda$ is its wavenumber. The intensity profile of our laser beam results in a tight confinement along the axial direction with a oscillation frequency $\omega_z = \hbar k\sqrt{2V_{ac}/m}$. Additionally, confinement is also present in the radial direction. Here, the

oscillation frequency is given by $\omega_r = \sqrt{4V_{ac}/(mw_0^2)}$. A natural energy scale for relating these trapping frequencies to the atoms in the lattice is the recoil energy $E_R = \hbar^2 k^2/(2m)$. At our optical lattice wavelength of 759 nm, the recoil frequency is $\nu_R \approx 2\,\mathrm{kHz}$.

CHAPTER 2

Experimental apparatus

In the preceeding chapter, we explored some of the tools available to modern physicists working on cold atom quantum simulation experiments. Here, we show how our experiment is designed and built to incorporate many of these tools in order to create a powerful and flexible simulation platform. This involves the use of techniques from vacuum engineering, laser optics, control theory and electronics. Each section of this chapter deals with a particular aspect of our experiment, its design, construction and testing.

2.1 Vacuum system

A good vacuum is an essential precondition for trapping cold atoms. The better the quality of the vacuum, the fewer the collisions between cold trapped atoms and any residual background gases. Consequently, a better vacuum results in longer trap lifetimes. To achieve the extremely low pressures necessary for quantum gas experiments, special chambers need to be constructed. In the following, we describe the design and performance of the vacuum system used in our experiment to achieve ultra-high-vacuum (UHV) pressures in the low 10^{-11} mbar range.

2.1.1 Atom source

We employ a comercial atom source[1] to generate a collimated beam of ytterbium atoms. This is the first such atom source manufactured for ytterbium by AOSense. The atomic sample is heated in an oven and initially collimated via a microcapillary array nozzle. We control the temperature of our oven using a commercial temperature controller[2]. We find that for day-to-day operation of the experiment, an oven temperature of 420°C is sufficient to generate an acceptable atomic flux in our glass cell. To confirm the oven flux is as intended, we perform absorption spectroscopy by interrogating the atomic beam transversely to its propagation directon using a weak probe beam, as shown in Fig. 2.1(a). We scan the probe beam frequency across the blue $^1S_0 \rightarrow {}^1P_1$ transition and measure the resulting transmission on an amplified photodetector[3]. The probe beam intensity is kept much smaller than the saturation intensity

[1] AOSense Yb Beam RevC
[2] SRS - PTC10 with PTC320 thermistor and PTC440 TEC modules
[3] Thorlabs PDA36A2

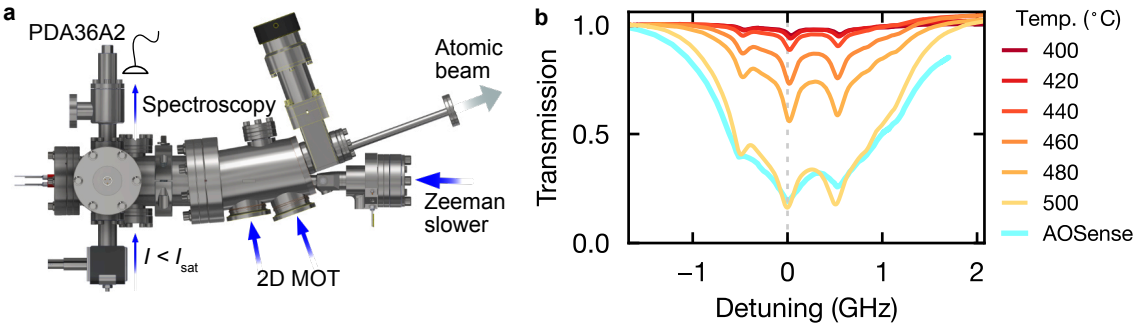

Figure 2.1 | Atom source and spectroscopy. (**a**) Top view of the AOSense Yb Beam RevC atom source with the relevant beams indicated. A collimated atomic beam is generated by an oven heated to 420°C. An in-vacuum permanent magnet Zeeman slower slows the atoms before they are transversely cooled and re-directed by a 2D MOT. We perform absorption spectroscopy on the atomic beam exiting the oven. (**b**) Normalized transmission from absorption spectroscopy as a function of the detuning from the ^{174}Yb $^1S_0 \rightarrow {}^1P_1$ resonance. The transmitted light is collected on an amplified photodetector (Thorlabs PDA36A2). The individual peaks correspond to different isotopes of ytterbium, with peak prominence determined by their respective natural abundances. At 500°C we find good agreement between our measurement and a dataset provided to us by AOSense.

of the transition to avoid having to deal with high intensity corrections. A comparison of our data with a dataset from AOSense at 500°C yields good agreement [Fig. 2.1(b)]. Unfortunately, the nozzle of our oven has clogged twice, necessitating two oven swaps. For further details, we refer the reader to Appendix A.

After exiting the oven, the atomic beam is slowed using a compact in-vacuum permanent magnet Zeeman slower. Our Zeeman slower light is detuned by −590 MHz from the ^{174}Yb $^1S_0 \rightarrow {}^1P_1$ resonance transition frequency. The beam has a $1/e^2$ waist of $w \approx 3$ mm, runs at $\approx$ 300 mW and is incident on a viewport heated to 360°C using the PTC10 controller. Subsequently, the atomic beam is further collimated, transversely cooled and diverted onto the main axis of our vacuum system using a 2D magneto-optical trap (MOT). For this purpose, we use two elliptically shaped beams ($w_{\mathrm{maj}} \approx 15$ mm, $w_{\mathrm{min}} \approx 2.5$ mm), detuned by −30 MHz from the same transition as the Zeeman slower and operating at $\approx$ 15 mW each.

2.1.2 Differential pumping

A two-stage differential pumping design guarantees that the pressure in the glass cell remains in the UHV range even when the temperature in the oven is increased and the pressure in that part of the vacuum system rises. Differential pumping works by using long and narrow tubes to interconnect different parts of the vacuum system with dissimilar pressures. The long mean free path of molecules at UHV ensures that given sufficient pumping speeds, the differing pressures in each part of the system are maintained at equilibrium. In our system, the first stage comprises a long tube of diameter $d = 6$ mm and length $l = 113$ mm in conjunction with an *SAES Z200* pump. This is followed by a second stage of dimension $d \times l = 6\,\mathrm{mm} \times 50\,\mathrm{mm}$ and an *SAES D500* pump. The pumps were chosen for their compactness, allowing us to place them close to the center of the vacuum chamber, thereby mitgating the effect of pipe conductance on the pumping speed.

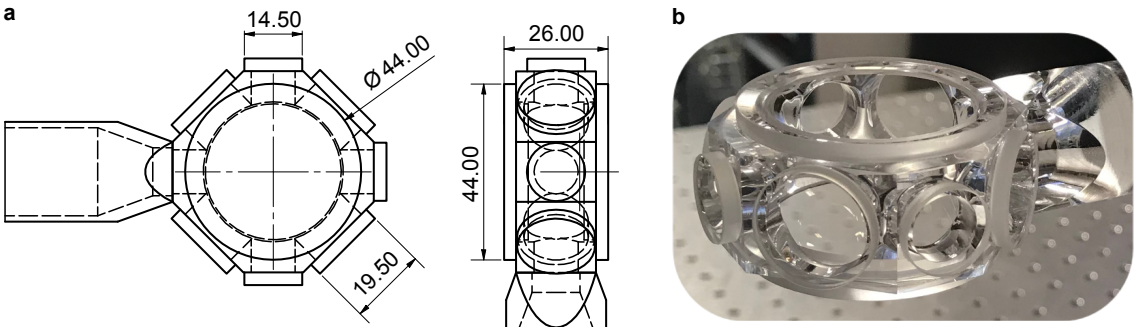

Figure 2.2 | **Glass cell.** (**a**) Technical drawing of our glass cell showing the diameter of the the different viewports attached to our cell. The large ⌀44.00 mm viewports are chosen to accomodate our tweezer arrays and imaging of the atoms, and are stepped to minimize viewport warping. The ⌀19.50 mm viewports are large enough to transmit our 3D MOT beams which have a $1/e^2$ diameter of 10 mm. (**b**) Image of our glass cell as mounted in the experiment. A random anti-reflection (RAR) nano-texture is etched into both sides of each viewport to minimize backreflections. The octagonal frame is made from UV grade fused silica. This frame is attached to a CF40 flange via a pyrex tube.

By purely considering the conductances of long pipes $C = \pi\langle v\rangle\frac{d^3}{l}$ (where $\langle v\rangle$ is the mean velocity of gas) and scaling the pumping speeds accordingly, we calculate a reduction of four orders of magnitude in pressure across our vacuum system using this geometry. Given a maximum atomic source pressure of 1×10^{-8} mbar as specified by AOSense, this would result in a glass cell pressure in the low 10^{-12} mbar. Of course, this does not take into account any outgassing effects whatsoever and indeed, the actual pressure measured using our hot-cathode gauge[4] close to the glass cell is higher, at around 3×10^{-11} mbar.

2.1.3 Glass cell

Our glass cell[5] is composed of several double-side random anti-reflection (RAR) nano-textured viewports[6] frit-bonded to an octagonal UV grade fused silica frame. This frame is bonded to a pyrex cylinder which is attached to a CF40 stainless steel flange. Nano-texturing is a technique involving the etching of randomly distributed sub-wavelength microstructures into the surface of the viewports. These structures ensure a gradual change in the refractive index of the glass through the surface layer, leading to destructive interference in the reflectance across a wide range of wavelengths and angles of incidence [161, 162]. The side viewports of the octagonal frame are of diameter ⌀14.5 mm and ⌀19.5 mm, assembled in an alternating fashion around the cell. The ⌀19.5 mm were chosen to accomodate, amongst others, our 3D MOT beams, which have a $1/e^2$ diameter of 10 mm. These viewports are specified to a flatness of $\lambda/10$, a parallelism of < 5 arcsec and a scratch/dig ratio of 10/5. The top and bottom viewports are stepped with a major and minor diameter of 44 mm and 34 mm respectively, as well as precisely determined thickness. This geometry was chosen to minimize potential warping of the viewports which could lead to optical aberrations.

[4] Edwards Vacuum IG40 EX
[5] Precision Glassblowing
[6] Substrates manufactured by LaserComponents with coating by TelAztec

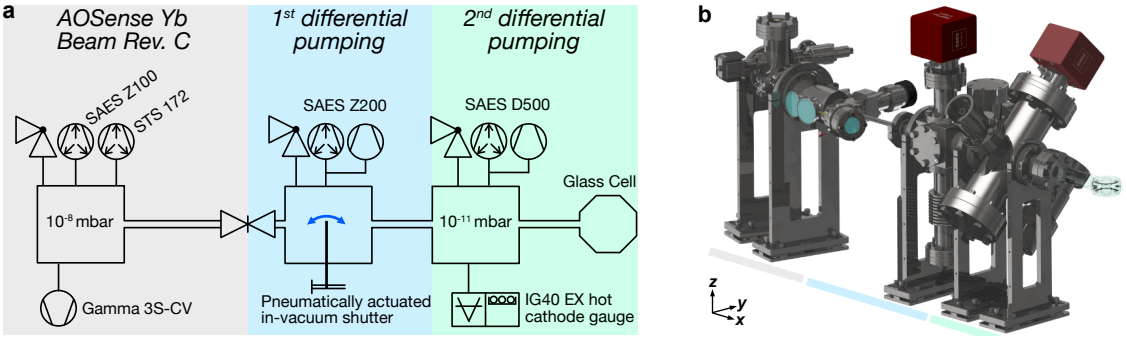

Figure 2.3 | **Vacuum system.** (**a**) Schematic of our vacuum system showing the relevant sections with the corresponding pressures and vacuum pumps. The system consists of an oven followed by two differential pumping sections with the purpose of maintaining a constant pressure in the glass cell. The first differential pumping section features a pneumatically actuated in-vacuum shutter. In practice, this is kept constantly open while we only use the 2D MOT light for shuttering the oven flux on and off. The pressure in the system is continuously monitored using a hot-cathode gauge. (**b**) Render of the vacuum system as it appears in the lab, with the relevant sections highlighted the corresponding colors from (**a**.)

2.1.4 Material considerations

The majority of our vacuum system is constructed from 316LN-ESR stainless steel, which was chosen for its outgassing properties, the ready availability of standard components and its low magnetic permeability of < 1.005. The latter is an important factor in the reduction of eddy currents induced by the switching of magnetic field coils in our experiment (see Section 2.2). The individual components were ordered from *VACOM* and specified to an outgassing rate of $< 1 \times 10^{-13}\,\mathrm{mbar\,L\,s^{-1}\,cm^{-2}}$. We also considered aluminium and titanium due to their favorable outgassing properties and even smaller magnetic permeability. However, both cost and lead times prevented us from pursuing these options further. Another option to reduce the outgassing of our vacuum system would have been to vacuum fire our stainless steel parts at 950°C prior to assembly.

2.1.5 Outgassing

A vacuum system can essentially be regarded as a collection of sources and sinks for gas loads contained therein. Sources of gas loads include: the inital gas load present at atmopsheric pressure, process gas loads (e.g. helium introduced into the chamber during a leak check), outgassing and leaks. To counteract the effect of these gas loads, vacuum pumps are required to serve as gas load sinks in the chamber. Depending on the pressure range and the type of gases present, a variety of different vacuum pumps are required to achieve the desired pressure. Within UHV chambers, outgassing is oftentimes the limiting factor to achieving a low pressure.

Outgassing describes the release or transport of gas molecules from within or through a material. Broadly speaking, it can be divided into three distinct categories:

- *Desorption* - The release of gas molecules from the surface of a material.
- *Diffusion* - The release of gas molecules from within the bulk of the material.
- *Permeation* - The transport of gas molecules through a material.

A schematic illustration of these processes is provided in Fig. 2.4(b).

Desorption.—Depending on the type of the material and its treatment during the manufacturing process, different types of molecules can acrue on its surface. To break the physical or chemical bonds binding these molecules to the surface, an activation energy E_{des} is required. A large class of desorption processes are captured by the Arrhenius equation, where the rate of molecules desorbing from a surface is given by [163]:

$$j_{\text{des}} = \nu_0 \tilde{n} e^{-E_{\text{des}}/RT}. \tag{2.1}$$

Here, $\nu_0 \approx 10^{13}\,\text{s}^{-1}$ is the oscillation frequency of molecules at room temperature, $\tilde{n} \approx 10^{15}\,\text{cm}^{-2}$ is the densest monomolecular packing of a square centimeter of a given surface and $\text{R} \approx 8.314\,\text{J K mol}^{-1}$ is the universal gas constant. In practice, the rate of desorption has been found to scale polynomially with time i.e $j_{\text{des}} \propto t^{-n}$ [164], where n is a scaling constant.

Diffusion.—Diffusion is the release of gas molecules from within the bulk of a material. This process is governed by Fick's laws of diffusion [165]:

$$j_{\text{diff}} = -D\frac{dn_L}{dx} \tag{2.2}$$

$$\frac{\partial n_L}{\partial t} = D\frac{\partial^2 n_L}{\partial x^2}, \tag{2.3}$$

where j_{diff} is the rate of diffusion, n_L is the concentration of gas molecules in the bulk and D is a material dependent diffusion constant which is exponentially decaying with decreasing temperature. The first law expresses the notion that gas trapped within the bulk will propagate from areas of high concentration to those of low concentration across a concentration gradient. The second law is the well-known diffusion equation and describes the density fluctuations of the gas as it undergoes diffusion. General solutions to these equations exist under certain well-defined boundary conditions. A reasonable assumption, which is often borne out in practice, is that the rate of desorption is much faster than the rate of diffusion, $j_{\text{des}} \ll j_{\text{diff}}$. Consequently, for a material of thickness $2d$, the density at the surfaces is vanishing, i.e. $n_L(\pm d) = 0$. Defining an initial concentration $n_L(x, t = 0) =: n_{L0}$, a general solution to the above equations takes the form:

$$j_{\text{diff}}(x = \pm d) = \frac{2D}{d} n_{L0} \sum_{i=0}^{\infty} e^{-\frac{(2i+1)^2\pi^2 Dt}{4d^2}}. \tag{2.4}$$

Notably, the characteristic time constant of diffusion $\tau_{\text{diff}} = 4d^2/\pi^2 D$ scales exponentially with temperature. At room tempertature τ_{diff} is many orders of magnitude larger than any bake-out or pump-down timescales. This allows us to approximate the scaling of the diffusion current by a square-root dependency in the time, $j_{\text{diff}} \propto t^{-1/2}$ [166].

Permeation.—The process of gas permeation through a material is subject to the pressure gradient across the material and obeys the equation:

$$j_{\text{perm}} = -K\frac{1}{2d}(p_1 - p_2), \tag{2.5}$$

where j_{perm} is the permeation current, K is a temperature and material dependent permeation constant, d describes the thickness of the material and $p_1 - p_2$ provides the pressure difference across the material. In contrast to desorption and diffusion, the permeation current is lacking an explicit time dependence. Rather, the time-dependence is contained within the evolving final pressure. However, since the permeation current increases with decreasing final pressure, we approximate this current in our own calculations by setting $p_2 = 0$.

Using our knowledge of these outgassing processes, we can calculate the pressure in our vacuum system as a function of time according to the following formula:

$$p(t) = \frac{Q_{\text{des}} + Q_{\text{diff}} + Q_{\text{perm}}}{S_{\text{eff}}}, \tag{2.6}$$

where Q_{des}, Q_{diff} and Q_{perm} are outgassing rates corresponding to desorptive, diffusive and permeative dynamics in the system (in units of $\text{mbar}\,\text{L}\,\text{s}^{-1}\,\text{cm}^{-2}$) and S_{eff} is the effective pumping speed of the pumps in our vacuum system. The latter is calculated using the relevant pipe conductances according to $1/S_{\text{eff}} = 1/S_{\text{x}} + 1/C_{\text{x}}$, while the outgassing rates are deduced from their respective currents (e.g. $Q_{\text{diff}} = j_{\text{diff}}A$, where A is the interior surface area of the vacuum chamber). The results are shown in Fig. 2.4(a). The theory is compared to pressure data collected during the final bake of our vacuum system and measured using a hot-cathode gauge (see Section 2.1.6 for details). It is important to note that by this point, the vacuum system has undergone multiple bakes at varying temperatures (see Section 2.1.6). The diffusion constant D is exponentially dependent on the temperature and as such, greatly influences the H_2 concentration gradient within the bulk. This gradient is frozen out upon returning to room temperature and therefore the high-temperaure equilibrium dynamics, including the outgassing rate, are preserved at room temperature. To illustrate this behavior and calculate the initial concentration of H_2 present in our vacuum system immediately prior to recording the data shown in Fig. 2.4(a), we solve the diffusion equation Eq. (2.3) using the well-known Crank-Nicolson finite difference method [167]. We set our initial concentration to be $n_{L0} = 40 \times 10^6$ Pa L/m^3 [166] and calculate our diffusion coefficient to be $D \approx 3.5 \times 10^{-11}$ at 400°C [168]. Under the boundary conditions mentioned previously, we are able to calculate the density profile in the bulk as the bake progresses [Fig. 2.4(c)] and extract a final H_2 concentration. The pump-down data is fitted with a $1/t^{\alpha}$ dependence [169, 170] to reflect the approximate scaling behavior of each outgassing process, as discussed previously. From this fit we find a scaling exponent of $\alpha = 0.33$, close to a value of 0.5, expected from pre-baked stainless steel [171]. The discrepancy between the recorded data and the calculated pump-down curves may stem from the presence of other materials in our vacuum system, most notably, the different glass varieties used in our glass cell.

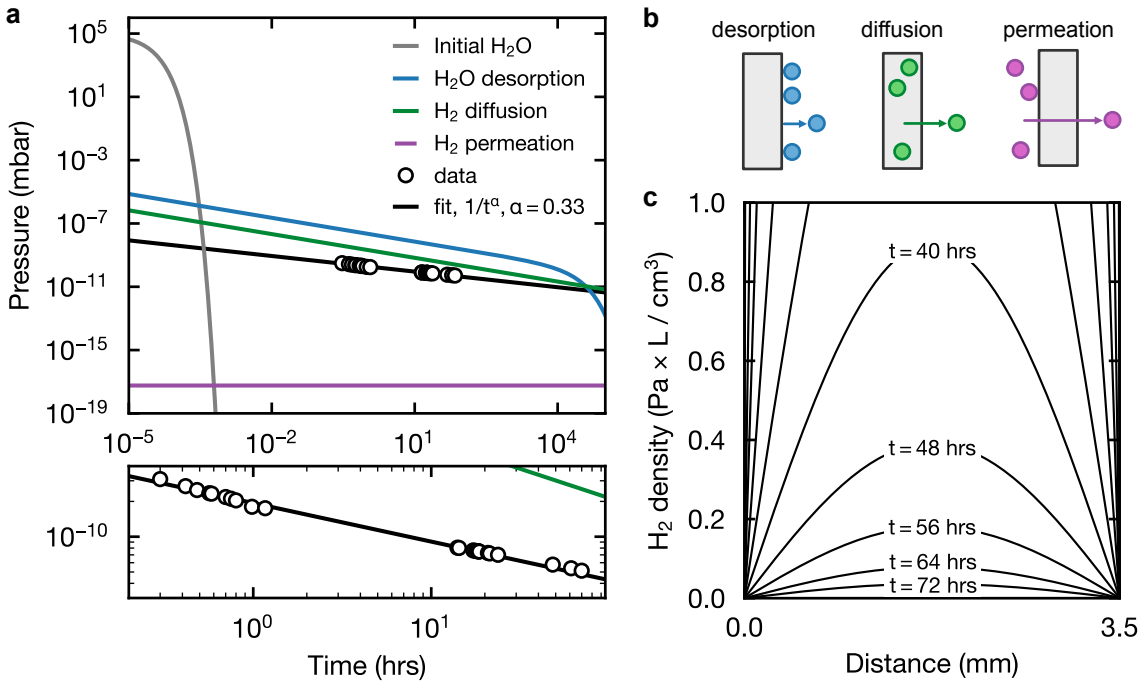

Figure 2.4 | **Pressure profiles.** (**a**) Pressure curves for various outagassing processes during the final pump-down of our vacuum system. The recorded data exhibits a $1/t^{0.33}$ scaling - close to the expected $t^{0.5}$ behavior of baked stainless steel. As expected, the pressure trends close to the diffusive process, which is expected to be limiting at UHV. (**b**) Schematics of the three outgassing processes considered in our calculations. (**c**) The density profile of hydrogen in the bulk of our stainless steel chamber walls as a function of bake time at 400°C. To obtain these profiles, we solve the diffusion equation using the Crank-Nicolson method. The diffusive dynamics are „frozen-out“ upon returning to room temperature and serve as the starting point for the pressure profile calculated in (**a**).

2.1.6 Assembly and bake

Cleaning and pre-baking.—To reduce the outgassing rates of our vacuum components, we decided to perform several pre-bakes at various stages of the vacuum system assembly. To remove any surface level contaminants, all steel components were initially cleaned in an ultrasonic bath consisting of water and a universal cleaning agent[7] in a ratio of roughly 100:5 at 60°C for 10 minutes. Upon removal from the bath, the components were rinsed with deionized water before being placed in a second ultrasonic bath of acetone for 15 minutes at room temperature. Subsequently, the components were rinsed with isopropanol and left to air-dry. We then wrapped the steel parts in UHV aluminium foil and placed them into a vacuum oven. Here the parts were baked under vacuum at the maximum oven temperature of 200°C for 72 hrs.

Next we decided to perform an in-situ bake of the steel components. To this end, we assembled the differential pumping sections of the vacuum system, including the hot-cathode gauge, but exlcuding the SAES pumps, which were replaced by blind flange placeholders. Similarly, the connecting flanges to the atom source and the glass cell were sealed off using blind flanges. To ensure a homogeneous seal around the copper gaskets, the flange screws were tightened in a star pattern using a torque of 9 Nm and 16 Nm for CF40 and CF63 flanges

[7] TICKOPUR R33

respectively. In total, twenty thermocouples were attached to the chamber walls at various points to detect the temperature during the bake. The temperature was recorded using three *TC-08* thermocouple data loggers from Pico Technologies. Heating tape was placed around the chamber ontop of an initial layer of UHV aluminium foil. This was followed by three layers of aluminium foil and fiberglass for insulation, ensuring a homogeneous heat distribution. The chamber was evacuated down to 2×10^{-7} mbar by a turbo pump (measured on the pump stand using a cold-cathode gauge[8]). Over the course of a day, we carefully ramped up the temperature of the chamber to 400°C, where it was maintained for 72 hrs. After ramping down the temperature, we briefly activated the hot-cathode gauge, measuring a steady-state pressure of 8.4×10^{-9} mbar compared to a turbo pump reading of 2.5×10^{-8} mbar. Next, we attached the SAES pumps and the angle valves and performed a bake at 240°C for 108 hrs. The ion pump magnets were removed prior to the bake.

Assembly and alignment.—Assembly of the vacuum system proceeded in two stages. First, we attached the atom source to the pre-baked steel components. Unfortunately, during this process we accidentally vented the atom source to atmosphere by failing to completely close the gate valve infront of the first differential pumping tube before removing the CF16 blind flange at the end of the tube. As luck would have it, the oxidation rate of ytterbium is rather slow when compared to alkali or alkaline-earth atoms so that we did not need to replace the oven at this point. However, an additional bake of the vacuum system was necessary (see Appendix A). Having attached the atom source onto one end of our baked steel parts, we then flanged the glass cell onto the other end to complete the assembly of our vacuum system. We used back-reflected 556 nm light to align the glass cell. Specifically, we pre-aligned a 556 nm beam to be perpendicular to the optical table before attaching the glass cell to our vacuum system. Upon attaching the cell, we overlapped the back-reflections of this guide beam from the top viewport of the glass cell with the incoming beam by rotating the cell in its flange, thus eliminiating the roll (yz) degree of freedom. The same procedure was performed at the front of the glass cell to eliminate the pitch (xz) degree of freedom. Instead of rotating the cell, we found that slightly tightening the flange screws was already sufficient to counteract any pitch of the glass cell. We used the same guide beam to compensate the tilt of the entire vacuum system by tuning the height of the chamber mounts and observing the amount of light in the 2D MOT section of the atom source. Prior to our final bake, we performed a leak check with helium[9] and detected a small leak that was fixed by replacing the copper gasket of the offending flange. We then placed a protective steel cylinder around the glass before wrapping the entire vacuum system in several layers of UHV aluminium foil, insulating fiberglass and heating tapes. The baking temperature was steadily increased at a rate of no more than 15°C/hr, as governed by the atom source. The maximum baking temperature was kept below 120°C around the atom source (limited by the gate valve) and 150°C at the glass cell to avoid excessive thermal gradients across the vacuum system. We maintained the vacuum system at these temperatures for nineteen days before ramping the heaters down.

Vacuum pump activation.—Upon completion of the final bake, we cycled the oven three times as per AOSense instructions. A single cycle involved ramping the oven temperature to

[8] Pfeiffer Vacuum IKR 270
[9] Leybold Vacuum Phoenix L300

500°C and mainting this temperature for two hours while carefully monitoring the pressure using the cold-cathode gauge on our turbo pump and the oven ion pump controller. Prior to cycling, the Zeeman slower hot window was ramped to 380°C. Due to the accidental venting of the atom source to air, we also had to re-activate the getter pumps in the atom source (SAES Z100 and STS172). These were activated sequentially by applying specified current ramps to each pump manually using a set of lab power supplies. We took the opportunity to perform absorption spectroscopy during each cycling of the oven.

Having cycled the oven, we turned to the getter pump activation in the differential pumping sections. We decided to activate the Z200 and D500 simultaneously to avoid saturating either pump with dirt from the other. Prior to the getter activation we degas our hot-cathode gauge, flash the Z200 and D500 ion pumps and perform another leak check. Activation of the getter elements was performed at 550°C while carefully monitoring the surrounding flange temperatures using thermocouples and an infrared camera. We found that the specified 1 hr activation cycle only partially activated the getters and so another activation was performed at the same temperature for 3 hrs. Subsequently, we turned on both ion pumps while the getter temperature was still ramping down (at $\approx$ 170°C) and closed the angle valves to the turbo pump. Within a few hours, the pressure logged by the hot-cathode gauge fell below $\times 10^{-11}$ mbar and eventually settled at $\approx 3 \times 10^{-11}$ mbar [see lower panel of Fig. 2.4(a)].

2.2 Magnetic fields

Controllable magnetic fields are ubiquitous in cold atom experiments. In our apparatus, they are required to generate MOTs, perform spectroscopy, spin and state-selective control, the tuning of atomic interactions and the compensation of earth's magnetic field. These varied applications require different types of magnetic fields, which in turn require different types of magnetic field coils. In this section we describe the coils and magnetic field control employed in our lab.

2.2.1 Mechanical design

Main MOT coils.—Each of our main MOT coils consists of 6×8 (radial, $\rho \times$ axial, z) windings of copper hollow core wire of dimensions 4 mm × 3 mm with a core diameter of ⌀1.6 mm (manufactured by *Krämer Energietechnik GmbH*). Together, these form coils with an inner (outer) diameter of ⌀75 mm (⌀125.4 mm), situated symmetrically about our glass cell as illustrated in Fig. 2.5(a). The coils are glued into $W \times L \times H = 150\,\text{mm} \times 180\,\text{mm} \times 20\,\text{mm}$ fiberglass plates[10] using two-component epoxy[11] and additionally held in place by heat-resistant zip-ties. Water-cooled hollow core wire enables the coils to run at currents in excess of 100 A for short durations without a significant increase in temperature. This allows us to generate magnetic fields of up to 400 G at the location of the atoms.

Shim and compensation coils.—To generate magnetic offset fields, we use a set of „shim" coils. These are small coil pairs wound from AWG18 copper wire and arranged along each spa-

[10] Erhard Hippe KG EP-GC-201
[11] DELO DUOPOX AD840

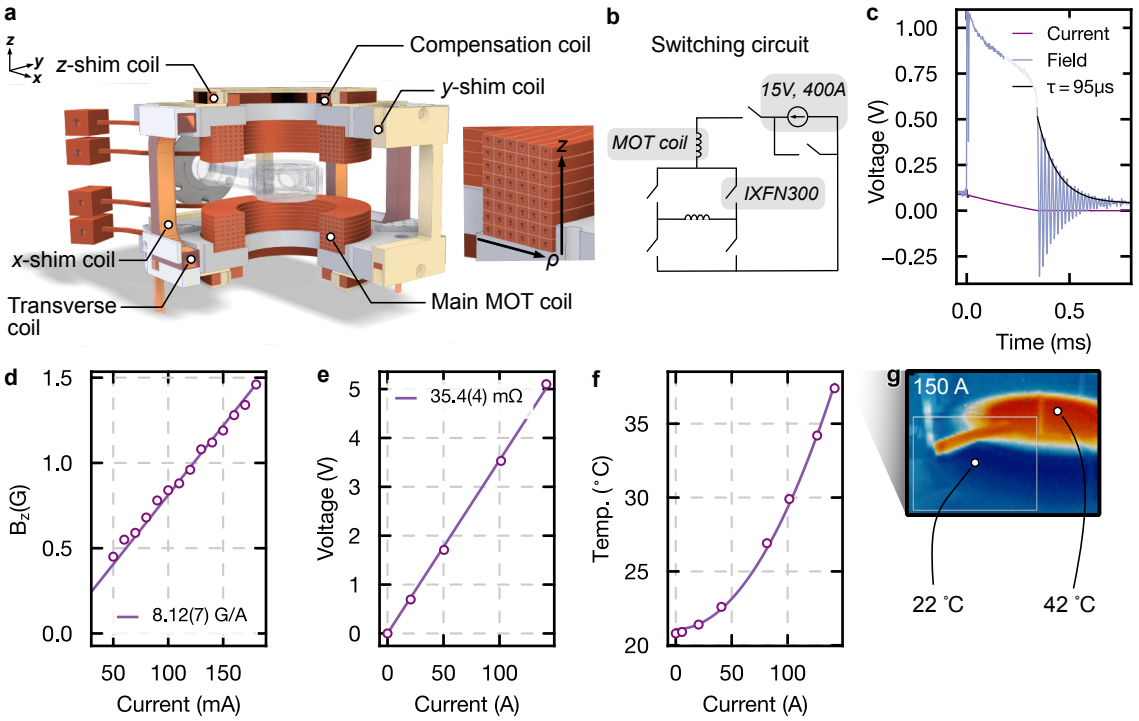

Figure 2.5 | **Magnetic field coils.** (**a**) Render of the magnetic field coils used in our experiment. Two main MOT coils consisting of water-cooled hollow-core wire provide strong fields for trapping and spectroscopy. These coils are supplemented by a smaller shim coil pairs in each spatial dimension which allow us to add an offset to the magnetic field. Along the *z*-axis, we add an additional compensation coil pair for compensating the earth's magnetic field. Finally, a set of water-cooled transverse coils along the *y*-axis allow us to define a quantization axis at an arbitrary angle in the (*yz*)-plane. (**b**) Fast anti-Helmholtz/Helmholtz and on/off switching is enabled by a MOSFET H-bridge switching circuit. (**c**) The switch-off duration of our coils is determined to be 95 μs using a ringdown measurement (see main text for details). (**d**) Our main MOT coils are able to generate magnetic fields of 8.12(7) G/ A at the location of the atoms. (**e**) The resistance of each of our main coils is measured to be ≈ 35mΩ. (**f**) Temperature of our main coils (with water cooling) at various currents, each applied for a number of minutes. The expected temperature at higher currents can be determined from a quadratic fit of the data (solid line). (**g**) Thermal camera picture of our coils at a current of 150 A showing the heat distribution in one of the water-cooled main coils.

tial dimension. The shim coils are designed to deliver smaller fields of 1−2 G while drawing only a couple of amperes of current, thus obviating the need for active cooling. Current is provided to these coils by smaller programmable power supplies[12]. Along gravity we have an additional pair of coils of similar dimensions to the shim coils for compensating the earth's magnetic field.

Transverse coils.—Finally, a rectangular pair of water-cooled coils capable of generating up to ≈ 25 G at 100 A is oriented along the *y*-axis (transverse to the atomic beam propagation direction). Switching between a Helmholtz and an anti-Helmholtz configuration is facilitated by a network of MOSFETs (see Section 2.2.3). In combination with the other coil pairs, this allows us to add an additional external magnetic field along any arbitrary direction.

[12]Delta Elektronika - ES150

2.2.2 Magnetic properties

We estimate the magnetic field strength of our coils along the radial and axial directions by approximating each winding of hollow core wire as a simple 1D current loop and calculating its contribution to the total magnetic field via the Biot-Savart law:

$$B_\rho = \frac{\mu_0 I}{2\pi} \frac{1}{\sqrt{(R+\rho)^2+z^2}} \frac{z}{\rho} \left(\frac{R^2+\rho^2+z^2}{(R-\rho)^2+z^2} E(k^2) - K(k^2) \right) \tag{2.7}$$

$$B_z = \frac{\mu_0 I}{2\pi} \frac{1}{\sqrt{(R+\rho)^2+z^2}} \left(\frac{R^2-\rho^2-z^2}{(R-\rho)^2+z^2} E(k^2) + K(k^2) \right) \tag{2.8}$$

$$k = \frac{4R\rho}{(R+\rho)^2+z^2}, \tag{2.9}$$

where $E(k^2)$ and $K(k^2)$ are elliptic integrals of the first and second kind respectively [172]. R is the radius of the coils, I the current flowing through the conductor and $\mu_0 = 4\pi \times 10^{-7}$ H/m is the magnetic permeability of the vacuum. The resulting fields are plotted in Fig. 2.6(a) in Helmholtz (top two panels) and anti-Helmholtz configuration (bottom two panels). we calculate a magnetic field strength of 7.38 G/ A and a gradient of 1.95 G/ cm/ A at the center of the coils. We also calculate the homogeneity of the magnetic field at the location of the atoms. In particular, we are interested in how the magnetic field varies within a region of similar size to our 3D MOT and also across the 100 µm field of view (FOV) of our objective (see Section 2.5.2). This is especially relevant for the states of the clock transition, as these form the basis for many of the quantum simulation encodings we plan to investigate using our apparatus. We define the inhomogeneity as the change of our magnetic field with respect to the field at B_0 [173]:

$$\text{inhomogeneity} = \frac{B(I,x,y,z)}{B(I,0,0,0)} - 1. \tag{2.10}$$

The result is shown in Fig. 2.6(b). In the top panel we plot the inhomogeneity across a 50 mm × 50 mm region in the xz-plane. The location of the MOT coils are indicated by red rectangles. In the bottom panel, we zoom in on the central 10 mm × 10 mm region of the top panel, roughly congruent with the diameter of our 3D MOT beams. Within this region, the inhomogeneity is calculated to be, at worst, ≈ 2%. Together with a quadratic Zeeman shift of 61.2(1) mHz/ G^2 [174], this results in a clock shift of ≈ 400 Hz at 400 G. This compares favorably with the clock linewidth at these field strengths and indicates a negligible effect for physics conducted within the much smaller FOV of our high-resolution objective. This also justifies the non-optimal Helmholtz configuration of the two main coils ($d = 49.5$ mm ≠ $R = 50.1$ mm) which was chosen as a compromise between Helmholtz field strength, anti-Helmholtz linearity and geometric constraints.

We perform several measurements to confirm that our main MOT coils operate as expected and conform to the requested specifications. We measure the magnetic field along the z-axis using a Hall probe positioned at the center of the coil pair. After determining the zero-current magnetic field to calibrate the measurement, we gradually increase the current applied to the coil pair and measure the resulting magnetic field. From a linear fit of the data, we obtain a Helmholtz field of 8.12(7) G/ A [Fig. 2.5(d)], with an error given by the standard deviation of

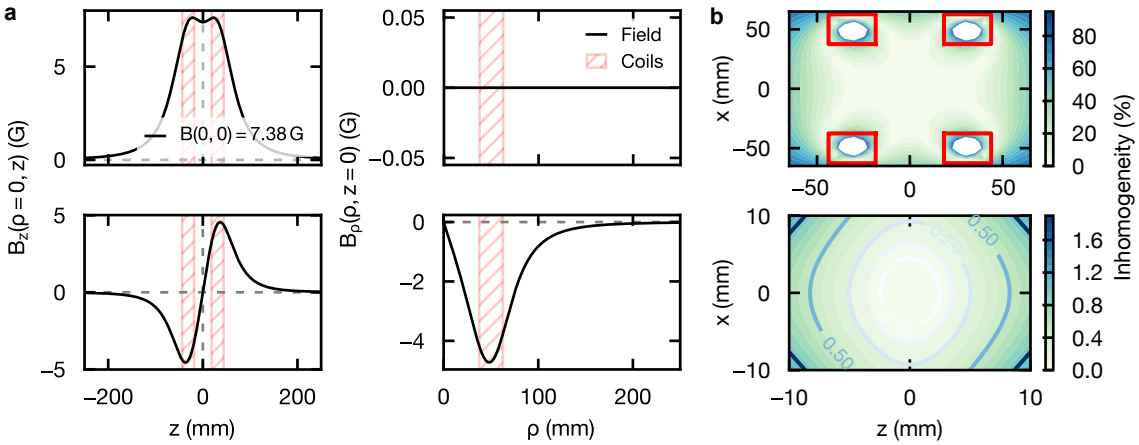

Figure 2.6 | Magnetic properties of main MOT coils. (**a**) The calculated magnetic field of our main MOT coils at 1 A of current, plotted along the radial (ρ) and axial (z) directions in Helmholtz (top two panels) and anti-Helmholtz (bottom two panels) confiuguration. The field was calculated by approximating each winding of our coils as a simple current-carrying loop and computing the relevant contribution to the total field via the Biot-Savart law. From this calculation, we predict a field of 7.38 G/ A in Helmholtz configuration at the location of the atoms. This value is confirmed by a quadratic Zeeman shift measurement (Section 3.4). (**b**) Magnetic field inhomogeneity in the xz-plane. The bottom panel is an enlarged version of the central 10 mm × 10 mm region of the top panel. The red rectangles in the top panel indicate the location of the main MOT coils. We find that the inhomogeneity over the FOV of our high resolution objective is negligibly small (see main text for details).

the data. This is close to the actual 7.41(8) G/ A measured using the atoms' quadratic Zeeman shift (see Section 3.4 for details) as well as the theoretically predicted 7.38 G/ A. Possible reasons for the discrepancies in values include probe miscalibration and deviations from the design geometry during the manufacturing process.

2.2.3 Electrical properties

The main MOT coils are powered by a 400 A, 15 V programmable power supply[13]. We use a set of MOSFETs[14] in an H-bridge architecture to switch between Helmholtz and anti-Helmholtz configurations Fig. 2.5(b). The switching is remote controlled from our sequence via a custom interlock-connected logic board. We calculate the resistance of our coils to be $R = \rho_{\mathrm{Cu}} \frac{l}{A} = 21.5\mathrm{m}\Omega$, where $l = 12.8\,\mathrm{m}$ and $A \approx 10\,\mathrm{mm}^2$ are the length and cross-sectional area of our copper hollow-core wire, and $\rho_{\mathrm{Cu}} = 1.68 \times 10^{-8}\Omega\mathrm{m}$ is the resistivity of copper at 20°C. For the calculation of the self-inductance of the coils we make use of the following empirical formula [175]:

$$L \approx 39.37 \times \frac{0.8N^2r^2}{6r + 9h + 10w} = 176\,\mu\mathrm{H}, \tag{2.11}$$

where $N = 48$ is the number of windings and $r = 50.1\,\mathrm{mm}$, $h = 25.4\,\mathrm{mm}$ and $w = 50\,\mathrm{mm}$ are the mean radius, height and width of the coil respectively. Our calculations are confirmed

[13] Delta Elektronika SM15-400
[14] IXYS IXFN300

by an inductance measurement using a bridge circuit[15] where we measure self-inductances of 219(5) μH and 220(5) μH for theses coils.

We use the same universal bridge to perform a Q-factor measurement, which indicates how close our coils are to an ideal inductor. In our coil circuit, the Q-factor is given by the ratio of an inductors reactance (i.e. its opposition to an alternating current) to its resistance [176]:

$$Q = \frac{\omega L}{R}, \tag{2.12}$$

where L is the inductance, R the resistance and ω the frequency of alternating current driven through the coils. From this we obtain coil resistances of 32.4(6)mΩ and 36.7(7)mΩ. These values are in close agreement with the 35.4(4)mΩ obtained by simply reading out the power supply current for a given set voltage [Fig. 2.5(e)]. Finally, we want to know how fast the coils are able to switch between different current configurations and states. To determine the switch-off time, we perform a ringdown measurement by suddenly quenching the applied current from 100 A to 0 A and observing the magnetic field response using our Hall probe. The behavior of the coil after the quench is described by:

$$V(t) = V_0 e^{-\frac{\omega}{2Q}t} \cos\left(\omega t \sqrt{1 - \frac{1}{4Q^2}} + \phi\right), \tag{2.13}$$

where V_0 is the initial voltage, ϕ is the phase of the voltage. The exponential envelope of this fit yields a ringdown time of $\tau = 95\,\mu s$, leading to a total switch-off duration of 440 μs from 100 A including the power supply's fall time. In the experiment, this switch-off time is significantly increased by the presence of eddy currents to around 8 ms. One strategy to mitigate this effect would be to switch the polarity of one coil for a brief burst of time, as demonstrated in Ref. [177].

2.2.4 Thermal management

Water-cooling is provided by a 3.2 kW chiller specified to a maximum throughput of 7.2 L/min at 17.2 bar[16]. We continuously monitor the flow rate, temperature and conductivity of water entering and exiting each coil using a combination flowmeter[17]. Under normal operating conditions, around 350mL/min of water running through each coil are enough to maintain a surface temperature of 20°C. The flowmeter pulse output is used as a monitor signal for the coil interlock. The remaining sensor data is read out using a custom PCB designed to handle MODBUS communication with the flowmeter. This same flowmeter scheme is repeated everywhere in our lab where water cooling is required. The temperature of each coil is measured using one or more E-type thermocouples, held in place by thermally conductive two-component glue[18] and read out by a data logger[19]. To ensure that the coil temperatures do not exceed

[15] HP4620A
[16] Van der Heijden Labortechnik GmbH
[17] Digmesa FHKU CombiSensor
[18] Fischer Elektronik - WLK10
[19] Keysight 34980A multichannel switch

acceptable limits, an alarm setpoint is programmed in software which enables the remote shutdown of the offending coil power supply.

We measure the temperature of our coils at various current values to test the thermal repsonse of the coils [Fig. 2.5(f)]. During this measurement the coils were supplied with $\approx$ 250mL/min of 20°C water. At each current setpoint we waited several minutes before recording the final temperature. This is a quasi-DC regime, as one run of our experimental sequence is on the order of 100's of ms. While the coil surface heats to nearly 30°C at 100 A during this test measurement, we find that in the experiment, repeatedly ramping to high currents on the ms scale has no discernible effect on the surface temperature of the coils.

2.3 Laser systems

In our experiment a multitude of different lasers and optical setups are required for the trapping and cooling of atoms. In this section we describe the design of each of these optical setups and explain their purpose and functionality.

2.3.1 Blue laser

Our blue laser is a frequency-doubled Toptica DL-TA-SHG-Pro. This commerical laser consists of an external-cavity diode laser (ECDL) optimized for a fundamental wavelength of 798 nm acting as a seed for a tapered amplifier (TA). The amplified fundamental light is frequency-doubled by means of second-harmonic-generation (SHG) in a non-linear crystal enclosed in a hermetically sealed optical cavity. The resulting emission at 399 nm is processed in the adjoining optical setup and sent to the experiment. The emission at the fundamental wavelength is used to frequency stabilize the laser to an ultra-stable reference cavity (Section 2.4). Blue light is required in our experiment for the Zeeman slower, the 2D MOT, absorption imaging of the atoms and pre-slowing the atoms prior to trapping in our 3D MOT. The most commonly used element for frequency shifting light is an acousto-optic modulator (AOM). These rely on the variation of the refractive index of a crystal to diffract light into different orders, each with a unique frequency. By varying the radio-frequency (RF) applied to the AOM, it is possible to tune the frequency of the diffraction orders continuously within some specified frequency range (usually $\approx 10 - 20$ MHz around the central frequency). While this allows for fast and flexible control of the optical frequency, both the bandwidth and central frequency of the AOM are limited to the MHz range. This means we must be careful to design an optical setup which is able to meet all the required optical frequencies for the different applications while remaining within a frequency budget easily accessed by standard AOM RF frequencies. For our blue laser, we find that operating the laser at a detuning of $\omega_{\text{laser}} - \omega_0 = -390$ MHz from the $^1S_0 \rightarrow {}^1P_1$ transition ensures that the furthest detuning required from a single AOM is -200 MHz for our Zeeman slower (see inset to Fig. 2.7). For the remaining beam paths, we first use an AOM in double-pass configuration[20] to impart a frequency shift of +210 MHz on the light. The imaging beam is brought to resonance by sending this light through two single-pass AOMs of the same

[20] Gooch&Housego I-M110

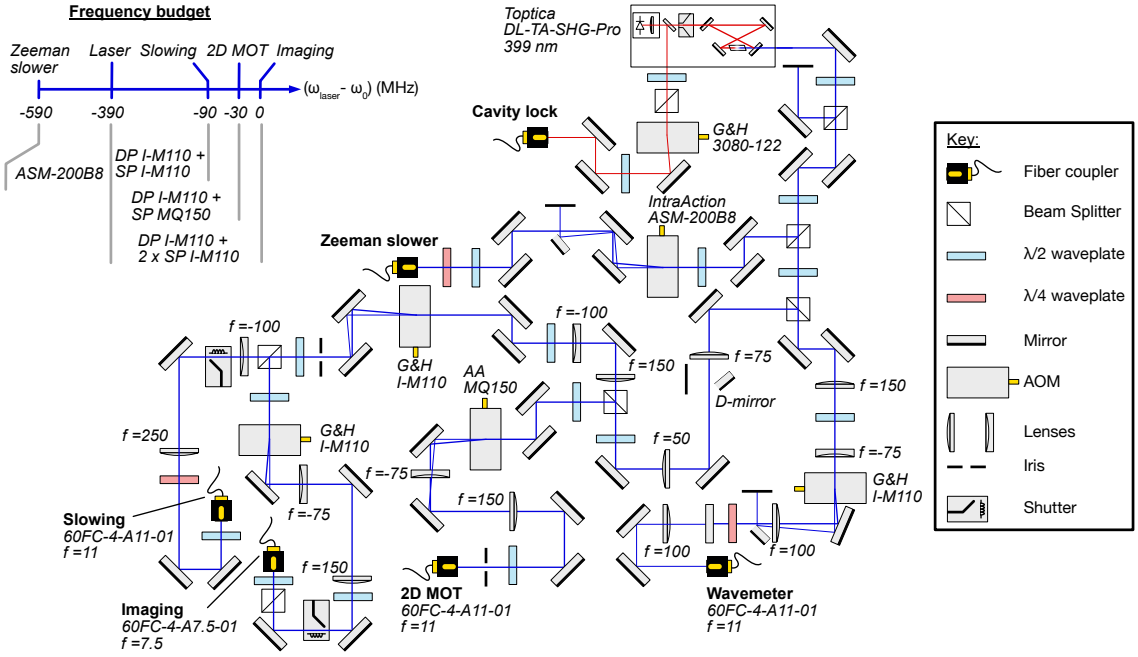

Figure 2.7 | Blue laser optical setup. Our blue laser system outputs ≈ 1.1 W of light at 399 nm from a frequency-doubled and amplified 798 nm seed laser. This light is split into several branches, each of which is used for a different application in our experiment. The frequency of each branch is controlled by at least one AOM, which we also use to intensity stabilize the light in that branch. A mechanical shutter is included in each branch to prevent leakage light in the experiment when shuttering off the AOMs. A number of different telescopes, lenses and polarization-sensitive optics are used to optimize the AOM diffraction and fiber-coupling efficiencies. Some of the 798 nm fundamental light is used to frequency stabilize our laser system to an ultrastable reference cavity by coupling into a fiber EOM. All focal lenghts are in units of mm unless specified otherwise. *Inset*: The frequency budget for our blue laser system, showing how we reach all relevant optical frequencies in our experiment.

kind, operating at +90 MHz. The crossed slowing beam shares half of the imaging path, passing through a single +90 MHz AOM before being fiber-coupled. Finally, for the 2D MOT, a single AOM at +150 MHz[21] is sufficient to generate the necessary detuning of −30 MHz.

In addition to a frequency budget, we are also constrained by the total ouput power of the laser. For our blue laser this is measured to be ≈ 1.1 W and expected to degrade over time. At lower wavelengths the power degradation is especially pronounced due to the reaction of dielectric coatings with high energy light. Careful beam shaping using lenses and telescopes is required to maximize the coupling efficiencies into our AOMs and optical fibers. The largest fraction of the laser's output power is consumed in the Zeeman slower path, which requires ≈ 300 mW incident on the atoms. We achieve a diffraction efficiency of 84% through the 200 MHz AOM[22]. The zeroth order is deflected into a beam dump using a D-shaped mirror and the first order coupled into an optical fiber with custom end-caps[23]. A fiber end-cap is a small amount of material spliced onto the end of a fiber to protect the fiber from high optical

[21] AA MQ150
[22] ASM-200B8, IntraAction Corp.
[23] Coastal Connections

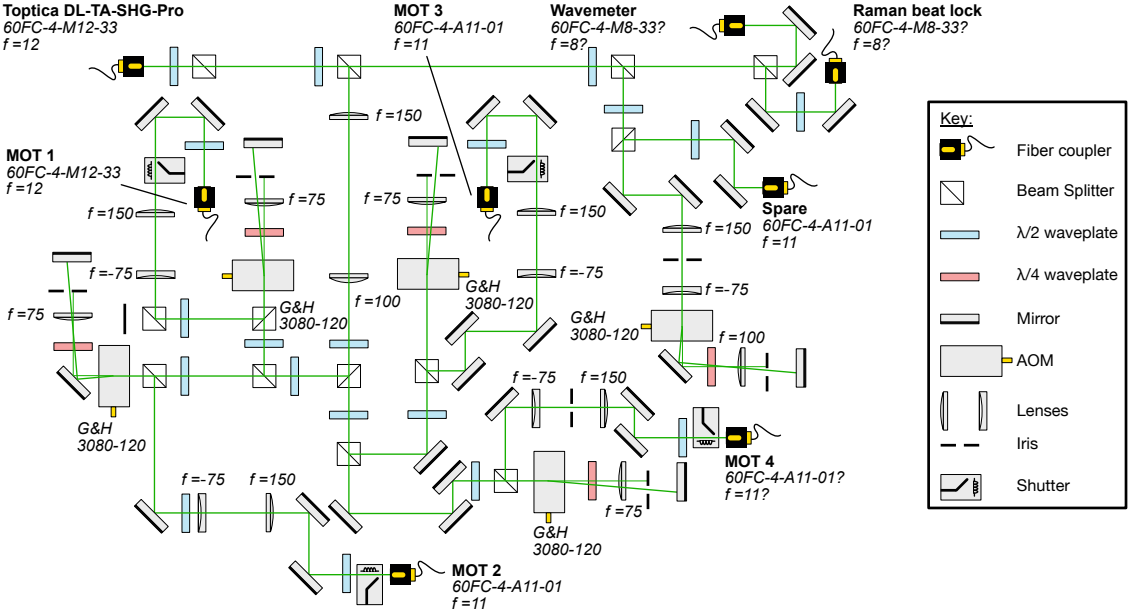

Figure 2.8 | Green laser optical setup. The main output of our green laser is fiber-coupled and routed to a dedicated breadboard where ≈ 1 W of 556 nm light is used in four MOT arms and for a Raman beat-lock. The frequency of each of our MOT beams is controlled using double-pass AOMs which preserve the fiber-coupling efficiency in each branch at the cost of available optical power. As in the blue setup, each of these AOMs is also used for intensity stabilization and control.

powers and reduce the ageing of the fiber at wavelengths close to the ultraviolet (UV) range. Apart from the wavemeter fiber, all of the fibers used in our blue laser setup are of this type. We also make use of the AOMs to intensity stabilize each beam in the setup. This is done by measuring the out-coupled power in each beam close to the experiment using a photodetector and feeding back to a custom intensity servo. This servo modulates the amplitude of the RF signal sent to each AOM in order to maintain a pre-determined setpoint which we can program from our experimental sequence. The set frequency for the majority of our AOMs is controlled by an RF synthesizer[24], the output of which is amplified in a custom AOM driver. By sending trigger signals from our control software to our AOM drivers, we enable or disable the RF drive as required. Even with the RF drive disabled, some amount of unwanted light is still able to leak through an AOM and make its way to the experiment. To prevent this, we also equip each beam with a homebuilt mechanical shutter based on the solenoid driven needle actuator from a sowing machine. Due to its comparatively long shuttering time, we are careful to open and close the shutter to match the shuttering of the corresponding AOM. Furthermore, we have found that some AOMs require an additional thermalization period after enabling the RF input. To circumvent this, the default state of our AOMs is to have the RF drive enabled.

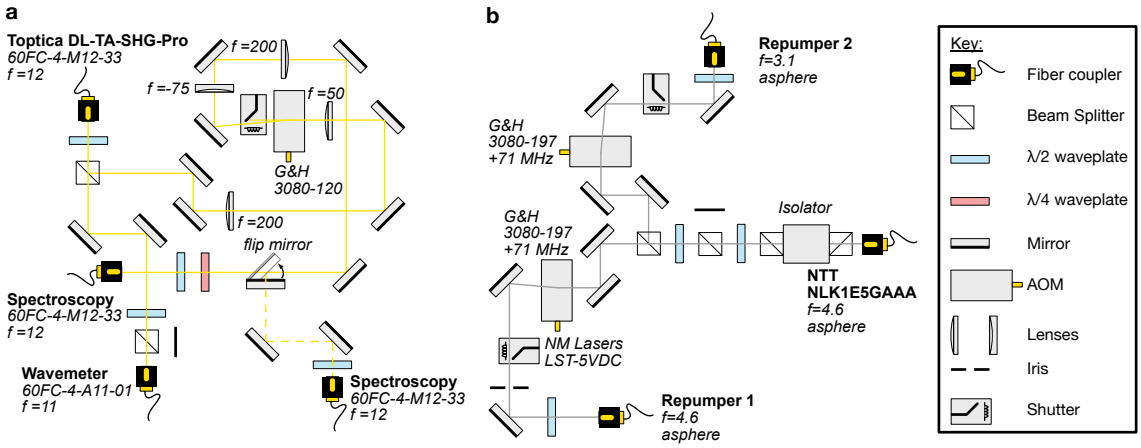

Figure 2.9 | Clock laser and repumping setup. (**a**) 578 nm light from a Toptica laser is fiber-coupled onto a separate breadboard, where it is split into two spectroscopy beams and a wavemeter monitoring arm. Which of the two spectroscopy beams is in use at a particular moment is governed by a flip mirror. (**b**) A DFB fiber-coupled laser module is used to produce 1389 nm light which is split into two separate branches for repumping atoms. Each branch sends ≈ 10 mW of light to the atoms and is detuned from the transition frequency by +71 MHz.

2.3.2 Green laser

We use another Toptica DL-TA-SHG-Pro to produce 556 nm light for our 3D MOT and for beat-locking a 556 nm Toptica DL-TA-Pro laser, which we plan to use for Raman cooling (see Section 2.5.4). As is the case for the blue laser, we use some of the infared light at 1112 nm to lock this laser to our ultrastable reference cavity. A schematic of the laser setup is shown in Fig. 2.8. Unlike our blue laser, the main output of our green laser is directly fiber-coupled using a Toptica FiberMon. This results in ≈ 1 W of usable light on our setup. Due to our high-resolution microscope objective, retro-reflection of the MOT in the vertical direction (z-axis) is not feasible. As such, our 3D MOT requires four independent beams: two retro-reflected beams in the horizontal (xy) plane and two counterpropagating beams through the top and the bottom of our glass cell. The frequency of each of these MOT beams is controlled by an AOM in double-pass configuration[25]. Ideally, this configuration ensures that the fiber-coupling efficiency remains independent of the AOM frequency at the cost of overall usable power in each beam. As in the blue setup, we also use each of these AOMs for intensity stabilization and use mechanical shutters to ensure no leakage light through the AOMs reaches the experiment.

2.3.3 Clock laser

The laser used for coherently addressing the ultra-narrow $^1S_0 \rightarrow {}^3P_0$ clock transition is of vital importance to our experiment and its spectral properties are subject to the most stringent requirements. In particular, a narrow linewidth is necessary to allow us to perform high-resolution optical clock spectrosopy. This will be especially important for the measurements of state-dependent wavelengths detailed in Chapter 4 of this thesis. Again, the basis for our

[24] Moglabs QRF
[25] Gooch&Housego 3080-120

clock laser setup is a Toptica DL-TA-SHG Pro, this time equipped with the narrow-linewidth option 1156 nm seed laser. We use light from this seed laser to lock the system to our ultrastable reference cavity (see Section 2.4 for details). As is the case for our green laser system, the main output of our clock laser is fiber-coupled with an total usable output power of ≈ 650 mW after the fiber. Currently, our experiment utilizes two clock spectroscopy beams. The choice of which beam to use is governed by a mechanical flip mirror [Fig. 2.9(a)]. Both paths share an AOM[26] which we use to control the frequency of the light. For increased mechanical isolation, the laser along with all the optics described in this section are placed on a 600 mm × 900 mm × 59 mm breadboard supported by rubber damping feet.[27]

2.3.4 Repumping laser

We make use of the $^3P_0 \rightarrow {}^3D_1$ transition to repump atoms from the metastable excited state back into the $^1S_0$ ground state. This has a number of advantages, not least of which is the ability to separately image the ground and excited state populations (see Section 3.1.4 for details). Atom number losses from the decay channel to the dark $^3P_2$ state are limited to $\sim 1\%$. To address the repumper transition, we use a distributed-feedback (DFB) laser module[28]. Current control is afforded by a commercially available current control module[29] while temperature control is provided by a custom homebuilt temperature controller. The laser output is fiber-coupled with a total of ≈ 27 mW at our disposal, of which we use $\approx 500\,\mu$W most of the time. This is split into two branches, both of which are detuned by +71 MHz from the transition frequency. Since our wavemeter is limited to 1180 nm, we initially use an optical spectrum analyzer to set the correct output wavelength and then keep track of the optimal value using the repumped atom fraction in our experiment. The wavelength is adjusted as needed by tuneing the laser temperature.

2.3.5 Lattice lasers

We use a set of three titanium:sapphire (ti:sapph) lasers[30] to generate our 3D magic optical lattice, with each individual axis of the lattice corresponding to one of the ti:sapphs. We opt for ti:sapph lasers due to their ability to generate large amounts of power ($7 - 9$ W) around the desired wavelength of 759 nm. The optical setup for one lattice axis is shown in Fig. 2.10(a). An optical isolator[31] with ≈ 40 dB of attentuation is used to prevent unwanted back-reflections into the ti:sapph. We use an *IntraAction AOM-402AF3* for frequency control, fast switching and intensity stabilization. To cope with the high powers, the light is coupled into a photonic-crystal fiber[32]. These types of fibers make use of a photonic bandgap to confine light to the core with a high degree of isolation, thereby reducing stimulated Brillouin scattering in the fiber. An important consideration is the effect of intensity fluctuations on the lifetime of atoms trapped in our optical lattice. At a given trap frequency ν_{tr}, the heating rate of atoms is expected to be

[26] Gooch&Housego 3080-120
[27] Newport M-SG-23-2
[28] acalbfi/NTT NLK1E5GAAA
[29] Toptica DTC110
[30] Sirah Matisse CS with 25W Millennia pump
[31] Toptica SSR780
[32] NKT-LMA-PM-15

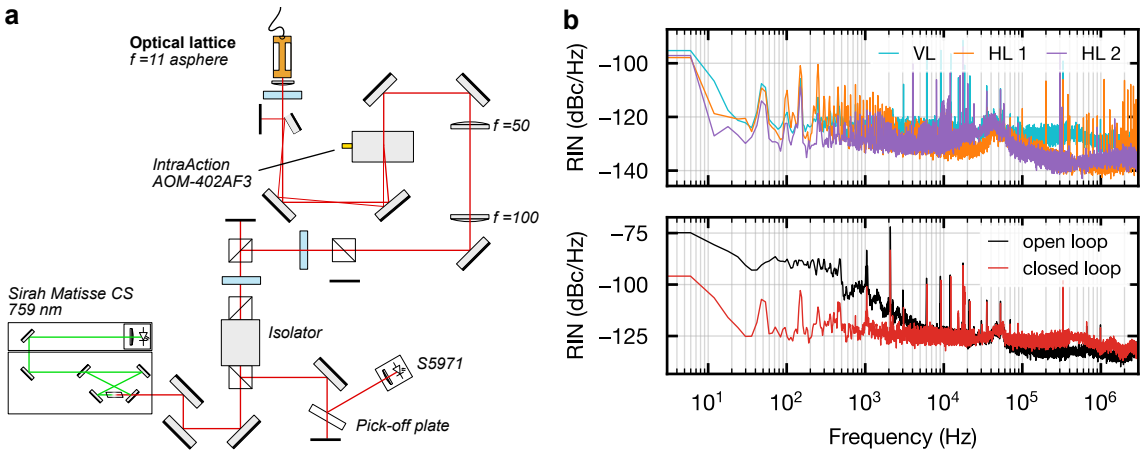

Figure 2.10 | Lattice laser optical setup. (**a**) The output of a Matisse CS ti:sapph laser is used to generate each of the axes of our 3D magic lattice. Light is coupled into a PCF fiber for power-handling and the alignment of the lattice is monitored by observing the back-reflection through the optical setup at the rejection port of the isolator using a homebuilt photodetector. (**b**) (Top panel) measured RIN curves of our ti:sapph lasers featuring a prominent peak at ≈ 40 kHz. (Lower panel) RIN curve of our vertical lattice ti:sapph with and without intensity stabilization. We observe a servo bandwidth of ≈ 6 kHz.

proportional to the one-sided power spectral density of the fractional intensity noise at twice that frequency i.e. $\Gamma_\epsilon = \pi^2 \nu_{\mathrm{tr}}^2 S_\epsilon(2\nu_{\mathrm{tr}})$ [178]. For this reason, we measure the relative intensity noise (RIN) of each of our three ti:sapphs [top panel of Fig. 2.10(b)] using a *Thorlabs PNA1* intensity noise analyzer. Notably, we observe a −120 dBc/Hz peak between 40 − 50 kHz in all three lattice arms, which limits our trap lifetime at 20 kHz to around 250 s. This is is on the same scale as our vacuum lifetime and is therefore not expected to be a limiting factor in our experiment. In addition, we determine the efficacy of our intensity stabilization by comparing the open and closed loop RIN of our ti:sapphs (an example dataset for this comparison is shown in the lower panel of Fig. 2.10(b) for our vertical lattice ti:sapph). We observe RIN supression up to a frequency of ≈ 6 kHz.

2.3.6 Tune-out lasers

To address the tuneout wavelengths for the ground and excited states of the clock transition, we employ a set of vertical-external-cavity surface emitting lasers (VECSELs)[33]. These lasers feature an optically pumped semiconductor gain chip, the output of which is frequency doubled in an external cavity using a non-linear lithium triborate (LBO) crystal. Frequency selectivity is achieved by combining a birefringent filter (BRF), thin etalon and piezo controlled cavity mirror in the cavity. Unlike laser diodes, where the beam shape of the emitted light is elliptical due to diffraction at the diode facets, emission from the gain chip occurs directly at the surface of the semicondutor, resulting in an extremely circular mode shape.

To tune the laser frequency, we first adjust the LBO temperature to a value where the emission operates in the vicinity of the desired wavelength (within ∼ 0.5 nm - specified in look-up table in the manual). We then tune the angle of the BRF for coarse wavelength selection.

[33] Vexlum VALO-SHG-SF

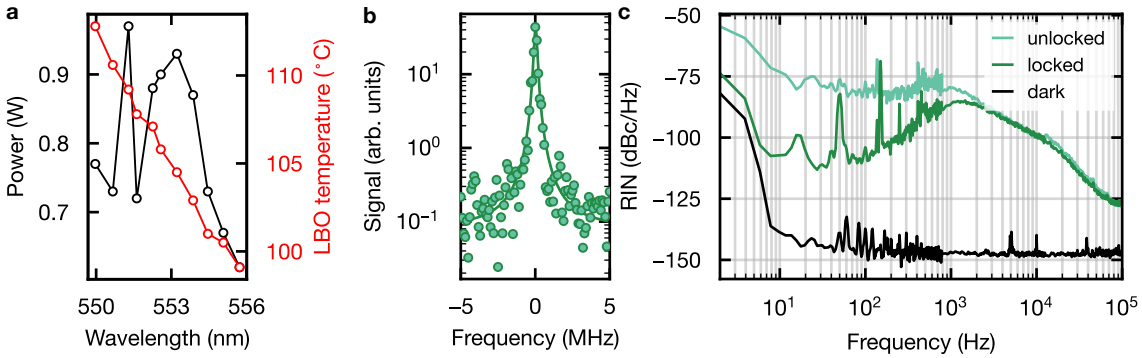

Figure 2.11 | Ground state tuneout laser characteristics. (**a**) Tuning curve of the Vexlum output power as a function of the frequency. The latter is tuned using the BRF angle and LBO temperature according to the procedure described in the main text. (**b**) A Lorentzian fit of the beat signal between the Vexlum laser and our green Toptica laser system yields an upper bound of 105(2) kHz on the Vexlum linewidth. (**c**) A comparison of the Vexlum RIN in the frequency locked and unlocked mode. Suppression of intensity noise by the lock is visible up to a frequency of $\approx$ 2 kHz.

We observe the various BRF modes on our wavemeter and select the one closest to the desired operating frequency. Once there, the output power is optimized by small changes in the LBO temperature (on the single degree Celsius level). For finer wavelength selection, we tune the temperature of the etalon itself and iterate with the LBO temperature to optimize the power. As a final step, we scan the cavity length using the piezo. To maintain a constant output frequency, we digitally lock our Vexlum lasers to the wavemeter. The digital feedback signal is processed by a digital-to-analog converter (DAC)[34] before it is amplified by a commercial piezo controller[35] and sent to the laser.

We extract an upper bound for the linewidth of the 552 nm Vexlum laser by performing a heterodyne beat measurement with our green Toptica laser system. The Toptica laser is locked to our reference cavity during this measurement and presumed to exhibit a linewidth < 5 kHz. We record the timetrace of the beat note signal using an amplified photodetector attached to a fast mixed signal oscilloscope[36]. We then calculate a fast-fourier transform (FFT) of the data and fit a lorentzian with a full width at half maximum (FWHM) of 105(2) kHz [Fig. 2.11(b)]. The intensity noise of the laser in the frequency locked and free running regime are evaluated by performing a RIN measurement using an FFT spectrum analyzer[37] [Fig. 2.11(c)]

2.4 Frequency stabilization

To perform laser spectroscopy and coherently address atoms, many of the lasers in our lab must be highly stable in their output frequency. For this purpose, we use a sideband-locking variation of the well-known Pound-Drever-Hall (PDH) frequency stabilization technique [179–181] to lock our three Toptica DL-TA-SHG Pro lasers to an ultrastable reference cavity.

[34] National Instruments USB6002
[35] Scientific Instruments PS200
[36] Tektronix MSO54
[37] SRS SR760

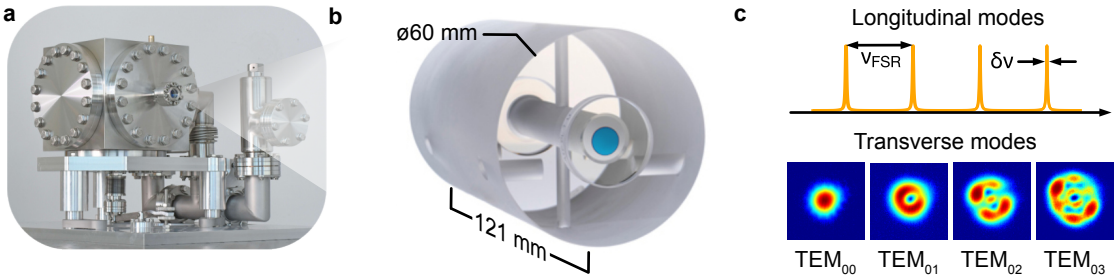

Figure 2.12 | **Reference cavity.** (**a**) An image of the complete Menlo ORS-cylindric cavity system (image credit of Menlo Systems GmbH) to which we lock the blue, green and clock lasers. The entire system is held at UHV by an ion pump and the cavity is temperature stabilized in vacuum. (**b**) A view of the cylindrical cavity manufactured from an ultra-low expansion (ULE) spacer with IBS coated mirrors on either side. The cavity is composed of one curved and one flat mirror on opposing ends of the cavity spacer. (**c**) Our cavity supports longitudinal modes separated by a free spectral range of $\nu_{\mathrm{FSR}} = 1.24\,\mathrm{GHz}$. By carefully tuning focusing lenses infront of the cavity we observe different transverse modes. We mode-match our laser light to the TEM_{00} mode of the cavity.

2.4.1 Reference cavity

Our reference cavity consits of a plane mirror and a concave mirror (radius of curvature: 1 m) attached to either side of a single-bore, cylindrical, ultra-low-expansion glass cylinder[38] of length $L = 121\,\mathrm{mm}$ and diameter ø60 mm [Fig. 2.12(a)], yielding a free spectral range of $\nu_{\mathrm{FSR}} = 1.24\,\mathrm{GHz}$. The mirrors are ion beam sputter (IBS) coated for 798 nm, 1112 nm and 1156 nm. To reduce the impact of external temperature and pressure fluctuations on the resonator stability, the cavity is contained within a vacuum chamber and actively temperature stabilized to within ±1 mK using a commerical temperature controller[39]. The entire system was purchased from *Menlo Systems GmbH*.

2.4.2 Finesse

The ability of an optical resonator to act as a frequency discriminator relies on its capacity to support only certain, very well-defined resonance frequencies (longitudinal modes of the cavity). The spectral width of these resonance frequencies $\delta\nu$ is determined by the length of the cavity L and the reflectivity R of the mirrors in the following way [182]:

$$\delta\nu = \frac{c}{2nL}\frac{1-R}{\pi\sqrt{R}} = \frac{\nu_{\mathrm{FSR}}}{\mathcal{F}}, \tag{2.14}$$

where n is the refractive index of the medium separating the cavity mirrors, and $\mathcal{F}$ is known as the finesse. The latter quantity is a relative measure for the quality of our resonator and determines the frequency resolution of the cavity. We measure the finesse of our cavity in two separate ways for each of the three frequencies that we wish to stabilize. First, we perform a ringdown measurement of the cavity photon storage time [Fig. 2.13(a)] [183]. This initially requires the relevant laser to be locked to the cavity (a detailed explanation of our locking

[38] Corning Inc. ULE 7973
[39] SRS PTC10

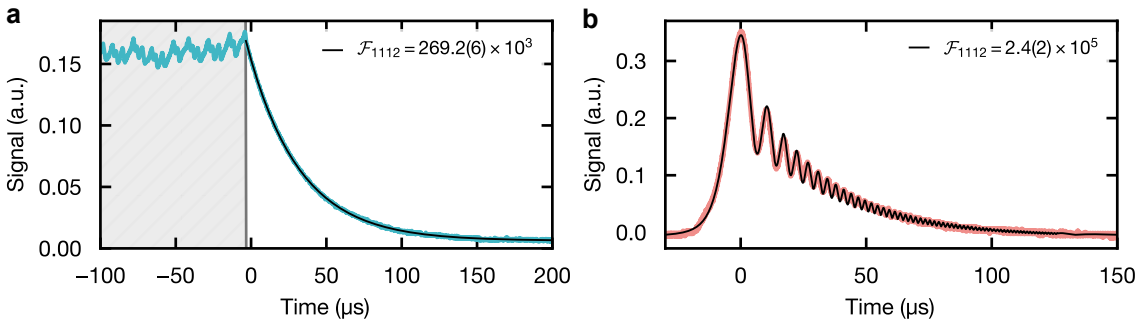

Figure 2.13 | **Cavity finesse.** (**a**) The finesse of our cavity for 1112 nm as determined by a cavity photon storage ringdown measurement. The initially locked laser is suddenly turned off, giving rise to an exponential decay with a time constant related to the finesse of the cavity. We repeat this measurement for our clock laser, giving rise to a finesse of $\mathcal{F}_{1156} = 484.2(3) \times 10^3$. (**b**) By sweeping our 1112 nm laser across the cavity resonance and measuring the time-domain response on a photodetector, we are able to confirm our finesse value from the ringdown measurement performed in (a). This measurement has the advantage allowing each laser to be free-running. We repeat this measurement at 798 nm and 1156 nm (see main text for finesse values).

scheme is found in Section 2.4.6). We then abruptly turn off the light entering the cavity using an AOM and measure the decay in transmitted intensity as a function of time, making sure that the AOM switch-off occurs much faster than the expected ringdown. The observed exponential decay has a time constant $\tau = \mathcal{F}L/(c\pi)$, allowing us to extract a finesse of $\mathcal{F}_{1156} = 484.2(3)\times10^3$ and $\mathcal{F}_{1112} = 269.2(6) \times 10^3$ for our yellow and green lasers respectively[40]. Second, we measure the time-domain response in the cavity transmission as we sweep our lasers across a cavity resonance. The response of the cavity field $E(t)$ to an external laser beam with amplitude E_0, incident on the cavity, is captured by the following differential equation [184]:

$$\frac{dE}{dt} = -\frac{1}{2\tau}\left[(1 - i\nu t)E + i\eta\right], \tag{2.15}$$

where $\nu = 2\mathcal{F}\dot{\omega}/(\pi c)$ with $\dot{\omega}$ the sweep rate of the laser and $\eta = \sqrt{\mathcal{T}}\mathcal{F}E_0/\pi$, with $\mathcal{T}$ the transmissivity of the first cavity mirror. The transmitted field closed-form solution for this equation then takes the form [183]:

$$|E_T(t)|^2 = \frac{\beta^2 |E_0(t)|}{\widetilde{\nu}} \left| \sqrt{\frac{\pi}{2}} e^{-t' + i\widetilde{\nu}t'^2/2 - i/(2\widetilde{\nu})} + i\sqrt{2}D\left(\frac{i + t'\widetilde{\nu}}{\sqrt{2i\widetilde{\nu}}}\right)\right|^2, \tag{2.16}$$

with $t' = t/(2\tau)$ and $\widetilde{\nu} = 2\nu\tau$. We use Eq. (2.16) to fit the data in Fig. 2.13(b), resulting in finesses of $\mathcal{F}_{1156} = 4.6(4) \times 10^5$, $\mathcal{F}_{1112} = 2.4(2) \times 10^5$ and $\mathcal{F}_{798} = 2.6(2) \times 10^4$ for our yellow, green and blue lasers respectively [185]. The expected finesse values as calculated from the cavity mirror reflectivities measured by Menlo are $\mathcal{F}_{1156} = 3.1 \times 10^5$, $\mathcal{F}_{1112} = 1.6 \times 10^5$ and $\mathcal{F}_{798} = 2.2 \times 10^4$.

[40] At the time of measuring these values, the blue 399 nm laser had not yet been locked to the cavity and thus no ringdown measurement of the finesse was performed.

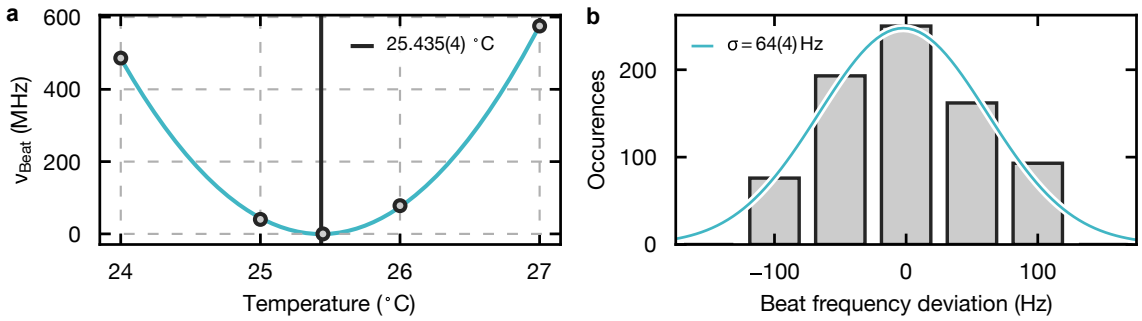

Figure 2.14 | Zero-crossing temperature. (**a**) We determine the zero-crossing temperature of our cavity by measuring the drift of a beat signal between our locked clock laser and another frequency stabilized clock laser from a neighboring lab at various cavity temperatures. A parabolic fit of the data gives a value of $T_0 = 25.435(4)°C$. (**b**) A histogram showing the frequency deviations in the beat signal between our clock laser and the frequency stabilized clock laser from a neighboring lab over a period of fifteen minutes.

2.4.3 Mode matching

In addition to resonance frequencies, the cavity also supports resonant field distributions. The behavior of these transverse electromagnetic (TEM) modes is governed in large part by the shape of the cavity mirrors. The lowest order mode (TEM_{00}) simply takes the form of a Gaussian beam and is therefore the most practically accessible. Mode-matching describes the process of shaping the light coupled into the cavity in such a way as to match the form of the TEM_{00} of the cavity. For this purpose, each of the beam paths coupled into the cavity is equiped with a telescope and an additional lens on a translation stage just prior to the vacuum chamber viewport. The 1112 nm and 1156 nm light are coupled into the cavity through the curved mirror of the cavity, while the 798 nm enters the cavity from the other side through the plane mirror. When calculating the beam propagations of each beam, we were careful to include the lensing effect of the curved cavity mirror on the beam shape. In addition, we pre-aligned each path before installing it on the cavity. The shape of the cavity mode was observed on a a beam profiler[41] and the lens positions tuned in such a way as to optimize the transmission on a nearby photodetector. Some of the observed transverse modes are shown in Fig. 2.12(c).

2.4.4 Zero-crossing temperature

Temperature fluctuations can lead to a change in the length of the reference cavity and correspondingly, a change in the cavity resonace frequencies. This is an undesirable effect which we wish to reduce as much as possible. For a given change in temperature ΔT, the relative change in the length of the cavity and resulting change in relative frequency are related in the following fashion [186]:

$$\frac{\Delta\nu}{\nu} = \frac{\Delta L}{L} = \alpha_{\mathrm{CTE}}(T)\Delta T, \tag{2.17}$$

[41] CINOGY CinCam CMOS 1201 Nano

where α_{CTE} is a temperature-dependent proportionality constant known as the temperature coefficient of thermal expansion. Our goal is to find a temperature T_0, for which α_{CTE} is minimized. Close to T_0, the solution to the differential equation

$$\frac{dL}{dT} = \alpha_{\mathrm{CTE}} L \tag{2.18}$$

can be approximated as

$$L \approx L_0(1 + a\Delta T + b\Delta T^2 + \mathcal{O}(\Delta T^3)). \tag{2.19}$$

The temperature T_0 at which the coefficient a vanishes is also known as the „zero-crossing“ temperature of the linear coefficient of thermal expansion. For ULE, the quadratic expansion factor is found to be $b \approx 1.8 \times 10^{-9}/\,\mathrm{K}^2$ [186]. To measure the zero-crossing temperature, we perform a heterodyne beat measurement between our clock laser and a second frequency stabilized clock laser from a neighboring lab. By keeping track of the drift of the beat frequency as we vary the applied temperature of the cavity, we can deduce the zero-crossing from the minimum drift range. We assume that the frequency drift of the second clock laser is negligibly small compared to the drift of the clock laser locked to our own cavity. Using the parabolic approximation as a fit for our data, we extract a zero-crossing temperature of $T_0 = 25.435(4)°\mathrm{C}$ [Fig. 2.14(a)], with an error given by the standard deviation of the parameter estimate.

2.4.5 Cavity ageing

Over time, ageing of the ultra-low expansion (ULE) glass leads to a slow change in the cavity mirror spacing. This in turn results in a continous and linear long term drift in the cavity resonance frequencies. We compensate this effect by spectroscopically probing the atomic resonance using our clock laser during several measurements over an extended period of time. From this we extract a linear drift rate of $59(1)\,\mathrm{mHz}/s$ which we continously feed forward onto our lock frequency Ω_1 (see Section 2.4.6).

2.4.6 Sideband locking

The light entering the cavity is phase-modulated using electro-optical modulators (EOMs)[42] driven at a modulation frequency $\Omega_1 = 105\,\mathrm{MHz}$ using a DDS[43] and a set of amplifiers [Fig. 2.15(f)]. This modulation frequency is then additionally phase modulated at a frequency Ω_2 by a frequency generator[44]. The resulting electric field takes the form:

$$E(t) = \sqrt{P_0}\exp\left[i\omega_c t + i\beta_1 \sin\left(\Omega_1 t + \beta_2 \sin\left(\Omega_2 t\right)\right)\right], \tag{2.20}$$

where P_0 and ω_c are the power and frequency of the light entering the EOM and β_1 and β_2 are the modulation depths of the respective modulation signals. These parameters quantify the strength with which the light is modulated and are related to the half-wave voltage V_π of the

[42] Jenoptik PM785, PM1064
[43] Wieserlabs WL-FlexDDS-NG
[44] Keysight 33600A. $\Omega_2^{798} = 35\,\mathrm{MHz}$, $\Omega_2^{1112} = 33\,\mathrm{MHz}$ and $\Omega_2^{1156} = 14\,\mathrm{MHz}$

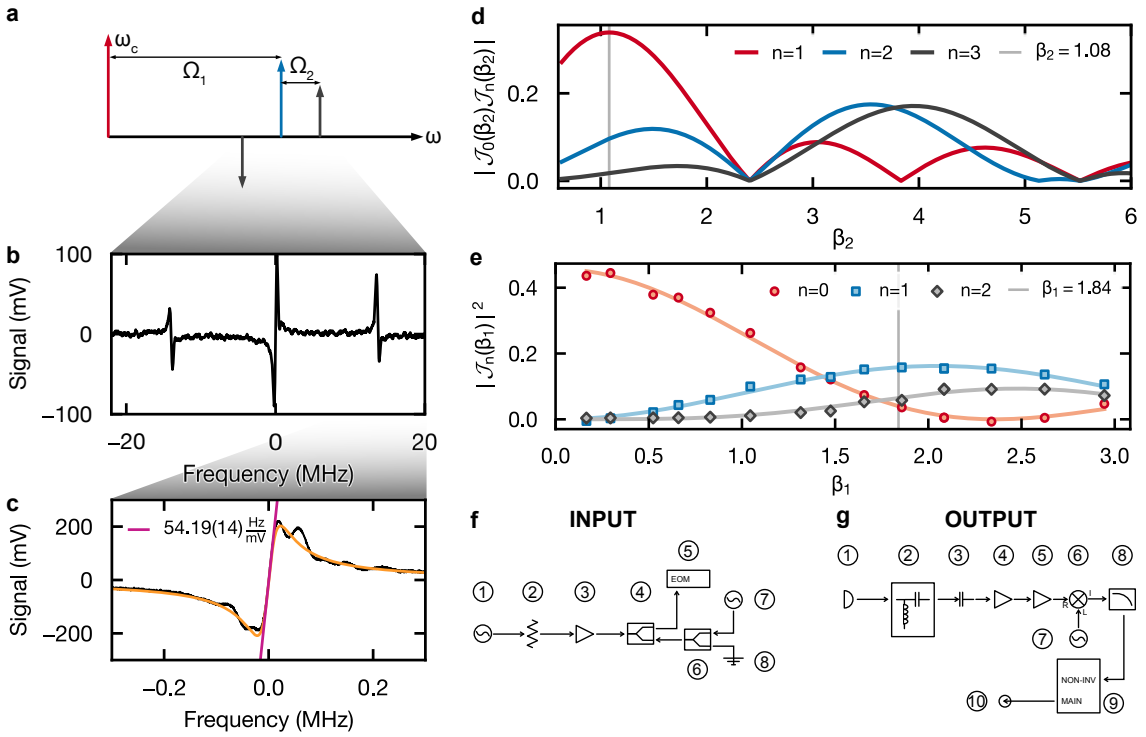

Figure 2.15 | Frequency stabilization. (**a**) Diagramatic representation of our offset sideband locking scheme. The fundamental frequeny of each of our Toptica DL-TA-SHG Pro lasers is stabilized to a sideband located at $\omega_c + \Omega_1$ (blue), generated by modulating an EOM at a frequency Ω_1 and modulation depth β_1. PDH sidebands (grey) are generated by additionally phase modulating this sideband with a frequency Ω_2 and depth β_2. (**b**) An error signal is generated by demodulating the reflected cavity signal at Ω_2 (data taken from a measurement for 1112 nm). (**c**) The slope of the error signal is given by the frequency discriminant, D, and allows us to determine the lock sensitivity according to eq. (2.21). For the 1156 nm lock, this is measured to be 54.19(14) Hz/ mV. (**d**) The optimal value of $\beta_2 = 1.08$ is found by maximizing the product of the term $\mathcal{J}_0(\beta_2)\mathcal{J}_1(\beta_2)$ (red line). Higher orders of n are shown as blue and black lines for context. (**e**) The optimal value of $\beta_1 = 1.84$ is confirmed by measuring the power residing in each sideband, given by $\mathcal{J}_1^2(\beta_1)$. This is done by observing the response of the EOM to various applied voltages in the form of the transmitted power in each sideband. Ideally, the optimal value of β_1 maximizes $\mathcal{J}_1^2(\beta_1)$ while keeping $\mathcal{J}_0^2(\beta_1)$ as small as possible. (**f**) Input locking electronics used in our lock scheme. *Numbers key*: 1. Wieserlabs DDS (105 MHz), 2. VAT-10W2+, 3. ZHL-1-2W-S+, 4. ZFSC-2-4-S+, 5. Jenoptik PM785/1064, 6. ZFSC-2-4-S+, 7. Keysight 33600A, 8. 50Ω termination. (**g**) Output locking electronics used in our lock scheme. *Numbers key*: 1. Photodetector (BW: 62 MHz), 2. ZFBT-6GW+, 3. BLK-89-S+ 4. Kuhne KU0180A, 5. ZFL-1000H+, 6. ZAD-6+, 7. Keithley 3390, 8. LPF-SLP-5+, 9. Toptica FALC, 10. Toptica DL-TA-SHG Pro DC MOD IN.

EOM (the voltage at which the EOM induces a phase shift of π on the light) via $\beta = \pi \frac{V}{V_\pi}$, where V is the voltage applied to the EOM. The modulation generates sidebands at frequencies $\omega_c \pm \Omega_1$ and an additional set of sidebands at $\omega_c \pm \Omega_1 \pm \Omega_2$, as shown in Fig. 2.15(a). By resonantly coupling the $\omega_c + \Omega_1$ (or $\omega_c - \Omega_1$) sideband into the cavity and demodulating the reflected signal at Ω_2 to generate an error signal in the standard PDH fashion [180], it is possible to lock the laser to the $\omega_c + \Omega_1$ sideband. In this way, we retain the ability to freely tune the carrier frequency by tuning Ω_1, while the laser remains locked. To optimize the frequency

stability, we want to maximize the sensitivity of our feedback loop to changes in frequency. This can be achieved by increasing the slope of the error signal, which in our locking scheme can be shown to take the form [181]

$$D(\beta_1, \beta_2) = \frac{8P_0}{\delta\nu}\mathcal{J}_1^2(\beta_1)\mathcal{J}_0(\beta_2)\mathcal{J}_1(\beta_2), \tag{2.21}$$

where $\mathcal{J}_n$ are n^{th}-order Bessel functions of the first kind. Expression (2.21) is also known as the frequency discriminant. From this expression it is clear that by finding the modulation depths β_1 and β_2 where the frequency discriminant is maximized, we optimize our lock sensitivity. Evaluating Eq. (2.21) as a function of β, we find optimum values of $\beta_1 = 1.84$ and $\beta_2 = 1.08$ [Fig. 2.15(d)], which correspond to a measured lock sensitivity of $D = 54.19(14)\,\mathrm{Hz/\,mV}$, as shown in Fig. 2.15(c). To confirm these values, we measure the optical power in each sideband as a function of the applied peak-to-peak voltage [Fig. 2.15(e)] . From this measurement, we extract a half-wave voltage V_π for each of the three EOMs, which we compare to the manufacturer specifications. The sidebands are accessed by slowly scanning each laser's output frequency while applying a modulation frequency of $\Omega_1 = 10\,\mathrm{MHz}$ to the EOM using an external signal generator[45]. We then vary the power of this modulation and measure the response of the EOM on a photodetector. The locking electronics used to modulate, and demodulate and feedback are shown in Figs. 2.15(e) and 2.15(f) respectively.

2.5 Main chamber optics

2.5.1 Zeeman slower and 2D MOT

Zeeman slower light is out-coupled close to the hot window of the atom source. We use a 1:2 telescope consisting of an $f = -100\,\mathrm{mm}$ and a $f = 200\,\mathrm{mm}$ lens to magnify the emergent beam to a waist of $\approx 3\,\mathrm{mm}$. The second lens is slightly displaced from its ideal position to focus the Zeeman slower beam into the atom source. A final $\lambda/4$ waveplate immediately infront of the hot window ensures the correct polarization for the Zeeman slower. To pre-align the Zeeman slower (without optimizing on an atomic signal), we overlapped the ingoing beam with its back-reflection from the hot-window while at the same time observing and mimizing the scattered light at the exit aperture of the Zeeman slower through the leftmost 2D MOT viewport. Next, we mounted a camera below the oven spectroscopy viewport opposite the getter pump and another close to the 2D MOT viewports and tried to observe and maximize a fluoresence signal at the resonance frequency while tuning the angle of the $\lambda/4$ waveplate.

The 2D MOT requires two large, elliptically shaped beams to maximize the interaction area with the atomic beam. To this end, the beam size is first increased using a 1:3 telescope ($f = -100\,\mathrm{mm}$, $f = 300\,\mathrm{mm}$), before being split into two branches, each of which is further magnified using a 1:5 cylindrical telescope, resulting in a beam of $w_x \times w_y \approx 33\,\mathrm{mm} \times 5\,\mathrm{mm}$. To couple these beams into the 2D MOT, we use a set of rectangularly shaped mirrors, followed by large $\lambda/4$ waveplates, situated just in front of the 2D MOT viewports for polarization

[45] Rohde & Schwarz SMB100B

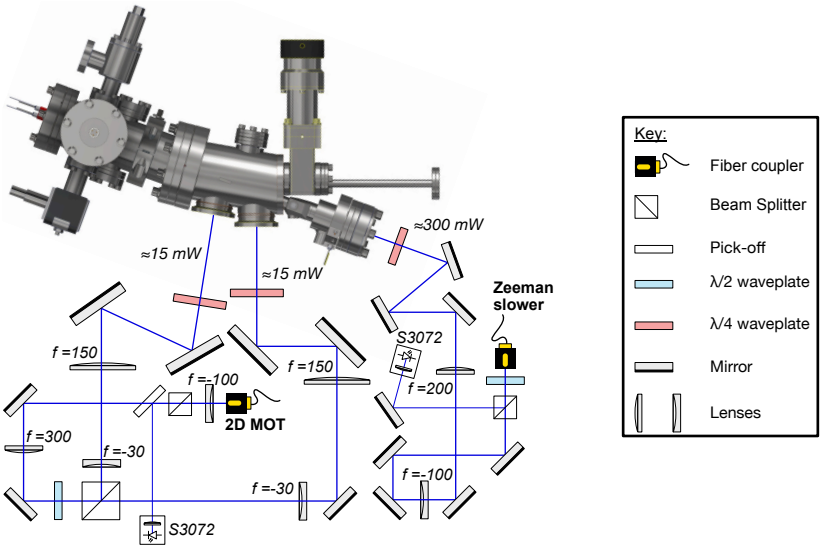

Figure 2.16 | 2D MOT and Zeeman slower setup. Two highly elliptical beams are formed for the 2D MOT by passing 399 nm light first through a 1:3 telescope and then through a set of 1:5 cylindrical telescopes (one for each branch). Each carries ≈ 15 mW of power. For the Zeeman slower we use ≈ 300 mW of blue light, which is magnified to a beam waist of ≈ 3 mm.

control. Pre-alignment is performed using using a card with a rectangular cut-out to overlap the ingoing and reflected light.

2.5.2 High-NA objective

Objective design.—Installed below our glass cell is a custom high resolution microscope objective[46] which is used to perform fluoresence imaging and to project optical tweezers onto the atoms. Though only one objective is installed, we have a second spare objective, identical in design specifications to the first and subject to all the same tests described in the following. Fluoresence imaging is performed by gathering scattered imaging light from our atoms and projecting this onto a low-noise CMOS camera[47]. An important measure for the ability of our objective to gather light is the numerical aperture (NA), defined in the following fashion [187]:

$$\mathrm{NA} = n \sin(\theta), \tag{2.22}$$

where n is the refractive index of the relevant operating medium ($n = 1$ is assumed in the following) and θ is the half-angle subtended by the arc formed by the final focusing lens of the objective. This quantity has important consequences for the diffraction limit of the objective which is defined as:

$$d = \frac{1.22\lambda}{2\,\mathrm{NA}} \tag{2.23}$$

[46] Special Optics Inc.
[47] Hamamatsu OrcaQuest

and determines the minimum distance between two objects within which they remain distinguishable as separate objects. In our magic lattice, the lattice spacing is given by $\lambda/2 \approx 379.5$ nm. For an imaging wavelength of 399 nm, this yields a minimum NA of 0.64. Our own objective possesses an NA of 0.7 and is designed to be diffraction-limited at 399 nm, 532 nm, 552 nm and 590 nm. The point-source imaging response of an objective is characterized by the so-called point spread function (PSF), which takes the form of an Airy pattern [188]:

$$I(\rho) \propto \left(\frac{2\mathcal{J}_1(\rho)}{\rho} \right)^2, \tag{2.24}$$

where $\rho = 1.22\pi(z/d)$ and $\mathcal{J}_1(\rho)$ is the Bessel function of the first kind. The diffraction limited performance of our objectives is tested at 399 nm and 532 nm by measuring the PSF and comparing to the corresponding diffraction limit. For this purpose, we use our objectives to image a 250 nm pinhole contained on a resolution test chart[48]. The results of this measurement are summarized in Figs. 2.17(a) and 2.17(b) for the objective installed in our experiment. For further details on this measurement and the objectives used in our experiment we refer the reader to Ref. [189]. Both objectives are confirmed to exhibit diffraction limited performance at the two test wavelengths. The area within which diffraction limited performance is guaranteed is known as the field of view (FOV) and in our case has been designed to a size of $\approx 100\,\mu\text{m} \times 100\,\mu\text{m}$. For a tweezer spacing of $2\lambda \approx 1.5\,\mu$m, this provides space for an array of 66×66 diffraction limited tweezers.

Mounting stage.—The distance between our objective and the surface of the stepped glass cell viewport is 1 mm for a total working distance of 14 mm. For positioning, the objective is mounted in a custom designed 5-axis stage. The objective is screwed into a titanium ring attached to an aluminium block using a set of springs. The aluminium block itself is screwed from below into the main breadboard surrounding the glass cell. Along any given translational degree of freedom, the action of these springs is counteracted by a corresponding picomotor which can be use to translate the titanium ring along the intended axis with nm resolution[49]. Titanium was chosen for its low coefficient of thermal expansion and low magnetic permeability. Similar reasoning led us to choose Ultem as the material from which to manufacture the objectives. Integrated within the mounting structure is a lens mount for focusing the lower MOT arm onto the back focal plane of the objective and a non-polarizing beam splitter (NPBS) for combining this MOT arm with the tweezer and imaging light (see Section 2.5.4 for details).

Alignment.—To fix the horizontal (xy) degrees of freedom, we aligned the objective to a guide beam which had previously been aligned onto the atoms through the bottom of the glass cell by maximizing atom loss from the MOT. To aid in the alignment, the exit pupil of the objective was equipped with an iris for the duration of the alignment procedure. Once the objective had been fixed in the horizontal plane, we aligned the tip and tilt degrees of freedom relative to the glass cell using 532 nm light. This proved difficult since we had to carefully distinguish between different back-reflections from the cell and overlap the relevant reflection

[48] Technologie Manufaktur TC-RT01
[49] Newport 8301NF for horizontal translation and Newport 8321 for vertical displacement

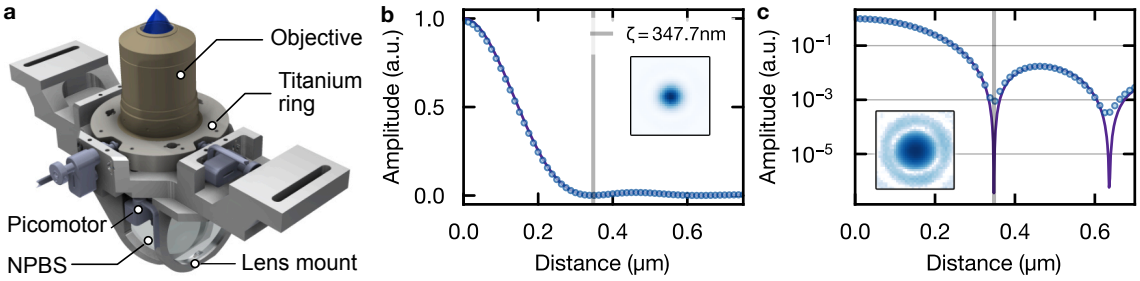

Figure 2.17 | High-NA objective. (**a**) Render of the high resolution microscope objective used in our experiment together with its 5-axis mount. (**b**) The measured PSF of our objective at 399 nm (blue datapoints) is in close agreement with the expected PSF (purple line) calculated from the Airy pattern [Eq. (2.24)] using the theoretical diffraction limit of 347.7 nm indicated by the grey line. The inset shows the image of the pinhole used to measure the data displayed in the plot. (**c**) The same data as in (b) but plotted on a logarithmic scale where the diffraction-limited performance is more clearly visible. Subfigures (**b**) and (**c**) are adapted from Ref. [189].

with the incoming beam. This problem was solved by scanning the angle of the incoming beam and observing the relative motion of the different back reflections.

2.5.3 Tweezer setup

Using our high resolution objective, it is possible to generate large arrays of tightly focused optical tweezers. While we eventually want to generate tweezer arrays at the ground and excited state tuneout wavelengths using our Vexlum lasers (see, for example, Section 5.3.1), initial tests of tweezer loading and cooling are performed using a 532 nm laser[50]. At this wavelength, large amounts of power are readily available, making it practical for generating large scalable arrays. In our experiment, we use a set of acusto-optic deflectors (AODs)[51] aligned to be orthogonal to one another, to create a regular array of diffraction orders. We control the relative spacing between these diffracted beams as well as the size and shape of the array using an arbitrary-waveform generator (AWG)[52]. AODs have the benefit of a uniform diffraction efficiency over a larger range of RF frequencies when compared to AOMs. We use a 1:1 telescope[53] placed between the AODs to image the first AOD onto the second and a further 1:10 telescope[54] to image the tweezer array onto the objective. The array is separately imaged onto a camera[55] by a 3:2 telescope, which we use for homogenization. Just before to the objective, the tweezer beam has been magnified tenfold, requiring the use of 3″ optics. Here, we are extremely careful to ensure that the final set of mirrors is sufficiently flat to avoid optically aberrated tweezers. To this end, we measure several mirrors[56] interferometrically to ensure a surface flatness of at least $\lambda/10$ using a Zygo interferometer. The selected mirrors are glued into Polaris mounts to minimize deformations and increase stability. The tweezers also pass

[50] Coherent - Verdi V18
[51] AA OptoElektronic DTSX-400-532.556
[52] Spectrum Instrumentation Corp. M4i6631-x8
[53] $2 \times f = 100\,\text{mm}$
[54] $f = 100\,\text{mm}$, $f = 1000\,\text{mm}$ ACT508-1000-A
[55] AlliedVision Alvium 1800 U-1240 mono C-Mount
[56] Thorlabs BB3-E02

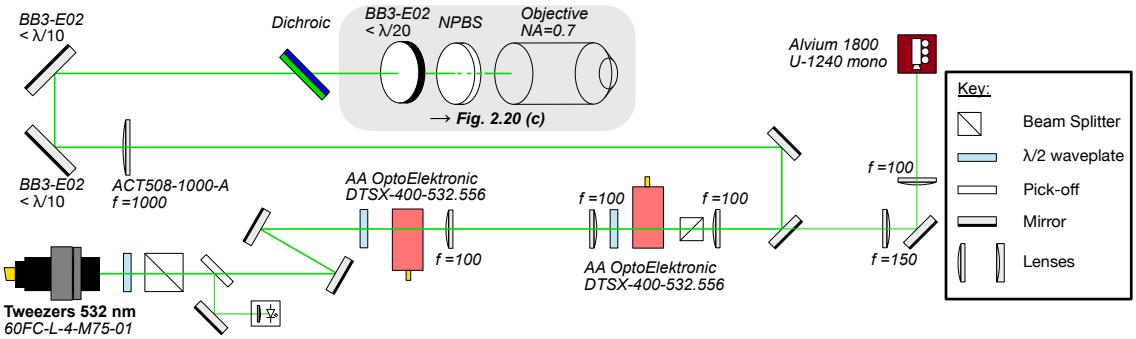

Figure 2.18 | Tweezer setup. The output of a 532 nm high-power laser is coupled through a PCF fiber onto the main experiment. To generate tweezer arrays, this light subsequently passess through two orthogonal AODs, separated by a 4*f* imaging system. Part of the tweezer light is further imaged on a camera for monitoring and homogenization. The majority of the tweezer light, however, is magnified tenfold before being reflected into our high resolution objective. This focuses the tweezer light at the position of the atoms.

through a narrow band dichroic which acts to separate them from the imaging wavelengths of 399 nm and 556 nm. Using the same Zygo interferometer as before, we find that by gluing the dichroic into its mount at only one corner, the surface flatness is optimized.[57] We bring 532 nm light onto our experiment table using a 4 m long PCF fiber[58] and align our AODs for a maximum diffraction efficiency of $\gtrsim 90\%$ using 5-axis stages[59]. The tweezer beam is intensity stabilized in the fashion described in Section 2.3.1 and the individual tweezer intensities are homogenized on the percent level by feeding back to the AODs on camera images of the tweezer array. To generate a sensible feedback signal, we employ an algorithm which iterates alternatingly between mean and random sampling methods to calculate a balancing error at each tweezer site [66].

2.5.4 Glass cell optics

Around our glass cell optics of various kinds are needed to shape and manipulate each beam path properly. In the following we provide an overview and rationale for each of these paths. One note of general interest is that every beam path is intensity stabilized. This is accomplished by feeding back the light picked off and collected on a photodector after each fiber, to an intensity servo, which in turn is connected to the corresponding AOM for that path. Unless stated otherwise, the photodetectors are custom built based on an existing design taken from Ref. [190]. The entire set of optics is visualized schematically in Fig. 2.19.

MOT optics.—Our 3D MOT consists of two orthogonal retro-reflected 556 nm beams in the horizontal (xy) plane [Fig. 2.19] and two independent counter-popagating beams along the vertical z-axis [Fig. 2.20(c)]. Each axis employs a $f = 75$ mm collimator[60] to bring the diameter of the beam to ≈ 10 mm. MOT arm 1 is required to propagate through our microscope objective.

[57] Using NOA61 UV curing glue from Thorlabs.
[58] NKT-LMA-PM-15
[59] Newport 9081-M
[60] Schäfter+Kirchhoff GmbH 60FC-L-4-M75-01

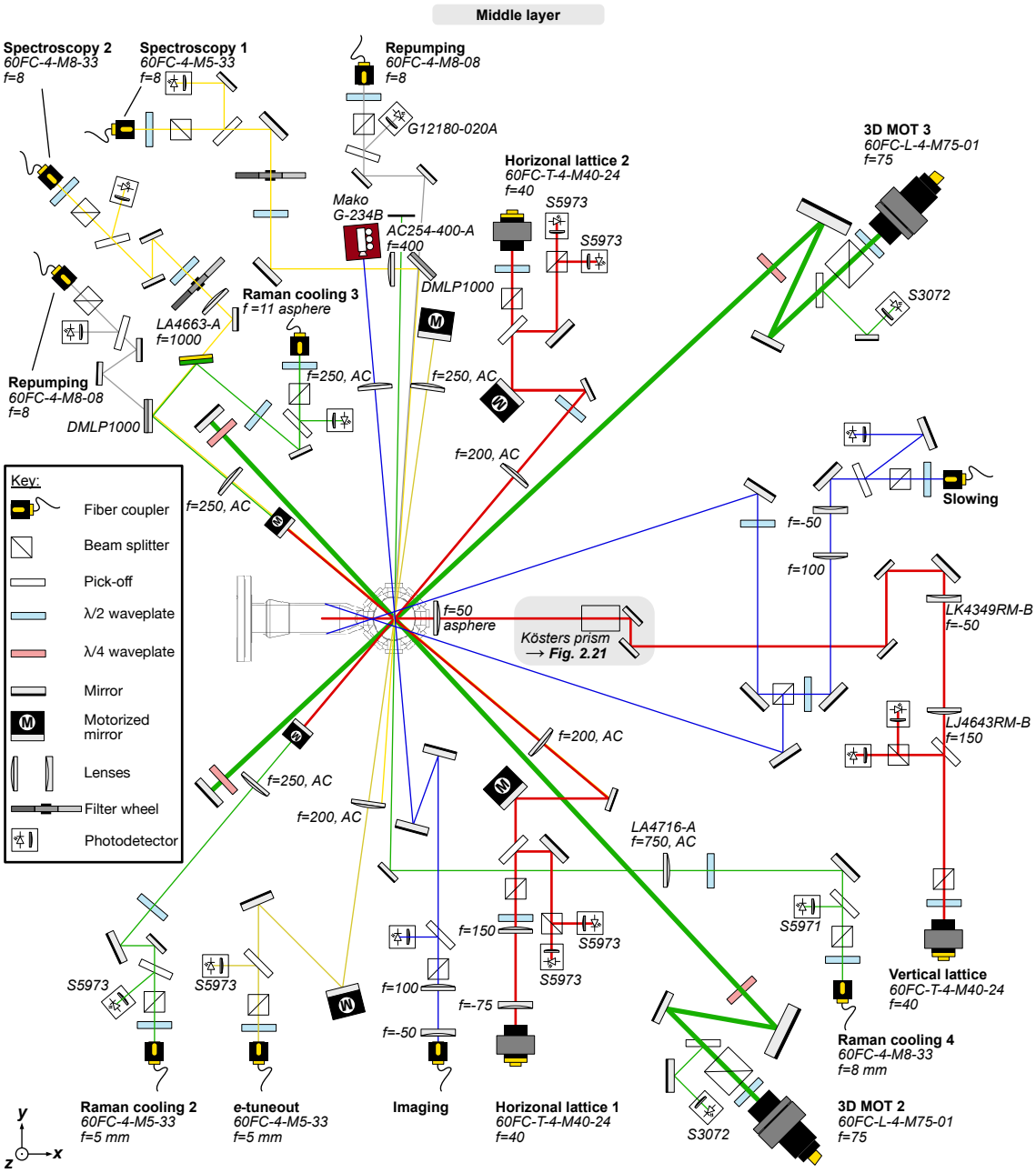

Figure 2.19 | **Glass cell optics.** Setup of all optics surrounding our glass cell in the middle layer (horizontal plane) at the time of the writing this thesis. Beam paths such as the additional MOT arms 1 and 4, as well as Raman cooling beam 1 are oriented vertically and contained in Fig. 2.20. For details regaring each beam path, the reader is referred to the main text.

To ensure the correct beam size at the location of the atoms, the light in this arm is focused onto the back focal plane of the objective using a 3" $f = 150$ mm lens [Fig. 2.20(b) and 2.20(c)].

Horizontal lattice.—Each of the two horizontal lattices is generated by the light from one of our 759 nm ti:sapphs, focused down to a $1/e^2$ beam waist of $w_0 \approx 35\,\mu$m and retroreflected from a curved mirror. The curved mirrors act as lenses to re-focus the retro-reflection at the

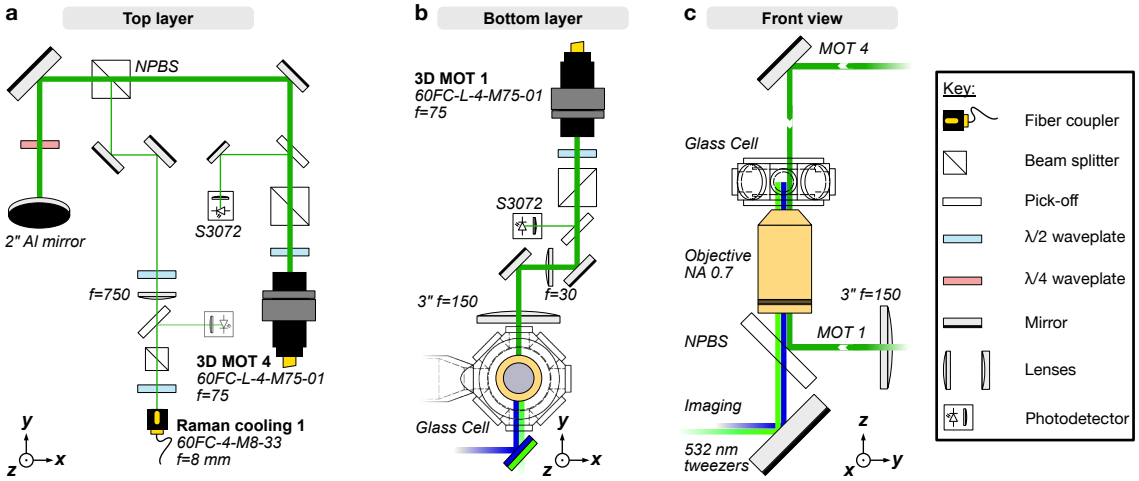

Figure 2.20 | Glass cell optics. (**a**) Top layer of optics, mounted on breadboard above glass cell. MOT arm 4 is combined with one of the Raman cooling beams and reflected downwards into the glass cell using an aluminium mirror. (**b**) Bottom layer of optics mounted below glass cell. MOT arm 1 is magnified by a $f = 30$ mm lens, before being focused onto the back focal plane of the objective using a 3" $f = 150$ mm lens. (**c**) Front view showing the vertical propagation of MOT beams 1 and 4 as well as the tweezer and imaging light.

position of the initial focus. These two lattice axes intersect at right-angles to each other, but are offset in their respective frequencies on the order of hundreds of MHz to avoid unwanted interference (note that day-to-day, these lasers are not locked to the wavemeter). To align the lattice arms, we use a set of motorized mirror mounts. The retro-reflected lattice light is coupled back into its respective pcf fiber and this return signal is picked off on the in-coupling side and the read-out by a photodetector [Fig. 2.10(a)]. By maximizing the signal on the photodetector we ensure good alignment within each lattice arm. The translational degree of freedom of each arm is fine-tuned by moving a $f = 200$ mm achromatic focusing lens using a dedicated translation stage[61].

Vertical lattice.—To complete our 3D lattice geometry, we implement a vertical lattice to confine atoms in the direction of gravity. Ideally, this vertical lattice would propagate orthogonally to both horizontal lattices. The placement of our high-NA objective prevents this ideal configuration and so we pursue and alternative approach wherein a vertical lattice is generated by interferring two running wave laser beams at a relative angle in the zy-plane [see figure Fig. 2.21(a)]. In our case, this angle is geomtrically constrained to $\leq 20°$ by the small glass cell viewport through which both beams must pass. To reduce the influence of noise on the differential path length of the running wave beams we use a Kösters prism[62] to split the lattice laser light into two parallel collimated beams [191]. These are then brought to interference by a final $f = 50$ mm focusing lens just infront of the glass cell viewport. The Kösters prism is a monolithic component and thus offers a high degree of passive phase stability. It is also capable of handling large amounts of optical power, making it less susceptible to thermal noise or distortion. The prism along with the final focusing lens is mounted on several

[61] Standa 7T67-6-9S35M-5
[62] B. Halle Nachfl. GmbH - IKP 040

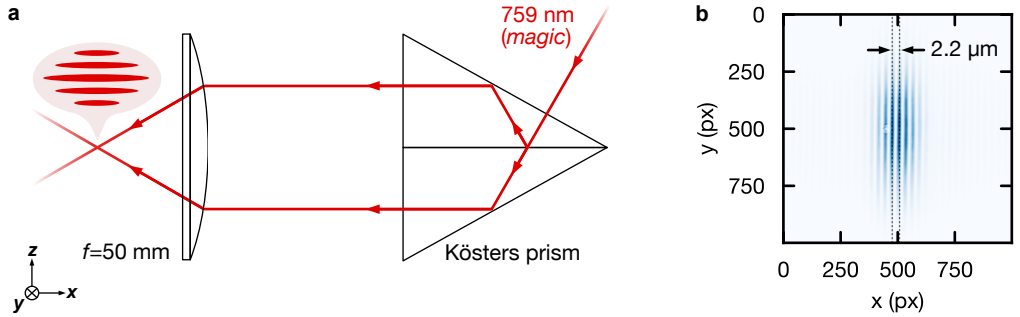

Figure 2.21 | **Vertical lattice.** (**a**) Schematic drawing of the vertical lattice architecture. The lattice light is split into two parallel beams using a Kösters prism. These beams are focused through a lens and brought to interference, thus creating a lattice along z. (**b**) Camera image of the vertical lattice during pre-alignment. We observe a layer spacing of 2.2 µm, as intended. The maximum trap depth achieved in this lattice is calculated at ≈ 40 kHz.

translation stages to allow for accurate positioning and alignment of the beam foci. During pre-alignment, we measured a lattice beam size at the focus of $\approx 18\,\mu\text{m} \times 54\,\mu\text{m}$ with a layer separation of $\approx 2.2\,\mu\text{m}$. At maximum power, our vertical lattice is calculated to possess a harmonic oscillator frequency of around 40 kHz.

Spectroscopy.—Currently, two spectroscopy beams are employed in our experiment, both running at 578 nm. The first spectroscopy beam („Spectrocsopy 1“ in Fig. 2.19) is in some sense a historical remnant, harking back to the time when we used a 1D optical lattice along the y-axis.[63] By contrast, our second spectroscopy beam („Spectroscopy 2“) is aligned to be counterpropagating with horizontal lattice axis 1. Spectroscopy 1 uses a $f = 400\,\text{mm}$ lens to focus light down to a waist of $w_0 \approx 220\,\mu\text{m}$ at the location of the atoms. For Spectroscopy 2, we decided to combine an $f = 250\,\text{mm}$ lens with an additional weakly focusing $f = 1000\,\text{mm}$ lens to further reduce the beam waist at the focus to $w_0 \approx 130\,\mu\text{m}$. This was done to enhance the Rabi frequency. Each spectroscopy path is equipped with a filter wheel that allows us to selectively reduce the yellow laser power incident on the atoms and thus reduce the effect of power broadening on the transition linewidth.

Repumping.—We co-align a set of repumping beams with our spectroscopy beams. This ensures that during sideband cooling, the recoil imparted by the repumping beams occurs along the same direction as the cooling (i.e. no heating occurs along directions that cannot be cooled). For the purpose of overlapping the repumper beams with the spectroscopy light, we make use of 1″ longpass dichroic mirrors.[64]

Imaging.—Prior to entering the glass cell, our 399 nm absorption imaging beam is magnified by a 1:2 telescope after exiting the fiber collimator, to ensure a homogeneous illumination across the atomic sample (see Section 3.1.1 for details). Our imaging camera is a Mako G-234B with a Sony IMX249 CMOS sensor, exhibting a monochrome quantum efficiency of $\sim 52\%$ at 399 nm.

Slowing.—We use two 399 nm beams, crossing under an angle of 22.5°, to slow atoms prior to entering the 3D MOT, thereby increasing our MOT loading rate [192]. To prevent heating of atoms in the MOT, the intersection of these two beams is offset from the MOT by ≈ 17.5 mm.

[63] See, for example, our state-dependent wavelength measurements in Chapter 4.
[64] Thorlabs DMLP1000

e-tuneout.—For measurements of the excited state tuneout wavelength, we create a shallow 1D lattice using 575 nm light from one of our Vexlum lasers (see also Section 4.5).

Raman cooling.—The presence of a non-vanishing nuclear spin and the concomitant appearance of hyperfine states in the fermionic isotopes of Yb, permits Raman sideband cooling to bring atoms into the motional ground state [66]. For this purpose, four separate 556 nm beams are required. These are necessary to address the correct σ and π transitions in our 3D lattice. The light for these beams is produced by a 556 nm Toptica TA-Pro beat-locked to our main green laser system (Section 2.3.2). As of the writing of this thesis, this setup is incomplete.

CHAPTER 3

Experimental methods

A typical run of our experiment proceeds according to a precisely determined sequence of events. First, hot and fast ytterbium atoms are initially slowed, captured and cooled in a MOT. Subsequently, the MOT is compressed and the atoms loaded into tweezer arrays or optical lattices. To prepare some desired initial state, the atoms are further cooled in the optical lattice using a variety of different techniques. Then, dynamical evolution of the system is allowed to occur for some time, after which, the atoms are interrogated spectroscopically to observe their final state. At this point, recourse is made to one of several imaging techniques. All of this takes place in less than one second. It is the purpose of this chapter to break down that one second into bite-sized chunks, each relating to a different stage in the above described sequence of events.

3.1 Imaging

Imaging techniques of various kinds are used in our experiment to extract relevant information about the size, temperature, location and state populations of our atomic sample. In this section we explain the principles involved in these imaging techniques and explain how they are realized in our experiment.

3.1.1 Absorption imaging

To measure the density distribution of our atomic sample, we make use of absorption imaging. The absorption of resonant light by our atomic ensemble attenuates the transmitted light intensity, thus casting a shadow which can be captured on a camera and used to deduce the density of the ensemble. This simple idea can be cast into the form of a differential equation

$$\frac{dI}{dy} = -n(x, y, z)\sigma_0 I, \tag{3.1}$$

where σ_0 is the resonant scattering-cross section of our atoms and captures the probability with which a scattering event will occur, and $n(x, y, z)$ is the local density of our atomic sample. By integrating this equation, we find that the attenuation of the initial intensity I_0

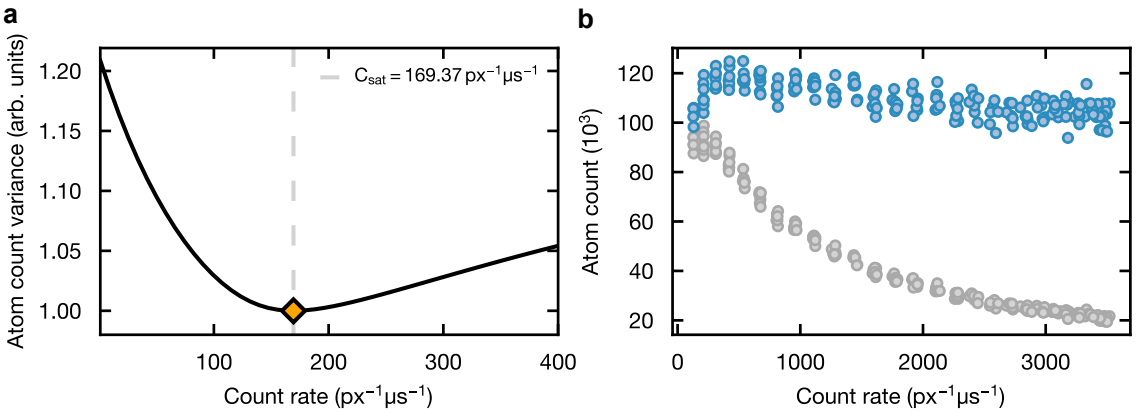

Figure 3.1 | High-intensity imaging calibration. (**a**) By recording the variance in atom count data for different imaging intensites incident on identical atomic samples, we are able to calibrate the count rate saturation factor $C_{\text{sat}} = 169.37\text{px}^{-1}\mu\text{s}^{-1}$ (see main text for details). (**b**) After calibration, the initially intensity-correlated atom count data (grey) is independent of the imaging light power (blue).

increases exponentially along the direction of light propagation in a fashion described by the Lambert-Beer law [193]:

$$I(x,z) = I_0(x,z)e^{-\sigma_0 \int dyn(x,y,z)}, \tag{3.2}$$

where I_0 is the initial intensity incident on the atomic ensemble. The column density, i.e., the integrated local density, is then given by

$$n(x,z) = -\frac{1}{\sigma_0}\ln\left(\frac{I(x,z)}{I_0(x,z)}\right), \tag{3.3}$$

such that, in principle, it is sufficient to capture two images: one of the imaging light with no atoms (bright image) and one image with the atoms present (atom image). In practice, we capture a third (dark) image without atoms and where the imaging light is turned off. This is then subtracted from both the bright and atom images to calibrate out the dark counts. The non-linear nature of expression (3.3) guarantees that this is a non-trivial offset.

3.1.2 High-intensity imaging calibration

So far we have assumed that the intensity of light incident on our atoms is much smaller than the saturation intensity, $I \ll I_{\text{sat}}$.[1] This assumption was implicit in our use of the resonant scattering-cross section in Eq. (3.1), but cannot be guaranteed in all measurements. We account for this fact by working with a modified effective scattering cross section

$$\sigma_{\text{eff}} = \sigma_0 \frac{1}{1 + \frac{I(x,y,z)}{\alpha I_{\text{sat}}}}, \tag{3.4}$$

[1]The saturation intensity is that intensity for which the absorption coefficient of a medium (i.e. the exponent of the Lambert-Beer law) is halved. It is defined as $I_{\text{sat}} = \pi hc/(3\lambda^3\tau)$, where τ is the lifetime of the excited state. For the $^1S_0 \leftrightarrow {}^1P_1$ transition in Yb, $I_{\text{sat}} \approx 60\,\text{mW/cm}^2$.

where α is a numerical factor compensating for imperfect imaging beam polarization and the multi-level atomic structure. In this way, we obtain a modified version of the column density [194]:

$$n(x,z) = -\frac{1}{\sigma_0}\left[\ln\left(\frac{I(x,z)}{I_0(x,z)}\right) + \frac{I(x,z) - I_0(x,z)}{\alpha I_{\text{sat}}}\right]. \tag{3.5}$$

It is a simple matter to relate this expression to the counts detected by the camera $C(i,j)$ [195]:

$$n(i,j) = -\frac{A}{\sigma_0}\left[\ln\left(\frac{C(i,j)}{C_0(i,j)}\right) + \frac{C(i,j) - C_0(i,j)}{C_{\text{sat}}}\right], \tag{3.6}$$

where A is the pixel area and (i,j) its coordinates. C_{sat} is an unknown calibration factor which we determine experimentally. To this end, we make use of the fact that the atom number is independent of the imaging intensity to repeatedly prepare the same atomic sample while varying the imaging intensity and observing the results of each iteration on our camera. From this data, $C_{\text{sat}} = 169.37\text{px}^{-1}\,\mu\text{s}^{-1}$ is determined as the minimum of the atom count variance [Fig. 3.1(a)]. During this calibration measurement, we are careful to ensure that the imaging light penetrates the atomic cloud even at the lowest imaging intensities. Using our calibrated count rate, we observe that the atom number recorded by the camera is now independent of the incident imaging light intensity [Fig. 3.1(b)]. This is in contrast to the correlated data observed prior to the calibration. An alternate calibration scheme would be to use a second camera to track the induced recoil from the imaging light on the atoms. By comparing the point at which the velocity saturates to the amount of light incident on the camera to be calibrated, it is possible to extract C_{sat} [195].

For each of the three images we take during absorption imaging we restrict the region of interest (ROI) to reduce unecessary overhead in the file size while still capturing the entire cloud in the atom image. In the bright and atom images, we additionally record a background region by sampling the edges of the ROI. This is done to compensate for changes in the imaging beam intensity between the two images.

3.1.3 Time-of-flight imaging

The magnification of our imaging optics necessitates a calibration of the effective pixel size. For this purpose, we employ time-of-flight (TOF) imaging and measure the free-falling acceleration of our atoms. In principle, this should match the acceleration due to gravity and any discrepancies are attributed to the uncorrected pixel area. During TOF imaging an initally trapped atomic sample is released and allowed to expand freely while absorption images of the sample are taken at regular intervals [Fig. 3.2(a)]. The centroid of the atom cloud follows a classical trajectory defined by:

$$y(t) = y_0 - \frac{1}{2}gt^2, \tag{3.7}$$

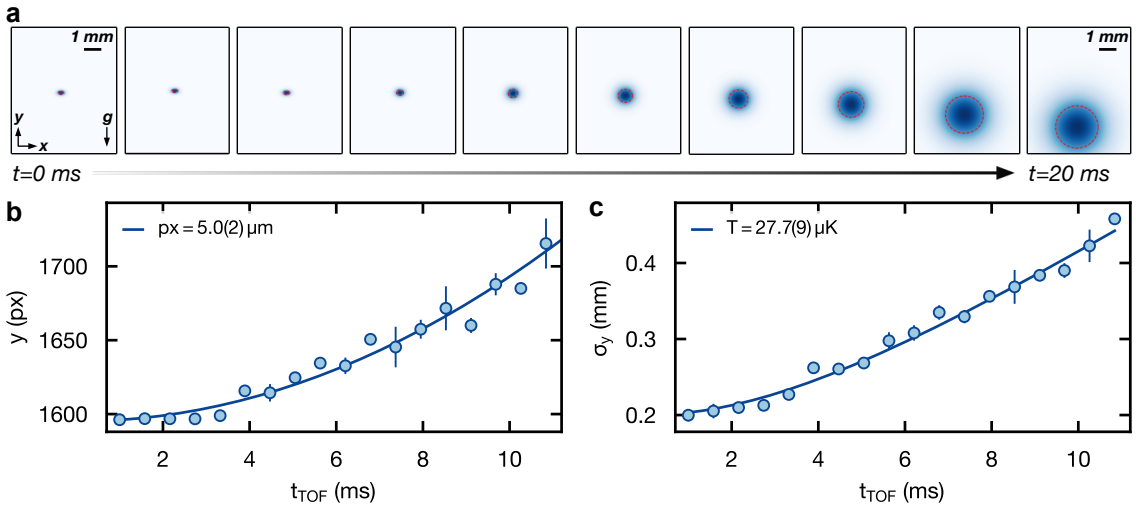

Figure 3.2 | **Time-of-flight imaging.** (**a**) Absorption images of the expanding atomic cloud after sudden release from our MOT. By fitting a 2D Gaussian (red dashed circle) to our cloud we keep track of the cloud size and center position as a function of time. (**b**) The cloud center as a function of time allows us to measure the acceleration of the cloud. By comparing this to the acceleration due to gravity (the solid line is a fit of Eq. (3.8)), we are able to calibrate our camera's pixel size to be 5.0(2) µm. (**c**) The cloud widths extracted from the Gaussian fits in (a) provide access to the temperature of the cloud. A fit of Eq. (3.7) to this data (solid line) gives a value of T= 27.7(9) µK for the temperature of the atomic sample.

where y_0 is the initial y-coordinate of the cloud center and g is the acceleration due to gravity. By fitting a 2D Gaussian to our atom cloud, we keep track of the cloud center. This in turn allows us to calibrate our pixel size by comparing the acceleration of the cloud center with the acceleration due to gravity [Fig. 3.2(b)].

We can further make use of TOF imaging to determine the temperature of our atomic sample. We assume our atoms to be non-interacting and thermally distributed, giving rise to ballistic expansion of the atomic cloud after quenching off the trap potential. The size of the cloud as a function of time is then given by [196]:

$$\sigma(t) = \sqrt{\sigma_0^2 + \frac{k_B T}{m} t^2}, \tag{3.8}$$

with σ_0 the initial cloud size, k_B Boltzmann's constant, T the temperature of the cloud and m the atomic mass [Fig. 3.2(c)].

3.1.4 State-selective imaging

We extend the absorption imaging scheme described at the beginning of this chapter to encompass the separate imaging of ground and excited state atoms of our clock transition. For this purpose, we initially take an atom image as before, but now add a separate 399 nm, 3.5 mW „blowout" pulse lasting 50 µs to ensure that no atoms remain in the ground state before we repump our excited state atoms. Importantly, our camera is triggered to read out this blowout pulse as an image so as to ensure that it is „clean" before taking the next image (the camera continously accumulates photons until it is read out). This adds an additional 12 ms wait time

to our sequence. After this blowout pulse, we repump our atoms for 3 ms from the excited state and take another image, followed by the usual bright and dark images. In this way we can directly determine the fraction of atoms in each state.

3.1.5 Fluoresence imaging

Fluoresence imaging makes use of our high resolution microscope objective to capture light sacttered off our atoms and project it onto a low-noise CMOS camera[2]. The benefits of this method compared to absorption imaging include a greater signal-to-noise (SNR) ratio and a higher resolution, in principle allowing for single-site imaging of atoms in our optical lattices. One significant drawback is the increased time required for this imaging method. This is usually limited by the rate of scattered photons and the readout time of the camera. To counteract these limitations, cooling the atoms during imaging may be employed to increase the photon scattering rate. Another option is to increase the sensitivity of the camera and its readout speed. Compared to the established electron multiplying charge-coupled device (EMCCD) cameras used in many cold atom experiments for the purpose of fluoresence imaging, our CMOS camera has the advantage of parallel sensor readout, thus significantly reducing its readout time. Our camera has a quantum efficiency (QE) of $\approx 83\%$ at 399 nm with a pixel size of $4.6\,\mu\text{m} \times 4.6\,\mu\text{m}$. The imaging system consists of our high-NA objective with a focal length of 24.97 mm and a $f = 500$ mm achromatic lens yielding a magnification of $\times 20$.

Our camera is operated in its „global shutter“ mode and a single exposure lasts 20 ms, during which time we illuminate the atoms using resonant 399 nm light. We arm the camera some 250 ms prior to exposure, during which time, photons accumulate on the camera sensor from other light sources in the sequence (e.g. MOT or lattice beams). This background must be subtracted from the captured frames since the camera is not „self-cleaning“ prior to exposure. We observe this background signal to be spatially homogeneous across the sensor, which allows us to use the edge of the camera frame for background subtraction. State-selective imaging is performed with the same basic pulse scheme as that described in Section 3.1.4, though in this case the blowout pulse and the ground state imaging pulse are one and the same. We also adjust the pulse durations to account for the differing specifications of the OrcaQuest compared to the Alvium camera used for absorption imaging.

3.2 A MOT of bosonic ytterbium

A fundamental pre-requisite for performing any quantum simulation experiments with cold neutral atoms is the creation of a MOT [197, 198]. The presence of narrow intercombination transitions in the level structures of AELs provides the opportunity for MOTs with lower Doppler temperatures when compared to their alkali counterparts. However, this advantage is negated to some degree by the reduced capture efficiency of narrow-line MOTs. For this reason, many AELs employ a two-stage MOT architecture, initially trapping a large fraction of atoms using a broader line, such as the ${}^1\text{S}_0 \leftrightarrow {}^1\text{P}_1$ transition, before switching to the narrow-line MOT.

[2] Hamamatsu OrcaQuest

This increases the technical difficulty of the MOT by having to take care of two transitions while also guaranteeing an efficient handover between the MOT stages. In this regard, one of the advantages of ytterbium over other elements with a similar level structure is the relatively broad linewidth of the $^1S_0 \rightarrow {}^3P_1$ intercombination transition. This means that ytterbium occupies a happy medium between efficient trapping and low achievable temperatures. In fact, the scattering rate from the 182 kHz intercombination line is large enough to effectively capture atoms without needing to resort to a two-stage MOT scheme at all. This is precisely what we do in our own experiment. However, to enhance the MOT loading rate further, we add an additional region of slowing using two blue beams crossing at 22.5° with respect to one another based on a scheme first employed by Plotkin-Swing *et al.* [192]. Each slowing beam operates at ≈ 8.4 mW of power with a beam waist of 3 mm. This crossed beam slowing region is spatially separated from the 3D MOT by 17.5 mm to avoid heating atoms out of the trap due to scattering of blue light. At the location of the atoms, each MOT beam has a $1/e^2$ diameter of ≈ 10 mm. In the horizontal plane our MOT beams are retro-reflected, while in the vertical direction, we use two independent counterpropagating beams. This geometry is necessitated by the presence of our high-NA microscope objective, mounted below the glass cell, as detailed in Section 2.5.4. By using appropriate output couplers[3], we circumvent the need for large telescopes in our beam paths. To ensure the correct collimated beam size from the MOT beam propagating through the objective, we focus the light in this arm onto the back focal plane of the objective using a 3 inch, $f = 200$ mm lens. During MOT loading, the power in each horizontal arm is stabilized to 30 mW, while in the vertical direction, the effect of gravity leads us to maintain the lower MOT arm at 22.5 mW compared to only 7 mW in the top arm. We combine this with a magnetic field gradient of $\partial B/\partial z \approx 5.5\,\mathrm{G/cm}$. With this configuration we load $\approx 14 \times 10^6$atoms/s of ^{174}Yb under normal operating conditions.

3.2.1 MOT compression

The majority of our experiments require atoms to be loaded from our MOT into optical lattices or tweezer arrays. However, after the inital loading stage, our MOT is much too dilute to ensure an efficient transfer of atoms to lattices or tweezers. To solve this problem, we spatially compress our MOT to a much smaller size, thereby drastically increasing its density.

A MOT relies on the interplay of dissipative and conservative forces to cool and trap atoms [198]. In abstraction, a MOT can be treated in a similar fashion to a damped harmonic oscillator where the total force experienced by the atoms along one dimension takes the form:

$$F = -\beta v - \kappa z. \tag{3.9}$$

Here, $\beta = \beta(I, \delta)$ acts as a intensity and detuning dependent viscous damping coefficient corresponding to dissipative dynamics, and κ is the spring constant of the trap responsible for

[3] Schäfter&Kirchhoff 60FC-L-4-M75-01

the scaling of the conservative force component. The latter is related to the applied magnetic field gradient $\partial B/\partial z$ in the following fashion [199, 200]:

$$\kappa = \frac{g_J \mu_B}{\hbar k} \frac{\partial B}{\partial z} \beta, \tag{3.10}$$

where g_J is the Landé g-factor of the relevant transition, μ_B is the Bohr magneton and $k = 2\pi/\lambda$ is the wavenumber. The force described by Eq. (3.9) slows down the motion of the atoms, thereby reducing their average kinetic energy. Despite the absence of a thermal equilibrium in this system, it is convenient to define a temperature for the atomic sample via the equipartition theorem in the following fashion [198]:

$$\frac{1}{2} k_B T = \frac{1}{2} \kappa \langle r^2 \rangle, \tag{3.11}$$

where $\langle r^2 \rangle$ is the root-mean-square (rms) cloud radius. Assuming a dilute and thermally distributed cloud, this equation allows us to derive the following scaling behaviors for the cloud size and velocity [201]:

$$r \propto \sqrt{I}/\sqrt{\partial B/\partial z} \tag{3.12}$$

$$v \propto \sqrt{I}/\sqrt{\delta}. \tag{3.13}$$

Hence, to reduce the phase space density of our atomic sample, it is necessary to decrease the intensity of the trap light while increasing the magnetic field gradient. In our own experiment, this compression is performed by ramping the magnetic field gradient to $\approx 24\,\mathrm{G/cm}$ within 100 ms while simultaneously reducing the power in the MOT beams by two orders of magnitude and ramping our detuning closer to resonance. Currently, this means starting at a detuning of $\delta = \omega_L - \omega_0 = -3.05\,\mathrm{MHz}$ and ramping to $\delta = -1.45\,\mathrm{MHz}$ for 3D MOT 2 through 4 and $\delta = -2.2\,\mathrm{MHz} \rightarrow -1.28\,\mathrm{MHz}$ for 3D MOT 1. Ramping the detuning is necessary to compensate for a narrowing of the power-broadened transition linewidth with decreasing laser intensity.

3.3 Spectroscopy

Spectroscopy is a vital tool for atomic physicists, allowing us to detect the frequencies of atomic transitions with a high degree of precision. In ytterbium, the ultra-narrow clock transition presents an especially sensitive spectroscopic probe. Optical lattice clocks have exploited this sensitivity to spectroscopically interrogate atoms on frequency scales approaching those where certain theories predict temporal variations in the fundamental constants of nature [41, 202]. In the context of this thesis, several spectroscopic methods are employed, the majority of which make use of optical lattices to confine atoms during spectroscopy, thus limiting motional effects and allowing for a greater frequency precision.

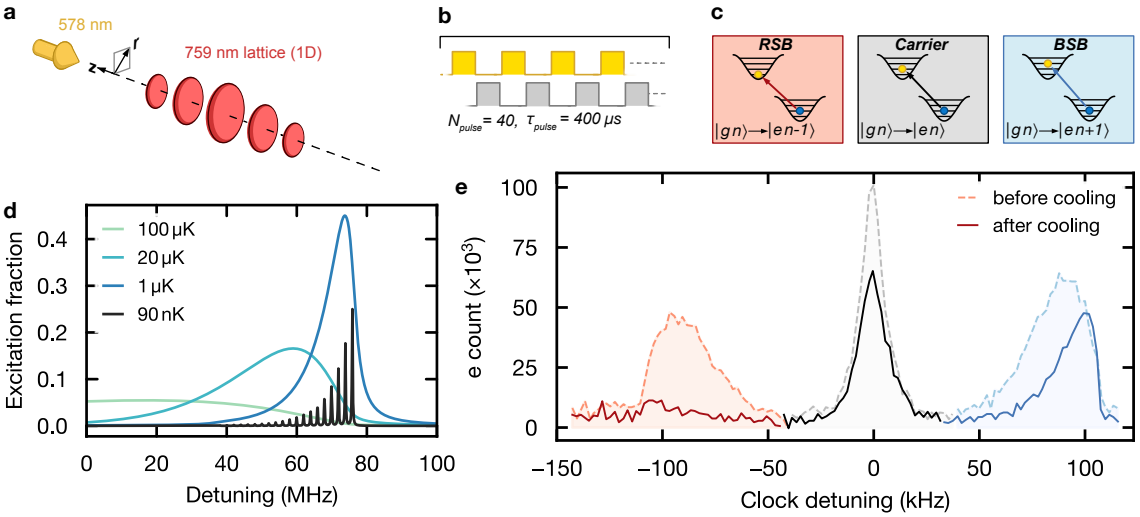

Figure 3.3 | Sideband spectroscopy and cooling. (**a**) Setup for sideband spectroscopy and cooling in 1D. Atoms are loaded into a magic lattice formed by a retro-reflected 759 nm laser beam. The atoms are interrogated using a narrow clock line laser at 578 nm propagating along the axial (z) direction. Cooling is faciliated by the same laser in combination with repumping light. (**b**) Schematic of one sideband cooling cycle consisting of fourty alternating 400 µs sideband and repumping pulses. (**c**) Illustration of the different transitions adressed during sideband spectroscopy. The red sideband (RSB) is used to facilitate cooling. (**d**) A plot of the blue sideband for different radial temperatures. Only for sufficiently low radial temperatures is it possible to resolve individual axial lattice bands [203]. (**e**) Sideband spectrum before (dashed lines) and after (solid lines) sideband cooling according to the sequence illustrated in (b). The reduced temperature is visible from the reduced prominence of the red sideband compared to the blue sideband.

3.3.1 Sideband spectroscopy

To probe the temperature of atoms in our optical lattice, we make use of sideband spectroscopy. Atoms are initially loaded into a 1D lattice at the 759 nm magic wavelength and light from our ultra-narrow 578 nm clock laser is aligned onto the tightly-confined axis of this lattice [Fig. 3.3(a)]. By scanning the frequency of the clock laser around the $^1S_0 \rightarrow {}^3P_0$ resonance, we address transitions to different motional states. Specifically, we are able to resolve a narrow carrier transition which preserves the motional quantum number ($|g,n\rangle \rightarrow |e,n\rangle$), as well as a blue ($|g,n\rangle \rightarrow |e,n+1\rangle$) and red sideband ($|g,n\rangle \rightarrow |e,n-1\rangle$), corresponding to raising and lowering by one motional quantum number [Fig. 3.3(c)]. We assume the atoms to be thermally distributed so that the mean occupation $\overline{n}$, is determined by the axial temperature T_z of our sample according to:

$$\overline{n} = \frac{\sum_{n_z=0}^{\infty} n e^{-n\hbar\omega_z/(k_B T_z)}}{\sum_{n_z=0}^{\infty} e^{-n\hbar\omega_z/(k_B T_z)}}. \tag{3.14}$$

The colder the sample, the more atoms populate the lowest motional state. For these atoms, no excitation on the red sideband is possible and hence, the fraction of atoms in this sideband decreases. Ideally, if all atoms populate the motional ground state, we should see the red

sideband disappear all together. This suggests a relation between the sideband areas and the mean occupation, and indeed, it can be shown that [66, 204]

$$\overline{n} = \frac{A_{\text{rsb}}}{A_{\text{bsb}}} \frac{1}{1 - (A_{\text{rsb}}/A_{\text{bsb}})}, \tag{3.15}$$

where A_{rsb} and A_{bsb} are the areas of the red and blue sideband respectively. It follows that the axial temperature can be determined simply by comparing the size of the sidebands:

$$T_z = \frac{\hbar\omega_z}{k_B} \frac{1}{\ln(A_{\text{bsb}}/A_{\text{rsb}})}. \tag{3.16}$$

This requires prior knowledge of the axial trap frequency ω_z. In principle, this quantity can also be determined from sideband spectroscopy since the trap frequency is directly related to the location of the sidebands. However, in practice this is difficult since it requires knowledge of the lineshape of the sidebands.

Probing our atoms in a 1D lattice, in the way described above, yields spectra of the type shown in Fig. 3.3(e). Naively, we would expect each sideband to exhibit the same Lorentzian lineshape as the carrier transition. In reality, for each sideband we observe an inhomogenously broadened lineshape tending towards the carrier. This feature is explained by the varying axial trap frequency along the radial dimension, which leads to a finite radial temperature and subsequent dephasing of the sideband transitions, as shown in Fig. 3.3(d). To derive an expression for this inhomogeneous lineshape, we consider an initial state $|n_x, n_y, n_z\rangle$ with associated energy [205]:

$$E(n_x, n_y, n_z) = \hbar\omega_r(n_x + n_y + 1) + \hbar\omega_z(n_z + \frac{1}{2}) + \mathcal{O}(n_z^2, n_x n_z, \dots), \tag{3.17}$$

where $\mathcal{O}(n_z^2, n_x n_z, \dots)$ subsumes higher order terms arising in the expansion of the lattice potential [205]. The transition $|n_x, n_y, n_z\rangle \rightarrow |n_x, n_y, n_z + 1\rangle$ has a frequency:

$$\omega(n_x, n_y, n_z) = \omega_z - \omega_{\text{rec}}(n_z + 1) + \omega_{\text{rec}} \frac{\omega_r}{\omega_z}(n_x + n_y + 1), \tag{3.18}$$

where $\hbar\omega_{\text{rec}} = \hbar^2 k^2/(2m)$ is the recoil frequency. Each individual transition of this type takes the form of a power broadened Lorentzian with linewidth Γ. Since our atomic sample is thermally distributed, the complete lineshape is then consituted of the thermally averaged individual Lorentzians:

$$p(\omega_L) = \frac{1}{Z} \sum_{n_r, n_z}^{\infty} e^{-E_z(n_z)/(k_B T_z)} \frac{(n_r + 1) e^{-\hbar\omega_r(n_r+1)/(k_B T_r)}}{\left(1 + \frac{4}{\Gamma^2}\left[\omega_L - \omega(n_r, n_z)\right]^2\right)}, \tag{3.19}$$

where ω_L is the laser frequency, Z is the normalizing partition function and $n_r = n_x + n_y$ is a radial quantum number. We use this expression to fit sideband spectra like those of Fig. 3.3(e) and extract the relevant physical quantites described above.

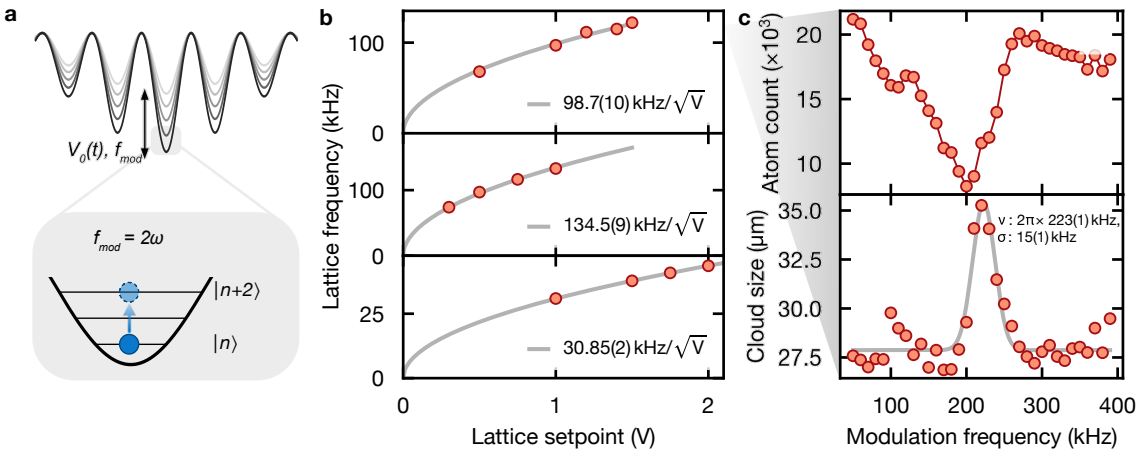

Figure 3.4 | Modulation spectroscopy and lattice calibration. (**a**) Modulation spectroscopy is performed by modulating the amplitude of the lattice V_0 using a sinusoidal signal of varying frequency f_{mod}. At a modulation frequency equivalent to twice the trap frequency, amplitude modulation leads to an excitation by two motional quanta and subsequent heating of atoms from the lattice. (**b**) We measure the lattice depth at various lattice intensity setpoints, using this method to calibrate the lattice depth in each arm. (**c**) The effect of modulation is observed both in the atom count and in the cloud size.

3.3.2 Sideband cooling

The principles described above can be used, not merely for probing atoms in a lattice, but also for cooling. By addressing the red sideband transition using our narrow clock laser, we excite atoms from the $|g, n\rangle$ to the $|e, n-1\rangle$ state. Subsequent repumping of the atoms from this state back into the ground state preserves the motional quantum number so that the final state is given by $|g, n-1\rangle$. Ideally, this cycle repeats itself until all atoms find themselves in the motional ground state.

In our experiment, we employ a pulsed cooling scheme wherein each cooling cycle consists of fourty instances of a 800 μs red sideband clock pulse followed by a 200 μs repumping pulse [Fig. 3.3(b)]. This is appended by a 40 ms period of rethermalization before the cooling cycle is repeated up to four times. The trap depth is maintained at $\approx 70E_{\text{rec}}$ throughout the sideband cooling and spectroscopy.

3.3.3 Modulation spectroscopy

An alternative method to determing the trap frequencies of our lattice relies on modulation of its amplitude V_0. As we briefly outlined in section 2.3.5, intensity modulation of the lattice laser leads to parametric heating of the atoms at a rate that is proportional to twice the modulation frequency. By scanning this frequency, we ought at some point, to reach a frequency that coincides with a lattice transition corresponding to an excitation by two motional quanta $|n\rangle \rightarrow |n+2\rangle$ [Fig. 3.4(a)]. The resulting atom loss can then be captured on a camera using absorption imaging. An example of such a modulation spectrum is shown in the top panel of Fig. 3.4(b). To capture this data we trigger a function generator to output a 30 ms sinusoidal burst at the desired frequency with a modulation depth of 0.3 V. The modulation frequency is

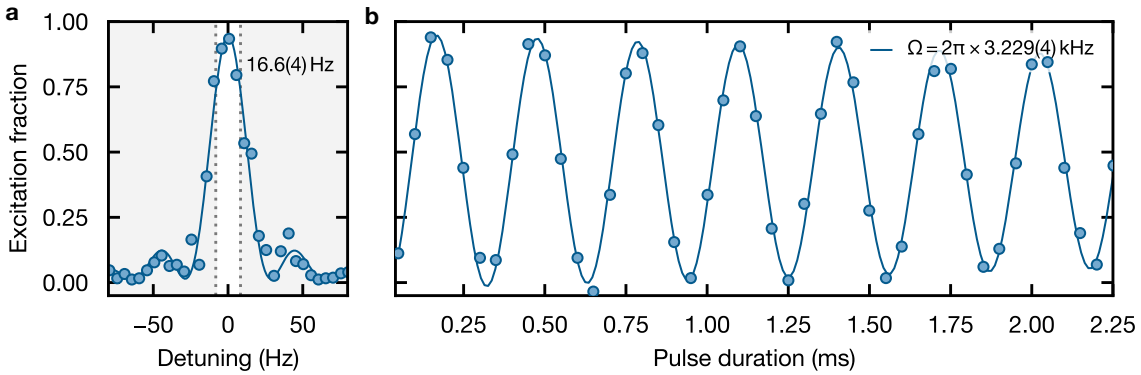

Figure 3.5 | Rabi spectroscopy. (**a**) Fourier-limited lineshape from Rabi spectroscopy performed on the clock transition in ^{174}Yb. The solid line is a fit of the data according to Eq. (3.20) (**b**) Rabi oscillations („flops“) observed on the same transition for variable probe pulse durations. By adjusting the clock laser pointing along the co-aligned magic lattice, we maximize the Rabi frequency and extract the corresponding π-pulse duration using an exponentially decaying sinusoid fit of the data (solid line).

sufficiently fast ($\sim 100\,$kHz) compared to the intensity servo bandwidth ($< 10\,$kHz) to prevent unwanted signal distortion.

In addition to the atomic loss signal, we can observe the cloud size as a function of the modulation frequency. This allows us to capture spectra like those shown in the lower panel of Fig. 3.4(c), from which we extract the trap frequency from the maximum of a Gaussian. Using these spectra, we calibrate our lattice depths along each dimension [Fig. 3.4(b)].

3.3.4 Rabi spectroscopy

The combination of optical lattices and a narrow linewidth clock laser allows us to perform high-resolution spectroscopy on the clock transition of ytterbium. We coherently drive our atoms on the clock transition using a light pulse of duration $\tau = \pi/\Omega$, where Ω is the Rabi frequency of the transition on resonance. As a function of laser detuning $\delta = \omega_L - \omega_0$ (with ω_L the laser frequency and ω_0 the frequency of the atomic transition), the probability of finding the atom in the excited state is given by

$$P_e(\delta) = \frac{\pi^2}{4}\mathrm{sinc}^2\left(\frac{\pi}{2}\frac{\widetilde{\Omega}}{\Omega}\right), \tag{3.20}$$

where $\widetilde{\Omega} = \sqrt{\Omega^2 + \delta^2}$ is the generalized Rabi frequency. We measure this probability by observing the excited state fraction of our atoms using the state-selective imaging techniques described previously in Section 3.1.4. An example of the type of excitation spectra captured using this method are shown in Fig. 3.5(a). The additional side peaks visible in this spectrum stem from higher order Fourier components of our square pulse shape used to excite the atoms. To minimize radial sideband excitations and Rabi frequency inhomogeneities, we align our clock laser to be co-aligned with the lattice axis along which we interrogate the atoms [183]. For bosonic isotopes of ytterbium, the coupling between ground and excited clock state vanishes at zero magnetic field, due to the absence of a nuclear spin degree of freedom. To induce this

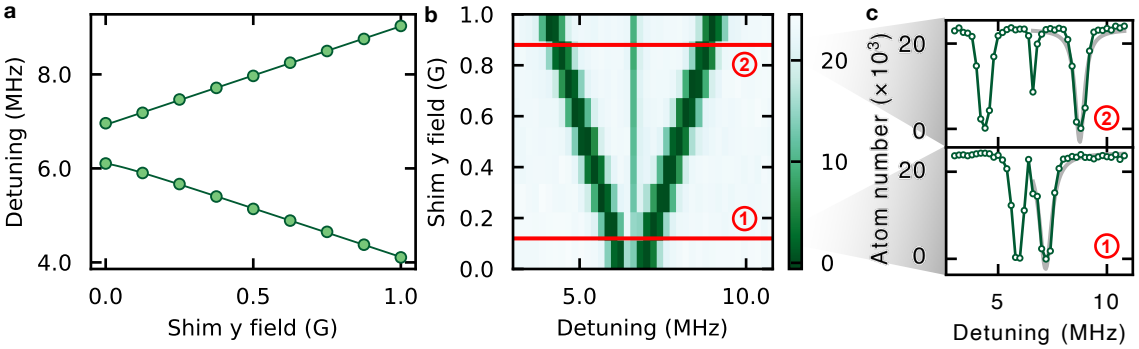

Figure 3.6 | Shim coil calibration. (**a**) Resonance position for the two magnetically sensitive $m_J = \pm 1$ sublevels of $^3P_1$ as a function of the applied coil current. The data is fitted using the linear relationship expressed in Eq. (3.21). (**b**) The same data as in (a), this time including the relevant atom number measured using absorption imaging. The two red lines indicate a cut through the data which is visualized in subfigure (c). (**c**) Two datasets used to generate the data shown in (a) and (b), taken at 0.1 G (lower panel) and 0.9 G (upper panel). The resonance position is measured using a Gaussian fit (grey).

transiton, it is therefore necessary to admix a small fraction of the $^3P_1$ state to the $^3P_0$ state via an applied external magnetic field [206, 207] (see also 1.1.2). By reducing the intensity of our probe pulse as well as the strength of our applied magnetic field, we can reduce the linewidth of our Rabi lineshape in a controlled manner to probe the transition with a greater degree of precision. To optimize the Rabi frequency and determine the π-pulse time, we adjust the pointing of our clock laser beam along the lattice axis and observe the induced Rabi oscillations as a function of the probe pulse duration [Fig. 3.5(b)].

Many of the previously discussed methods rely on accurate knowledge of the magnetic field being applied to the atoms. In the following section we discuss the corresponding measurements performed to calibrate our magnetic fields.

3.4 Magnetic field calibration

To calibrate our magnetic fields, we want to know what coil current value corresponds to what magnetic field in the experiment. To deduce this we make use of the previously described spectroscopic methods to measure the linear and quadratic Zeeman shift of notable atomic transitions. The linear Zeeman shift arises as a consequence of the interaction between the applied external magnetic field B, and the the magnetic dipole moment of the atom μ_B, taking the form [125]:

$$\Delta E_{\text{lin}} = \alpha_m B = \mu_B g_J \Delta m_J B, \tag{3.21}$$

where g_J is the Landé g-factor of the relevant transition and Δm_J is the corresponding change in the z component of the total angular momentum. The linear Zeeman shift has previously been measured as a function of the applied magnetic field for the broad $^1S_0 \rightarrow ^1P_1$ transition as well as the for narrower $^1S_0 \rightarrow ^3P_1$ transition [208]. In the case of the clock transition, where $J = 0$ for both states, this effect vanishes. However, a small quadratic dependency on

the magnetic field is retained due to the magnetic-field induced coupling of fine-structure levels within the triplet manifold [209]:

$$\Delta E_{\text{quad}} = \beta_m B^2, \tag{3.22}$$

where β_m is a proportionality constant dependent on the frequency of the fine structure levels.

3.4.1 Measurements

To characterize the linear Zeeman shift of our coils, we perform spectroscopy on the magnetically sensitive $^1S_0 \rightarrow {}^3P_1$ transition. Here, we employ our 3D MOT arm 4 (oriented along the z-axis) to track the resonance positions of the m_J states over a range of magnetic fields [shown for the example of the y-shim coils in Fig. 3.6(a)]. At each value of the magnetic field, we scan the detuning of the MOT arm and observe the ground state atom number using absorption spectroscopy [Figs. 3.6(b) and 3.6(c)]. We assume the magnetic field of any given uncalibrated coil pair to take the form:

$$B(I) = \sqrt{\left(\frac{a}{\alpha_m} I - B_{\parallel}\right)^2 + B_{\perp}^2}, \tag{3.23}$$

where I is the applied current, producing a field aI/α_m. Here a, with units of Hz/A, is an unknown factor which we wish to determine. Toghether with the known value of the linear Zeeman shift α_m, this gives the required calibration factor in G/A. Additional magnetic fields from other uncalibrated coils is split into components parallel $(B_{\parallel})$ and perpendicular $(B_{\perp})$ to the coil axis being calibrated. We use Eq. (3.23) to fit data of the type obtained in Fig. 3.6(a). For our main coils, this results in a calibration factor of 7.41(8) G/A, which is in good agreement with the expected value calculated in Section 2.2.2. During our measurements, we find that the optical lattice used to initially confine the atoms causes an additional non-linear shift in the resonance positions as a function of the magnetic field, likely due to a non-vanishing tensor contribution to the polarizability. To prevent this, we turn off the lattice while the green spectroscopy is performed.

Since our main MOT coils are able to generate large fields of up to 400 G, we additionally measure the quadratic Zeeman shift to confirm our calibration. For measuring the quadratic shift, we perform Rabi spectroscopy at multiple different magnetic field values and track the position of the clock resonance [Fig. 3.7(a)]. This yields a value of 58.4(12) mHz/G^2, close to the 61.2(1) mHz/G^2 measured in Ref. [174]. At higher magnetic fields admixing of the $^3P_1$ state causes a broadening of the transition linewidth, thereby introducting uncertainty into the measurement. We observe deviations in the expected behavior for fields above 350 G, which are likely technical in nature.

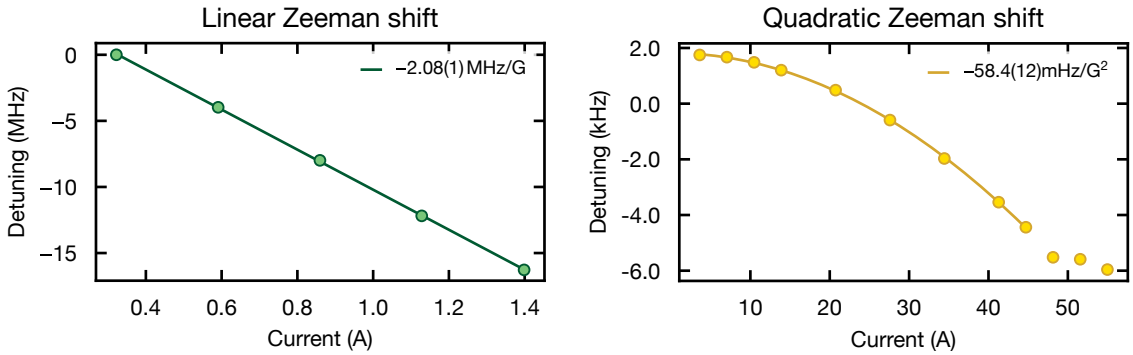

Figure 3.7 | Main MOT coil calibration. (**a**) Linear Zeeman shift measured for our main MOT coil pair using atom loss spectroscopy on the $^1S_0 \rightarrow {}^3P_1$ transition for the $m_J = -1$ state. After calibration, a linear fit of the data yields a value of $-2.08(1)$ MHz/ G, close to the literature value of $\alpha_m = 2.08943(7)$ MHz/ G [208]. (**b**) Quadratic Zeeman shift measured using Rabi spectroscopy on the clock transition. Using the measured shift, we calibrate our magnetic field to scale with current at a rate of 7.41(8) G/ A.

3.5 Tweezer arrays

Tweezer arrays will form an integral part of our experimental platform, allowing us to dynamically re-arrange atoms in our optical lattice or implant them therein in a controlled fashion [210]. Furthermore, our planned simulations of lattice gauge theories necessitate two separate tweezer arrays, operating at the tune-out wavelengths for the ground and excited state of the clock transition (see Section 5.3.1 for details). To test the loading and cooling of individual Yb atoms in optical tweezers, we initially work with an array of 532 nm tweezers. This wavelengths is readily available from commercial laser sources and has been shown to work well in tweezer arrays of Yb atoms [66]. In the following we describe the realization of such an array in our experiment.

3.5.1 Initial alignment

Initial alignment of the tweezer array onto the atoms was performed using a single large tweezer. For this purpose the 1:10 telescope was removed and the NA artifically restricted using an iris (see Fig. 2.18 for reference). We then performed the standard MOT loading sequence with compression, while keeping the tweezer light on throughout. A first signal was observed using TOF imaging after 50 ms time-of-flight. We then repositioned the compressed MOT using our shim coils to optimize this signal. To increase the signal fidelity, we switched to fluoresence imaging. A clear signal was obtained for longer imaging pulse lengths (100 ms) and a deep tweezer ($\approx$ 210 mW). We further improved the SNR of the initial signal by tuning the position of the final $f = 500$ mm imaging lens infront of the OrcaQuest using a micrometer stage (from subsequent fits of the tweezers, we calculated a magnification of $\times 20.2$ in our imaging system). We then began to generate arrays of various sizes (number of tweezers and power per tweezer) to explore and calibrate the set of optimal tweezer parameters in each array configuration. An example of such an array is shown in Fig. 3.8(a). Previous imaging of the tweezer setup outside the experiment, during pre-alignment, determined a tweezer spacing of 2.05 µm/ MHz [189].

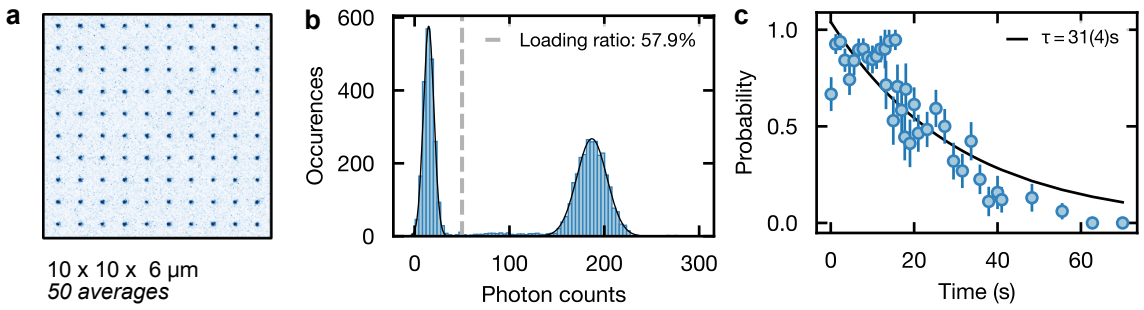

Figure 3.8 | Tweezer Arrays. (**a**) An image of a $10 \times 10 \times 6$ µm tweezer array at 532 nm composed of fifty averages. (**b**) Histogram of photon count occurences. The isolated peak centered around ≈ 180 counts and well-separated from the background peak is evidence of single atoms in individual tweezers. The loading ratio is determined by the ratio of total occurences above a cut-off value (grey dashed line) to those below. (**c**) The lifetime of atoms in tweezers as determined by measuring the probability of finding an atom in a tweezer after a certain time interval. An exponential fit of the data yields a decay constant of $\tau = 31(4)$s.

3.5.2 Cooling and trapping of individual atoms

Our tweezers are initially loaded stochastically, leaving certain tweezers empty while other are filled with atoms. In the latter case, occupied tweezers are likely to be loaded with more than one atom per tweezer. To obtain unity filling, some form of photoassociation (PA) light is required whereby two atoms are excited to an energetically higher-lying molecular state and leave the tweezer trap [211]. In this way a parity projection is performed so that either one or zero atoms remain in the tweezer depending on the initial tweezer occupancy. To detect the remaining individual atoms residing in tweezers after PA, we require each atom to scatter sufficient imaging light to be detectable on our camera. Since this heats the atoms in the tweezer array, additional cooling of atoms is required during imaging. In our experiment, we have found that PA and cooling can be combined into a single operation.

For this purpose we employ our top MOT beam, detuned by 2.65 MHz from the $^1S_0 \rightarrow {}^3P_1$ free space resonance. We find that ≈ 9 mW per tweezer are optimal in terms of SNR when combined with our PA/cooling light. Assuming a perfectly diffraction-limited spot size of $d = 464$ nm, this corresponds to a trap depth of ≈ 32 MHz and harmonic confinement frequency of $\omega_r \approx 2\pi \times 2.3$ MHz. The value of the ground state polarizability used to estimate these quantities is taken from our empirical polarizability model of Section 4.4.

After cooling, we perform absorption imaging on the $^1S_0 \rightarrow {}^1P_1$ resonance with a 50 ms long, 15 µW imaging pulse. The OrcaQuest exposure time is set to 60 ms. Recording the photon count occurences during imaging as a histogram we verify single-occupancy in our tweezers by observing clearly separated zero-atom and single-atom peaks [Fig. 3.8(b)]. We performed several lifetime measurements on atoms trapped in our tweezer array by imaging the array after various hold times. In theory, the atoms should follow a simple single-body decay exponential, with a lifetime limited by off-resonant photon scattering from the tweezers. With the array parameters described above, this yields a tweezer lifetime of $\tau = 31(4)$s [Fig. 3.8(c)].

CHAPTER 4

State-dependent potentials in neutral ytterbium atoms

As the neutral atom toolbox has expanded, so too has the role of state-dependent potentials. These have been used, at varying times, to implement new cooling and state preparation schemes [76–78], simulate out-of-equilibrium dynamics [80, 82, 83] and investigate strongly coupled quantum emitters [84]. State-dependent potentials have also been a significant driving force in the realization of neutral atom quantum computing protocols [51, 85–88, 153, 212].

Many of these applications have relied on alkali atoms such as Rb and Cs, where the interplay between the D1 and D2 lines gives rise to state-dependent potentials located at convenient laser wavelengths [142]. For example, in ^{87}Rb, the tune-out condition for the $\left|^2\mathrm{S}_{1/2}, F = 2\right\rangle$ state is achieved for a laser wavelength of $\lambda \approx 790\,\mathrm{nm}$, that exactly balances the contribution of the D1 and D2 transitions [148]. By varying the laser detuning with respect to either transition, the polarizability of the desired state can be carefully controlled. However, the wavelength splitting between the fine-structure states $^2\mathrm{P}_{1/2}$ and $^2\mathrm{P}_{3/2}$ is only on the order of some 15 nm. Thus, implementing state-dependent potentials in alkali atoms often relies on using near-resonant laser light, which induces heating and limits the lifetime of the desired state. AELs do not suffer this drawback. State-dependent control of the metastable electronic states is possible even with light far detuned from any atomic resonance. This makes state-dependent potentials in AELs ideal for investigating a wide variety of topics from impurity physics [213] to transport dynamics [214] and quantum computing [51, 91, 153].

In this chapter, we describe our measurements of three new state-dependent wavelengths for the $^1\mathrm{S}_0$ ground state and $^3\mathrm{P}_0$ metastable excited state in neutral ytterbium. We begin by examining two magic wavelength measurements, performed using a Rabi spectroscopy-based scheme. Subsequently, we employ parametric heating in an optical lattice to determine the ground state tune-out wavelength. To conclude this chapter, we touch on some recent progess towards a measurement of the excited state tune-out wavelength as well as the application of these state-dependent potentials in the future. The results in this chapter are based, in large part, on Ref. [93].

4.1 Measuring magic wavelengths

As we discussed in Chapter 1, a wavelength at which the differential polarizability between two states vanishes is known as a magic wavelength. For the states of the ytterbium clock transition, multiple such wavelengths exist within a range readily accessible to lasers commonly used in ultracold atom experiments (see Figs 1.2 and 4.4(b)). In our publication, we measure two new magic wavelengths for the $^1S_0$ and $^3P_0$ states in ^{174}Yb, located at $\nu_{m1} = 542.50205(19)$ THz and $\nu_{m2} = 652.281(21)$ THz.

4.1.1 Measurement principle

To measure the magic wavelengths mentioned above, we rely on the previously described technique of Rabi spectroscopy (Section 3.3.4). We use this technique to measure the wavelength-dependent light shift induced on the clock transition by an optical potential (dipole beam) [135]. This light shift is measured for a number of different dipole beam frequencies around the expected value of the magic wavelength. From these values it is possible to determine the frequency at which the light shift is zero.

We prepare our system by directly loading $\approx 300 \times 10^3$ atoms from our compressed MOT into a 1D, $\approx 730 E_{rec}$ deep optical lattice operating at the magic wavelength of $\lambda_{lat} = 759.3$ nm. Using sideband spectroscopy, we determine the axial temperature of our atoms in the lattice to be $\approx 12\,\mu$K. To generate the additional optical potential, we superimpose a frequency-tunable laser beam with the optical lattice at an angle of $\approx 1°$. We choose this finite angle to avoid unwanted back-reflections of the dipole beam light from the lattice mirror [Fig. 4.1(a)]. In the case of the measurement near 652 THz, this light is provided by an optical parametric oscillator (OPO)[1]. This laser has the advantage of an almost continously tunable output frequency across a large part of the visible spectrum, but only a small amount of available power (tens of mW). This in turn has consequences for the systematic error on our measurement (see Section 4.1.2 for details). By contrast, the measurement performed at 542 THz uses a VECSEL laser[2] with a high output power but relatively modest frequency tuning range when compared to the OPO (see Section 2.3.6 for more details). Rabi spectroscopy is performed under the influence of a ≈ 100 G external magnetic field applied along the vertical z-axis using our main MOT coils. The resulting excitation fraction is determined using the state-selective absorption imaging described in Section 3.1.4. To measure the induced AC stark shift at a given wavelength, we perform spectroscopy with and without the addition of the dipole beam on the atoms for various dipole beam powers [Fig. 4.1(a) and 4.1(b)]. The linear relationship between these two quantities allows us to extract a value for the differential light shift at a particular wavelength. Repeating this measurement at various wavelengths around the expected position of the magic wavelength [Fig. 4.1(c)] allows us to extract the point where the differential light shift is vanishing using a simple least-squares linear fit of the data [Fig. 4.1(d)]. In this way we obtain the aforementioned values of $\nu_{m1} = 542.50205(19)$ THz and $\nu_{m2} = 652.281(21)$ THz. The ν_{m2} value was independently confirmed using Ramsey spectroscopy by the authors of Ref. [139].

[1] HÜBNER Photonics C-WAVE VIS+IR Low Power
[2] Vexlum VALO-SHG-SF

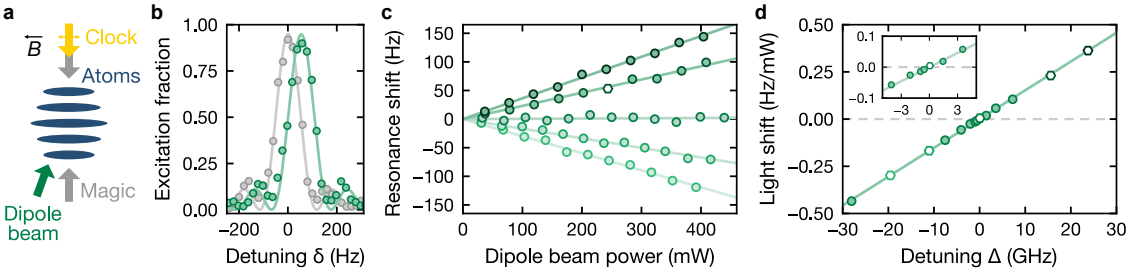

Figure 4.1 | Magic wavelength measurement. (**a**) Schematic of the experimental setup. Atoms are loaded from the MOT into a 1D magic wavelength lattice (blue). An additional dipole beam is superimposed on the atoms (green) at an angle of $\approx 1°$. We interrogate the atoms using Rabi spectroscopy with and without the dipole beam using our narrow clock laser with a polarization (double arrow) parallel to the applied external magnetic field (B). (**b**) Resonance spectra measured with (green) and without (grey) the dipole trap. Data shown here is for the measurement of ν_{m1}. The fitted Rabi lineshapes allows us to extract the difference in the resonance position for a given dipole beam power. (**c**) Resonance shifts for as a function of the applied dipole beam power for different wavelengths. The results from (b) are indicated by a white hexagon and each data point is an average of three Rabi spectroscopy measurements. The slope of each dataset provides a value for the light shift at that wavelength (**d**) Measured light shifts as a function of the detuning from the magic frequency $\Delta = \omega_L - \omega_m$. Data from (c) is shown as empty heaxgons. Figure is taken from Ref. [93].

4.1.2 Error analysis

Differentiating between statistical and systematic errors, our measurement values may be written as:

$$\nu_{\mathrm{m1}} = \left[542502.05 \pm 0.08_{\mathrm{stat}} \left(^{+0.01}_{-0.11}\right)_{\mathrm{sys}}\right] \mathrm{GHz} \tag{4.1}$$

$$\nu_{\mathrm{m2}} = \left[652281 \pm 10_{\mathrm{stat}} \left(^{+11}_{-0}\right)_{\mathrm{sys}}\right] \mathrm{GHz}. \tag{4.2}$$

The systematic component of the measurement error comprises several different effects, which are analyzed in the following.

Drift errors.—To mitigate the effect of slow drifts in the frequency of our clock laser over the course of a measurement, we randomize the detuning $\delta = \omega_L - \omega_0$ of the clock laser for each new run of the experiment. In addition to a frequency drift of the clock laser, we also observe a drift in the relative position between the optical lattice and the dipole beam. By keeping track of the overlap using a camera, we estimate the effect of this drift to account for no more than a 7% reduction in intensity at the location of the atoms. From the camera data, we observe the drift to be roughly linear in time. To ascertain the corresponding effect on the light shift, we first calculate the atom cloud size in the lattice to be $\sigma_z = 288(18)\,\mu\mathrm{m}, \sigma_r = 16.52(4)\,\mu\mathrm{m}$ by fitting a 3D Gaussian to a set of representative atom cloud images. The weighted mean of the intensity experienced by an atom at a given location is then obtained by integrating the cloud over the dipole beam intensity distribution. In this way we estimate a -0.11 GHz and 0.3 GHz contribution to the systematic error of the ν_{m1} and ν_{m2} measurement respectively.

Calibration errors.—Prior to the start of each measurement, we determine the intensity of our dipole trap beam using a photodetector equipped with a bandpass filter. We observe a wavelength dependent sinusoidal modulation of the otherwise linear light shift data which we

believe to stem from étaloning between the filter and the photodiode facet. To calibrate out this effect, we separately measure the intensity of our dipole trap using an integrating sphere[3]. We discover the modulation to have a periodicity of 9.34(6) GHz with a relative amplitude difference of ≈ 20%. The fitted sinusoid is used to rescale the light shift data accordingly. The corrected dataset is shown in Fig. 4.1(d).

Scaling errors.—The lower output power of the OPO laser used in the measurement of ν_{m2} as well as the reduced gradient of the polarizability curve around this frequency result in a larger statistical uncertainty. To cope with this unfortunate reality, we increase the range of detunings around the magic wavelength within which we perform our measurements. However, given large enough detunings, the assumption of a linear light shift begins to break down. To quantify the contribution of this effect on the systematic error of ν_{m2}, the theoretical values of the polarizability for each detuning sampled in the experiment is calculated and then compared to the value determined from the linear fit. In this way we determine the discrepancy between the theoretically expected zero-crossing wavelength and the one determined in the experiment. Within a range of ±1 THz, this discrepancy amounts to a systematic error of 11 GHz, significantly larger than any of the other systematic error sources described above. We thus use this range to bound the detunings for which we perform our data analysis.

4.2 Measuring the ground state tune-out wavelength

In addition to the two magic wavelengths measured in the previous section, we also perform the first measurement of the $^1S_0$ tune-out wavelength in ^{174}Yb. For this purpose we measure the lifetime of a thermal sample of atoms in a magic optical lattice when exposed to amplitude modulation by an additional shallow tune-out lattice potential [91]. The lifetime is measured at various lattice wavelengths around the predicted tune-out wavelength and compared to the lifetime with no modulation. The tune-out wavelengths is determined from the minimum of this dataset. We determine value of $\nu_{to} = 541.8325(5)$ THz for the ground state tune-out frequency.

4.2.1 Measurement principle

Similarly to the magic wavelength measurement, atoms are once again loaded into a 1D magic lattice at 759.3 nm. Here, we initially load at a lattice depth of ≈ $390E_{rec}$ before ramping to ≈ $730E_{rec}$ within 10 ms. Instead of an additional dipole beam, we now superimpose a shallow variable-wavelength perturbing lattice with our magic lattice [Fig. 4.2(a)], which we turn on within 5 ms after having ramped our magic lattice to the aforementioned ≈ $730E_{rec}$. This second shallow lattice is co-propagating with the magic lattice and its wavelength is tuned around the expected position of the ground state tune-out wavelength. At each new wavelength value, we modulate the amplitude of this lattice to induce parametric heating and measure the resulting atom loss rate from the trap (in analogy to the measurements performed in Ref. [91]). This is compared to the atom loss rate in the unmodulated case to determine the differential loss rate $\Gamma_{exc} := 1/\tau - 1/\tau_0$. Here τ and τ_0 are the lifetimes in the modulated

[3]Thorlabs S140C

and unmodulated lattice respectively, as determined by an simple exponential fit of the atom count data over the hold time [Fig. 4.2(d)] If the shallow lattice is running at the tune-out wavelength, the scalar polarizability for the ground state vanishes and the shallow lattice has no effect on the ground state. Therefore, at the tune-out wavelength, we expect a vanishing differential atom loss rate [Fig. 4.2(c)].

Modulation spectroscopy.—To determine the parametric heating resonance, we perform modulation spectroscopy in our combined lattice system (see Section 3.3.3). To this end, both lattices are turned on and the amplitude of the shallow lattice is modulated over a range of frequencies ν_{mod} using a square-wave with a modulation depth of 100% [Fig. 4.2(b)]. In practice, this is executed by a function generator programmed to periodically turn on and off the relevant AOM. We note that the intensity stabilization of the shallow lattice reliant on this AOM is unaffected by the modulation which occurs on timescales several orders of magnitude smaller than those corresponding to the servo bandwidth. Due to the incommensurability of the lattices, two types of modulation are possible on any given lattice site. On the one hand we have fluctuations in the trap frequency responsible for excitations separated by two motional quanta and resulting in parametric heating. On the other hand, we also encounter fluctuations in the position of the trap center, leading to exciations by only one motional quantum. Both of these processes are visible as broad dips in the measured modulation spectrum centered at $\nu_{\mathrm{mod}} \approx 89\,\mathrm{kHz}$ and $\nu_{\mathrm{mod}} \approx 178\,\mathrm{kHz}$ respectively. Due to the square-wave modulation, we also observe smaller dips at lower frequency components which originate in the Fourier components of the pulse. We use sideband spectroscopy to separately measure lattice trap frequency. This yields a value close to $\nu_z \approx 107\,\mathrm{kHz}$. We speculate this discrepancy to originate in the anharmonicity of higher motional states in the lattice. For the purposes of our tune-out wavelength measurement we maintain the modulation frequency at $\nu_{\mathrm{mod}} \approx 178\,\mathrm{kHz}$.

4.2.2 Data analysis

Fit functions.—Given our lattice parameters, we estimate our atomic sample to be dilute enough for two and three-body losses to be of negligible concern. We thus expect a single exponential fit of our lifetime data to be sufficient to capture the necessary decay dynamics. We confirm this hypothesis by comparing the lifetime extracted from a single exponential fit of our datasets with that of two and three-body super-exponential fits. As expected, the lifetime is found to be unaffected (within error bars) by the higher order exponential fits.

Given our choice of modulation frequency, it is reasonable to assume that parametric heating is the dominant mechanism responsible for atom loss from the lattice. Under this assumption, the excess loss rate scales with the square of the intensity in a fashion already briefly discussed in Section 2.3.5 [178, 215]:

$$\Gamma_{\mathrm{exc}} = \pi^2 \nu_{\mathrm{mod}}^2 S_\epsilon(2\nu_{\mathrm{mod}}) \propto \alpha^2(\Delta)\nu_{\mathrm{mod}}^2 I^2, \tag{4.3}$$

where $\alpha(\Delta)$ is the detuning-dependent polarizability of the ground state. For sufficiently small detunings around tune-out wavelength the polarizability is linearly proportional to the detuning. As such, the excess loss rate also scales quadratically with the detuning in

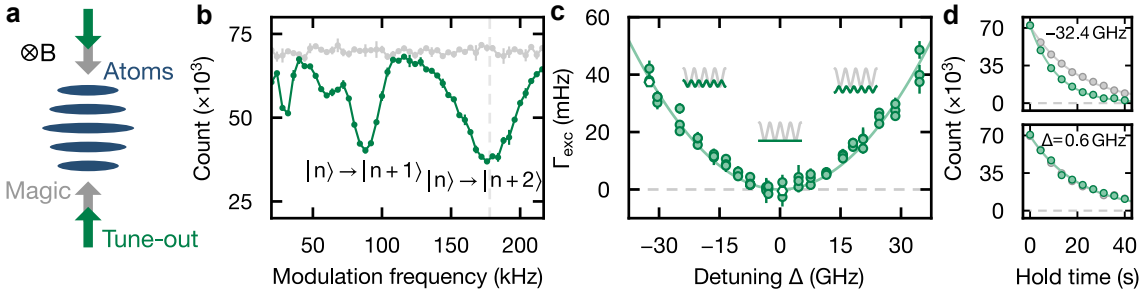

Figure 4.2 | Ground state tune-out wavelength measurement. (**a**) Schematic of the experimental setup. Atoms (blue) are loaded into a 1D magic optical lattice (grey) onto which we superimpose a shallow variable-wavelength tune-out lattice (green). (**b**) The modulation spectroscopy data with (green) and without (grey) modulating the amplitude of the tune-out lattice. The incommensurability of the two lattices leads us to observe two prominent dips in the atom count at 89 kHz and 178 kHz corresponding to excitations by one and two motional quanta respectively. For the tune-out wavelength measurement, we make use of the latter frequency. The plotted data is taken at a detuning of $\Delta = 327$ GHz removed from the tune-out wavelength for 40×10^3 modulation cycles and averaged over two measurements. (**c**) The excess loss rate determined from lifetime measurements at various detunings around the tune-out wavelength. At the tune-out wavelength, the shallow lattice is invisible to the ground state atoms and the excess loss rate vanishes (see main text for more details). (**d**) Three examples of the lifetime measurements taken at each wavelength value. Green data is with shallow lattice modulation and grey data without. The data extracted from the three panels is indicated by white hexagons in (c). Figure is adpated from Ref. [93].

this range. It is this reasoning that leads us to fit the excess atom loss rate data presented in [Fig. 4.2(c)] using a quadratic function. Errors arising from deviations in this quadratic model are discussed in the following section.

4.2.3 Error analysis

As before, we divide our errors into those of a statistical and those of a systematic nature:

$$\nu_{\text{to}} = \left[541832.49 \pm 0.23_{\text{stat}} \left(^{+0.05}_{-0.24}\right)_{\text{sys}}\right] \text{GHz}, \tag{4.4}$$

and analyze the systematic component in the following.

Deviation from quadratic model.—To probe the error arising from deviations of the quadratic fit model of our excess atom loss rate data at large detunings, we pursue a number of different strategies.

Firstly, we find that by fitting an additional offset in the y-axis, the fit quality at large detunings is improved. However, this leads to an unphysical offset in the excess atom loss rate at the tune-out frequency ν_{to}. By fitting a series of increasingly truncated datasets, we discover this offset to become significant only at detunings exceeding $|\Delta| \gtrsim 21$ GHz [Fig. 4.3(a)]. To gain further insight, we detune our tune-out lattice by 25 GHz and measure the excess loss rate dependency on the tune-out lattice intensity. Above lattice powers of ≈ 100 mW, we begin to observe a deviation from the expected quadratic behavior and instead find that introducing an additional quartic correction to the intensity is necessary to describe the data accurately [Fig. 4.3(b)]. In particular, the quartic model describes the saturation of the excess atom

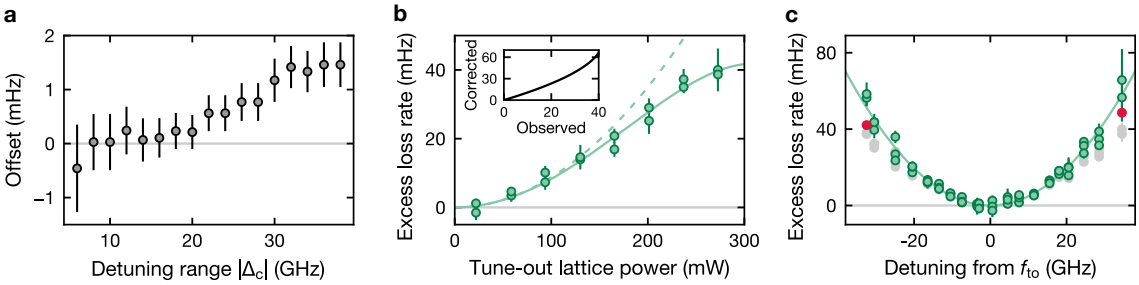

Figure 4.3 | **Analysis of systematic errors.** (**a**) Offset in the excess loss rate determined from quadratic fits of truncated data sets of the excess loss rate. The detuning range indicated on the *x*-axis refers to the range of detunings over which a given dataset has been truncated to determine the offset. We observe a significant deviation from zero only for datasets including detunings larger than 21 GHz. (**b**) For detunings beyond this range, we observe significant deviations from our quadratic fit model (dashed green), as is the case here for a detuning of 25 GHz. Above tune-out lattice powers of $\approx$ 100 mW, the excess loss rate data is better described by a quartic fit (solid green). The inset shows the rescaling factor calulated using the quartic correction and used to rescale the data. (**c**) Rescaled (green) vs. original (grey) excess loss rate data. The two points in red are rejected since they feature loss rates in excess of 40 mHz (see main text for more information). Figure is taken from Ref. [93].

loss rate at 40 mHz for large tune-out lattice intensities. We speculate this correction to be a consequence of the anharmonicity of the lattice potential [216] and use it to rescale the excess atom loss rate data for the purposes of error analysis, as shown in [Fig. 4.3(c)]. For the two datapoints which exhibit an excess loss rate above 40 mHz no calibration data excists and as such, these are rejected from the analysis. A renewed comparison of the quadratic fit of this rescaled data with and without offset yields a frequency difference of 53 MHz in the value of ν_{to}, which we interpret as a contribution to the systematic error of this measurement.

Secondly, we return to the truncated non-rescaled datasets and observe the difference in the fitted value of the tune-out frequency in each trunctation $\widetilde{\nu}_{\mathrm{to}}$, with that of the full dataset ν_{to}. For datasets with detunings exceeding $|\Delta| \gtrsim 11.5\,\mathrm{GHz}$, we find only a small variance from ν_{to}. Since we concluded that for detunings above $|\Delta| \approx 21\,\mathrm{GHz}$, the previously discussed offset becomes significant, we further restrict our region of interest to lie below this value. Within this range $11.5\,\mathrm{GHz} \lesssim |\Delta| \lesssim 21\,\mathrm{GHz}$, the largest single deviation from ν_{to} is found to be $\Delta\nu_{\mathrm{to}} = -243\,\mathrm{MHz}$. We posit this value as the dominant contribution to the systematic error of our tune-our measurement.

4.3 Excited state polarizability

We can make use of our new-found knowledge of the tune-out wavelength to measure the excited state polarizability at ν_{to}. For this, we use an identical setup to the one described in Section 4.1.1 and tune the dipole beam wavelength to the newly measured tune-out wavelength. The induced AC Stark shift on the transition is now completely determined by the excited state polarizability. Thus, by measuring the former, we are rewarded with the latter. To avoid power broadening of the lineshape, we operate the dipole beam at a modest 35 mW and calculate resulting intensity at the location of the atoms in the same fashion as was done

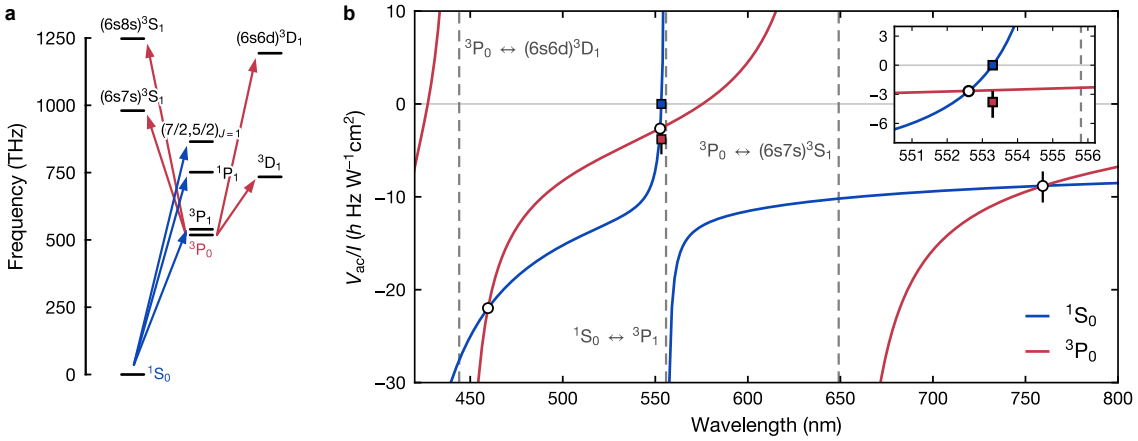

Figure 4.4 | Empirical polarizability model. (**a**) Schematic representation of the various transitions used to calculate the ground (blue) and excited (red) state polarizabilities. (**b**) A plot of the calculated polarizabilities as a function of the wavelength, together with the data points measured in Refs. [93] and [135]. The models for both states are empirically corroborated by ensuring that the fit passes through the measured magic (white circles) and ground-state tune-out (blue square) wavelengths. Inset: measured excited state polarizability (red square) at the ground state tune-out wavelength, ν_{to} (blue square). The magic wavelength ν_{m1} is indicated by the white circle. Figure is taken from Ref. [93].

for the magic wavelength measurement. Dividing the light shift V_{ac} by this value allows us to determine the polarizability to be:

$$V_{\mathrm{ac}}/I = \left[-3.8 \pm 0.07_{\mathrm{stat}} \left(^{+1.1}_{-1.6}\right)_{\mathrm{sys}}\right] \mathrm{Hz}/\frac{\mathrm{W}}{\mathrm{cm}^2}. \tag{4.5}$$

Uncertainties relating to the beam waist, atom cloud size and relative angle between dipole beam and lattice are calculated to contribute $0.85\,\mathrm{Hz}/\frac{\mathrm{W}}{\mathrm{cm}^2}$ to the systematic error of this measurement. In addition, we attribute some systematic error to the imperfect overlap of dipole beam and lattice foci. For the most part, this overlap uncertainty is expected to be contained to the axial direction, since the radial overlap is optimized prior to the measurement by maximizing the light shift on the atoms. Having previously mapped out the beam profile of both the lattice and the dipole beam, we estimate a maximum axial focus mismatch of 5 mm, corresponding to a systematic error contribution of $-0.48\,\mathrm{Hz}/\frac{\mathrm{W}}{\mathrm{cm}^2}$. Furthermore, we consider the uncertainty inherent in the calibration of our reference photodetector used for measuring the dipole beam power. The photodetector values are compared to that of an integrating sphere for various different powers and the fit uncertainty is used as an estimate for the calibration uncertainty. Finally, we measure the transmission of the dipole beam through the glass cell. The combined systematic error from these last two sources of uncertainty are estimated to be $0.24\,\mathrm{Hz}/\frac{\mathrm{W}}{\mathrm{cm}^2}$.

4.4 Empirical polarizability model

Our measurements of the state-dependent wavelengths described above allow us to refine the polarizability model discussed in Section 1.2.1. We recall that for bosonic ytterbium the absence of a nuclear spin ensures that the polarizability of a state $|i\rangle$ reduces to its scalar component:

$$\alpha_i^{(s)}(J;\omega) = \sum_{J' \neq J} \frac{2}{3} \frac{\omega_{JJ'}}{\hbar(\omega_{JJ'}^2 - \omega^2)} \left|\langle J||\boldsymbol{d}||J'\rangle\right|^2, \tag{4.6}$$

To relate the transition dipole matrix elements $\left|\langle J||\boldsymbol{d}||J'\rangle\right|$ to other physically meaningful quantities, we note its relation to a corresponding observable linewidth $\Gamma_{JJ'}$ according to [125]:

$$\Gamma_{JJ'} = \frac{\omega_{JJ'}^3}{3\pi\epsilon_0\hbar c^3} \frac{2J+1}{2J'+1} \left|\langle J||\boldsymbol{d}||J'\rangle\right|^2 \tag{4.7}$$

We can further express this linewidth in terms of the branching ratio $\beta(J,J')$ of a final state and its lifetime $\tau(J')$ in the following way:

$$\Gamma_{JJ'} = \beta(J,J')/\tau(J'), \tag{4.8}$$

so that even in the event where the linewidth is unkown, we have recourse to these two quantities.

We use these relations to determine the contribution of various transitions to the $^1S_0$ and $^3P_0$ polarizabilities within a range of visible wavelengths, subject to the constraint that our model must take account of the state-dependent wavelength values measured above. As was briefly alluded to in Section 1.2.1, the ground state polarizability is chiefly affected by the broad blue transition to the $^1P_1$ state, the green intercombination transition to $^3P_1$ and a core-excited state transition to $(7/2, 5/2)_{J=1}$ at 347 nm [104]. This notation is used in place of the usual Russell-Saunders notation scheme to indicate that we are dealing with strong spin-orbit coupling (jj-coupling) [217, 218]. Other higher-lying transitions are sufficiently far detuned for their impact on the polarizability to be negligible when compared to these three transitions and we find that adding a free offset parameter to the fitting function is sufficient to capture their effect. When it comes to the excited state polarizability, the issue is complicated by the increased number of relevant transitions that need to be taken into account. Particularly the presence of numerous broad transitions to a series of $^3D_1$ and $^3S_1$ states in various shells has an outsized effect on the polarizability of the $^3P_0$ state. The relevant transitions are summarized in Table 4.1 and illustrated in Fig. 4.4(a). Again, a number of higher-lying transitions outside the surveyed wavelength range play a role in the calculation of the polarizability. However, due to their large detuning, these can be subsumed into a single effective transition, characterized by a wavelength λ_{eff} and linewidth Γ_{eff}. Fitting our model to the measured tune-out and magic wavelength values, with $(\lambda_{\text{eff}}, \Gamma_{\text{eff}})$ as free parameters, we find $\lambda_{\text{eff}} \approx 376\,\text{nm}$ and $\Gamma_{\text{eff}} \approx 2\pi \times 23\,\text{MHz}$.

$\|J\rangle$	$\|J'\rangle$	$\omega_{JJ'}/2\pi$ (THz)	$\Gamma_{JJ'}/2\pi$ (MHz)	Ref.
$^1S_0$	$(6s6p)^3P_1$	539.386800	0.183	[104, 219]
	$(6s6p)^1P_1$	751.526389	29.127	[98]
	$(7/2, 5/2)_{J=1}$	865.111516	11.052	[104]
$^3P_0$	$(6s5d)^3D_1$	215.870446	0.308	[219]
	$(6s7s)^3S_1$	461.867846	1.516	[220]
	$(6s6d)^3D_1$	675.141040	4.081	[220]
	$(6s8s)^3S_1$	729.293151	0.625	[220]
	Empirical	797.204099	22.889	Fit

Table 4.1 | Overview of transition parameters used in empirical polarizability model. The initial state is denoted as $|J\rangle$ and the final state is denoted as $|J'\rangle$. The entry labeled „Empirical“ is used to designate an effective transition capturing a number of higher-lying transitions with minor contributions to the polarizabilities (see main text for details).

4.5 Towards the excited state tune-out wavelength

In addition to the ground state tune-out wavelength, we also want to measure its excited state counterpart, predicted to lie somewhere in the vicinity of 576 nm. For initial measurements on the excited state tune-out wavelength we make use of the same measurement scheme as described in Section 4.2.1. However, we find that even in the unmodulated lattice, the loss rate of atoms is large enough so as to render any sustained measurement of the atom lifetimes very imprecise. One possible mechanism responsible for this fast decay in the excited state lifetime is two-body loss from *e*-*e* scattering [221–224]. Supplementing the single-body decay $\dot{N} = -aN$, by a two-body loss term of the form $\dot{N} = -bN^2$ leads to a superexponential decay of the atom number according to:

$$N(t) = N_0 \frac{ae^{-at}}{a + N_0 b\,(1 - e^{-at})}. \tag{4.9}$$

We find that this process more closely describes our *e*-lifetime when compared to pure single-body decay, as confirmed by a χ^2 test for the goodness-of-fit. To inhibt the effect of *ee* scattering, we move from a 1D to a 3D lattice geometry. In 3D, the pinning of individual atoms to a particular lattice site is expected to significantly reduce density-dependent scattering effects [225, 226].

In addition to inelastic *ee* scattering, we also expect photon scattering from the lattice to play a role in the fast decay of the *e*-lifetime. Here, lattice photons either cause a complete loss from the trap or repumping to the ground state via some intermediate states [135, 227]. To investigate this dependency, we have measured the *e*-lifetime at various lattice depths. However, preliminary data has been inconclusive in the sense that it is difficult to separate density and light dependent scattering effects in the system. All in all, further cooling the atomic sample seems to be a necessary precondition for any sustained measurement of the excited state tune-out wavelength. For this purpose we can extend the sideband cooling scheme described in Section 3.3.2 to our 3D lattice. Additionally, the hyperfine manifolds of the fermionic isotopes of ytterbium allow for Raman sideband cooling [66]. Work on both of these cooling ideas is currently an ongoing task in our lab and will play an important role in preparing low-entropy

initial states in future experiments on our platform. In the following chapter we will see how the state-dependent wavelengths measured in our experiment can be applied to simulate some of the most fundamental theories in physics.

CHAPTER 5

Simulating lattice gauge theories

Gauge theories have proven to be some of the most effective theories for our description of physical phenomena. In particular, our understanding of the fundamental forces of nature is intimately tied to these theories [228]. This is perhaps embodied most completely in the success of the Standard Model of particle physics, combining the electromagnetic, weak and strong forces [229]. Notably exempt from this model is the force of gravity, as described by Einstein's theory [230]. A gauge theory in its own right, it has been just as successful as the Standard Model in its predictive power as relates to gravitational phenomena [231–233]. The attempt to find a unified framework for these two paradigms is perhaps the most sought after and consequential prize in all of modern physics. Apart from their obvious physical import, gauge theories also raise conceptual questions regarding the importance of symmetry in our description of reality, the extent to which gauge degrees of freedom arise simply from descriptive redundancy and the reason for their seeming ubiquity in modern physics [234–237].

For all the success of these theories, certain problems remain intractable. Quantum chromodynamics (the gauge-theoretic description of the strong force) is strongly interacting at low energies due to its running coupling constant. This poses severe problems for the study of low-energy phenomena such as quark confinement. Discretized versions of gauge theories on a lattice offer a natural remedy by inherently encoding an energy scale cut-off via the lattice spacing [4, 238–240]. This has been exploited to great effect by methods such as Monte Carlo computation [241, 242] and tensor networks [243–245]. Beyond their role as a computational tool, these lattice gauge theories (LGTs) are found to emerge as low-energy effective theories in the context of strongly-correlated electron systems in condensed matter physics [246].

Despite the proliferation of numerical methods tackling LGTs, significant challenges remain. Monte Carlo methods are known to suffer from the sign problem, leading to an exponentially increasing computation time with particle number [247]. Cold atom simulators do not suffer from this pitfall and are in some sense a natural candidate for simulating LGTs due to their discretized geometry and the degree of control afforded over a vast variety of different system parameters. Spurred on by the success of pioneering work in ion trap experiments [248], numerous proposals for the simulation of LGTs on these types of quantum simulators have been proposed in recent years [5, 6, 92, 249–259]. In the following, we show how our experiment is ideally suited to realize many of these ideas. As part of this effort, we demonstrate how LGT models can be mapped to internal degrees of freedom in our experiment and show how our

hybrid lattice-tweezer architecture provides the potential for quantum simulations of gauge theories beyond quantum electrodynamics.

5.1 Principles of lattice gauge theories

In this section, we familiarize ourselves with some of the basic building blocks of lattice gauge theories. We begin with a few words on the notion of symmetry, as this is a concept that will crop up several times during the course of this chapter.

5.1.1 A note on symmetries

In the context of modern physics, symmetries are thought of as transformations that leave an object or a collection of objects unchanged. For example, the rotation of an equilateral triangle about one-hundred twenty degrees recovers the same triangle, while a circle can be rotated about an arbitrary angle without consequence. Mathematically, this notion is formalized in the concept of groups, whereby each transformation constitutes part of a symmetry group of transformations. The rotation of the square by ninety degrees represents the action of an element of the dihedral group D_4, whereas continuous rotations on a circle are described by the unitary group U(1) and so forth. We have already encountered one physical example of such a symmetry group when examining the SU(N) symmetric interactions of ytterbium in Chapter 1. There, the nuclear spin is preserved under generalized rotations belonging to this group.

For the following discussion it will also be helpful to distinguish between global and local symmetries. Global symmetries correspond to transformations affecting all parts of space equally at the same time. These kinds of symmetries are related to conserved quantities via Noether's first theorem [260]. Prominent examples include the conservation of energy due to the homogeneity of time and the conservation of angular momentum from the isotropy of space. By contrast, local symmetries are those where the laws of physics are unaffected by transformations at each individual point in time or space. This imposes a much more rigorous standard on a physical theory than a global symmetry. In the following we will see how certain types of local symmetries known as "gauge symmetries" play a crucial role in accounting for interactions between matter and fields.

5.1.2 Fundamentals

Let us imagine space as subdivided into a regular grid of points $\boldsymbol{r} = (i, j)$.[1] Charged matter may move from point to point on this grid and its state at any instant in time can be described by a set of fermionic creation and annihilation operators, $\psi_{\boldsymbol{r}}^\dagger$ and $\psi_{\boldsymbol{r}}$ [Fig. 5.1(a)]. This is the case of free fermions moving on a 2D lattice and is described by the following Hamiltonian:

$$H_0 = -w \sum_{\boldsymbol{r},\boldsymbol{k}} (\psi_{\boldsymbol{r}}^\dagger \psi_{\boldsymbol{r}+\boldsymbol{k}} + h.c.) + \sum_{\boldsymbol{r}} m_{\boldsymbol{r}} \psi_{\boldsymbol{r}}^\dagger \psi_{\boldsymbol{r}}, \tag{5.1}$$

[1] Here we have implictily accorded the variable of time a privileged place since it remains a continous variable. This need not be the case, and formulations of LGTs with discretized time as well as space exist [261]

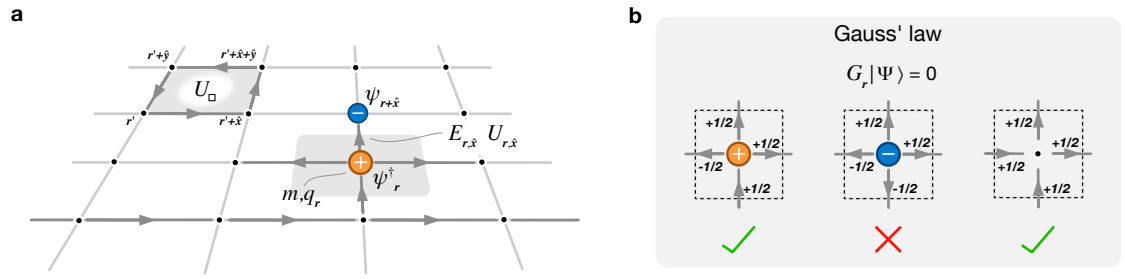

Figure 5.1 | Lattice gauge theory. (**a**) Basic ingredients of a lattice gauge theory in two spatial dimensions: Charged matter, here in the form of positrons (orange circles) and electrons (blue circles), resides on vertices of a lattice and is described by fermionic creation and annihilation operators $\psi_{\boldsymbol{r}}^\dagger$ and $\psi_{\boldsymbol{r}}$. These fermionic degrees of freedom can hop from vertex to vertex with a hopping amplitude w. In electromagnetism, charged matter acts as a source and sink for electric fields $E_{\boldsymbol{r},\boldsymbol{k}}$ (grey arrows), where $\boldsymbol{k} = \hat{\boldsymbol{x}}, \hat{\boldsymbol{y}}$ are unit vectors on the lattice. The sign of the electric field (i.e positive or negative) is indicated by the direction of the grey arrows. Together, the matter and fields must obey Gauss' law or, equivalently, local gauge invariance. To ensure that this constraint is met, additional link operators, or gauge fields, $U_{\boldsymbol{r},\boldsymbol{k}}$ are needed. By themselves, these gauge field operators can constitute a magnetic field term in the form of a closed loop on the lattice. The smallest of these loops is a square of four links and is described by a plaquette operator $U_\square$ (Eq. (5.12)) (**b**) Gauss' law can be cast into the form of an operator $G_{\boldsymbol{r}}$ (see Eq. (5.3) for definition). Only those states $|\Psi\rangle$ obeying the eigenvalue equation $G_{\boldsymbol{r}}|\Psi\rangle = 0$ are physically relevant. Here, three examples of matter and field configurations that either obey (green check mark) or violate (red cross) Gauss' law are shown for a spin-1/2 mapping of the electric field.

where w is the nearest-neighbor hopping amplitude and $\boldsymbol{k} = \hat{\boldsymbol{x}}, \hat{\boldsymbol{y}}$ indexes the unit vectors of the lattice. The mass term is staggered, $m_{\boldsymbol{r}} = m(-1)^{i+j}$, to account for fermion doubling.[2] In addition to the fermionic matter degrees of freedom described by H_0, a successful lattice gauge theory must also take account of fields.

To provide some intuition here, let's consider the particular case of quantum electrodynamics (QED), where charged matter takes the form of electrons, and fields are electric and magnetic in kind. We can think of charges as sources and sinks of electric fields. Thus an electron on a particular lattice site will give rise to an electric field $E_{\boldsymbol{r},\boldsymbol{r}+\boldsymbol{k}}$ on the links surrounding it [Fig. 5.1(a)]. A fact which is captured by Gauss' law:

$$\sum_{\boldsymbol{k}} E_{\boldsymbol{r},\boldsymbol{r}+\boldsymbol{k}} - E_{\boldsymbol{r}-\boldsymbol{k},\boldsymbol{r}} = q_{\boldsymbol{r}}, \tag{5.2}$$

where $q_{\boldsymbol{r}} = -e\psi_{\boldsymbol{r}}^\dagger\psi_{\boldsymbol{r}} + (1-(-1)^{i+j})/2$ is the (staggered) charge density of the electron. This is simply a discretized version of the familiar Gauss' law $\boldsymbol{\nabla}\cdot\boldsymbol{E} = q(\boldsymbol{r})$ from Maxwell's equations,

[2] The fermion doubling problem describes the emergence of unwanted fermionic degrees of freedom in the continuum limit of a naively discretized gauge theory. This problem has its roots in the concept of chiral symmetry, and is captured by the Nielsen-Ninomiya no-go theorem, prohibiting theories with chiral fermions (such as the Standard Model) on a lattice [262]. To navigate this issue, different kinds of fermion discretizations are possible, including Wilson fermions [4] or the staggered fermions used here [238]. The topic of regularizing chiral gauge theories is an ongoing area of research [263, 264].

where we have replaced the divergence with finite differences. Gauss' law defines an important constraint on the states $|\Psi\rangle$ of our system, since only those states that obey

$$G_{\boldsymbol{r}}\,|\Psi\rangle := \left(\sum_{k}\left(E_{\boldsymbol{r},\boldsymbol{r}+\boldsymbol{k}} - E_{\boldsymbol{r}-\boldsymbol{k},\boldsymbol{r}}\right) - q_{\boldsymbol{r}}\right)|\Psi\rangle = 0 \tag{5.3}$$

are physically relevant states.[3] Fig. 5.1(b) illustrates some examples of this constraint. Crucially, Eq. (5.3) acts as a local constraint at each lattice site and the absence of any explicit time-dependence guarantees its validity not only for the initial state of the system, but also for all future times. It follows that the physically relevant Hamiltonians obey the commutator relation:

$$[H, G_{\boldsymbol{r}}] = 0,\ \forall \boldsymbol{r}. \tag{5.4}$$

This in turn implies that our Hamiltonian is invariant under unitary transformations:

$$\begin{aligned} H &= V_{\boldsymbol{r}}^{\dagger} H V_{\boldsymbol{r}}, \\ V_{\boldsymbol{r}} &= \prod_{\boldsymbol{r}} e^{-i\alpha_{\boldsymbol{r}} G_{\boldsymbol{r}}}, \end{aligned} \tag{5.5}$$

where $\alpha_{\boldsymbol{r}}$ is a phase factor defined locally at a specific lattice site. The unitary transformations $V_{\boldsymbol{r}}$ are known as gauge transformations and constitute a symmetry group, the so-called gauge group of our theory.[4] In the case of QED, this group is the unitary group U(1). We emphasize that the symmetry described here is a local symmetry, in the sense that the invariance of the Hamiltonian to a choice of the phase factor $\alpha_{\boldsymbol{r}}$ must be respected locally at each particular lattice site $\boldsymbol{r}$.

Returning to our free fermion Hamiltonian H_0 [Eq. (5.1)], we discover, to our chagrin, that this Hamiltonian is not gauge invariant in the sense described in Eq. (5.5), since $\psi_{\boldsymbol{r}}^{\dagger}\psi_{\boldsymbol{r}+\boldsymbol{k}} \neq \psi_{\boldsymbol{r}}^{\dagger} V_{\boldsymbol{r}}^{\dagger} V_{\boldsymbol{r}+\boldsymbol{k}} \psi_{\boldsymbol{r}+\boldsymbol{k}}$. To restore local gauge invariance, we introduce additional link operators $U_{\boldsymbol{r},\boldsymbol{r}+\boldsymbol{k}}$, which transform as:

$$U_{\boldsymbol{r},\boldsymbol{r}+\boldsymbol{k}} \to U'_{\boldsymbol{r},\boldsymbol{r}+\boldsymbol{k}} = V_{\boldsymbol{r}}^{\dagger} U_{\boldsymbol{r},\boldsymbol{r}+\boldsymbol{k}} V_{\boldsymbol{r}+\boldsymbol{k}}. \tag{5.6}$$

and which obey the following commutation relations:

$$\begin{aligned} \left[U_{\boldsymbol{r},\boldsymbol{k}}, U_{\boldsymbol{r}',\boldsymbol{k}'}\right] &= 0 \\ \left[E_{\boldsymbol{r},\boldsymbol{k}}, U_{\boldsymbol{r}',\boldsymbol{k}'}\right] &= g\delta_{\boldsymbol{r}\boldsymbol{r}'}\delta_{\boldsymbol{k}\boldsymbol{k}'} U_{\boldsymbol{r},\boldsymbol{k}'}. \end{aligned} \tag{5.7}$$

Here we defined $U_{\boldsymbol{r},\boldsymbol{k}} := U_{\boldsymbol{r},\boldsymbol{r}+\boldsymbol{k}}$ and $E_{\boldsymbol{r},\boldsymbol{k}} := E_{\boldsymbol{r},\boldsymbol{r}+\boldsymbol{k}}$ for notational simplicity. Colloquially, these operators, also referred to as gauge fields, serve to compare a local change of phase on site $\boldsymbol{r}$ with its neighbor on site $\boldsymbol{r}+\boldsymbol{k}$, and compensate accordingly. In fact, the second of the two commutation relations from above tells us that $U_{\boldsymbol{r},\boldsymbol{k}}^{\dagger}$ and $U_{\boldsymbol{r},\boldsymbol{k}}$ act as raising and lowering

[3] This version of Gauss' law is a limited version of a more general Gauss' law and corresponds to a particular choice of eigenvalue or „static charge", namely that of the zero eigenvalue. The set of eigenvalues of $G_{\boldsymbol{r}}$ divide the Hilbert space of the theory into separate, dynamically isolated superselection sectors.

[4] In the language of group theory, our gauge group is a Lie group, whose generators $G_{\boldsymbol{r}}$ are elements within the associated Lie algebra.

operators for the electric field $E_{\boldsymbol{r},\boldsymbol{k}}$. Furthermore, we note that these link operators are also elements of the group U(1) and can be written in a similar fashion to Eq. (5.5). With these link operators, our Hamiltonian now becomes:

$$H_0 = -w \sum_{\boldsymbol{r},\boldsymbol{k}} (\psi^\dagger_{\boldsymbol{r}} U_{\boldsymbol{r},\boldsymbol{k}} \psi_{\boldsymbol{r}+\boldsymbol{k}} + h.c.) + m \sum_{\boldsymbol{r}} \psi^\dagger_{\boldsymbol{r}} \psi_{\boldsymbol{r}}, \tag{5.8}$$

which is known as the Kogut-Susskind Hamiltonian [238].

Let us briefly pause here and take stock of what this means. We started with Gauss' law as a constraint on our system and found that this generates gauge transformations. Consequently, we discovered that our system must be invariant under these local gauge transformations and that this requires us to introduce link operators in our Hamiltonian. Tellingly, these link operators couple to the charged matter in our theory, providing us with the interactions between matter and fields that have so far been missing from our theory. To complete the picture, we consider the free electric and magnetic field contributions:

$$H = H_0 + H_E + H_B. \tag{5.9}$$

In the continuum theory of QED, these contributions are quadratic [265]:

$$H = \frac{1}{2} \int d^3r \left[\boldsymbol{E}^2(\boldsymbol{r}) + \boldsymbol{B}^2(\boldsymbol{r}) \right], \tag{5.10}$$

and thus we can reasonably expect H_E and H_B to be of a similarly quadratic nature in its lattice counterpart. It is simple enough to discretize the free electric field while maintaining local gauge invariance:

$$H_E = \frac{g^2}{2} \sum_{\boldsymbol{r},\boldsymbol{k}} E^2_{\boldsymbol{r},\boldsymbol{k}}, \tag{5.11}$$

where g is a coupling constant that quantifies the strength of the interaction. But what about the magnetic field contribution? Unlike their electric counterpart, magnetic fields are neither sourced nor sunk by charges. If we think of magnetic field lines on our lattice, these must propagate in closed loops. The smallest of these loops, which still obeys the constraints of local gauge invariance, gives rise to a plaquette term of four link operators [Fig. 5.1(a)]:

$$U_\square = U_{\boldsymbol{r},\hat{\boldsymbol{y}}} U_{\boldsymbol{r}+\hat{\boldsymbol{x}},\hat{\boldsymbol{y}}} U^\dagger_{\boldsymbol{r}+\hat{\boldsymbol{y}},\hat{\boldsymbol{x}}} U^\dagger_{\boldsymbol{r},\hat{\boldsymbol{x}}}, \tag{5.12}$$

and therefore the magnetic part of our Hamiltonian is given by:

$$H_B = \frac{1}{4g^2} \sum_\square \left(U_\square + U^\dagger_\square \right). \tag{5.13}$$

The apperance of the coupling constant in the reciprocal is a consequence of the duality

between electric and magnetic fields. Putting everything together, we finally arrive at the lattice QED Hamiltonian:

$$H_{QED} = -w \sum_{\boldsymbol{r},\boldsymbol{k}} (\psi_{\boldsymbol{r}}^{\dagger} U_{\boldsymbol{r},\boldsymbol{k}} \psi_{\boldsymbol{r}+\boldsymbol{k}} + h.c.) + m \sum_{\boldsymbol{r}} \psi_{\boldsymbol{r}}^{\dagger} \psi_{\boldsymbol{r}} + \frac{g^2}{2} \sum_{\boldsymbol{r},\boldsymbol{k}} E_{\boldsymbol{r},\boldsymbol{k}}^2 - \frac{1}{4g^2} \sum_{\square} \left(U_{\square} + U_{\square}^{\dagger} \right). \tag{5.14}$$

The nearest-neighbor vertex coupling and the plaquette terms call to mind the toric code, which itself is an example of a $\mathbb{Z}_2$ lattice gauge theory [266]. These plaquette terms are difficult to implement experimentally as they require four-body interactions. However, a first proof-of-principle cold atom simulation has been performed by suppressing all interactions up to fourth order using an effective gradient field in an optical superlattice [83]. A non-perturbative approach has been suggested in Ref. [256].

Reducing the lattice QED Hamiltonian to the bare minimum of one spatial dimension, and doing away with the plaquette terms, results in a model known as the Schwinger model of QED [267, 268]. This model is known to exhibit confinement in the presence of an electrostatic potential and to transition to a deconfined phase via a first-order phase transition [269]. Furthermore, it predicts and describes electron-positron pair production in the presence of a sufficiently strong electric field (Schwinger effect) [270–272]. These properties, along with its relative simplicity, makes it an enticing candidate for benchmarking quantum simulations of LGTs [273]. How exactly this can be done will become clear in the following.

5.2 Mapping to a quantum simulator

From the previous discussion it is clear that any quantum simulation of lattice gauge theories must ensure two main criteria are met, namely:

I The presence of both matter and gauge degrees of freedom

II A way to engineer the Gauss' law constraint to ensure the correct gauge invariant interactions between these degrees of freedom

For quantum simulators working with neutral atoms, the first of these criteria is already difficult to enact. We might start, very naively, by placing fermionic atoms on our lattice sites to represent the matter degrees of freedom in our theory. This is fine, as far as it goes. But how to encode the gauge fields? Not only is this a bosonic degree of freedom, but the Hilbert space of the operators $U_{\boldsymbol{r},k}$ and $E_{\boldsymbol{r},k}$ is, in principle, infinitely-dimensional.

5.2.1 Quantum link models

To deal with this issue, the matter and gauge degrees of freedom of our LGT can be mapped to different internal spin states of an atom. Working in 1D, this mapping takes the following form [6, 274]:

$$U_{n,n+1} \to \frac{s^+_{n,n+1}}{\sqrt{S(S+1)}}$$
$$E_{n,n+1} \to s^z_{n,n+1},$$

where $s^z_{n,n+1}$ is the operator corresponding to the z component of the spin and $s^+_{n,n+1}$ is the raising operator for a spin state with quantum number S residing on the link between lattice sites n and $n+1$. This is known as the quantum link model (QLM) of lattice gauge theory [274] and reduces the local Hilbert space dimension of the gauge field operators to be finite-dimensional, while keeping the commutation relations between $E_{\boldsymbol{r},\boldsymbol{k}}$ and $U_{\boldsymbol{r},\boldsymbol{k}}$ intact (Eq. (5.7)). Additionally, we can map our fermionic creation and annihilation operators to Pauli operators using a Jordan-Wigner transform and obtain the QLM version of the lattice Schwinger model [250]:

$$H_{QLM} = -\frac{w}{\sqrt{S(S+1)}} \sum_{n=1}^{N-1} (\sigma^-_n s^+_{n,n+1} \sigma^-_{n+1} + h.c.) + m \sum_{n=1}^{N} \sigma^z_n + \frac{g^2}{2} \sum_{n=1}^{N-1} (s^z_{n,n+1})^2. \tag{5.15}$$

One of the first experiments to realize this model in an experiment made use of trapped ions [248]. In their simulation, Martinez *et al.* encoded the Schwinger QLM in an effective spin model with long-range interactions by tracing over the gauge degrees of freedom. More recently, the Schwinger QLM has been implemented on a quantum simulator of ultracold rubidium atoms using optical superlattices [275]. Subsequent work on the same simulator allowed the authors to probe the confining-deconfining transition in this model by tuning the topological θ-angle using a staggered optical potential of varying amplitude [276, 277]. This angle determines the magnitude of the coupling constant of the electric field $g^2(\pi - \theta)$ and as such the strength of confinement. The quantum link formulation has also been successfully employed in cold atom simulators to realize other instances of LGTs. Making use of Floquet engineering, Schweizer *et al.* were able to implement a $\mathbb{Z}_2$ LGTs in a quantum simulator of bosonic rubidium atoms in a system of double well potentials [278].

5.3 Experimental realization

We now turn to the particular implementation of LGTs in our own experiment using the QLM approach described in the previous section. The section is based in large part on a proposal made by the author's supervisor and described in some detail in Ref. [92]. Key to this proposal is the use of the Yb clock states $|g\rangle := {}^1\mathrm{S}_0$ and $|e\rangle := {}^3\mathrm{P}_0$ as well as the combination of optical lattices and tweezer arrays [Fig. 5.2(a)].

In our LGT simulation we distinguish between two kinds of lattice sites: those which may be occupied by both $|g\rangle$ and $|e\rangle$ atoms and those which are allowed to host only one of these two states *but not* both. The former we call gauge sites and the latter, matter sites. In our mapping, matter sites are assigned an integer valued index, $n \in \mathbb{Z}$, while gauge sites are

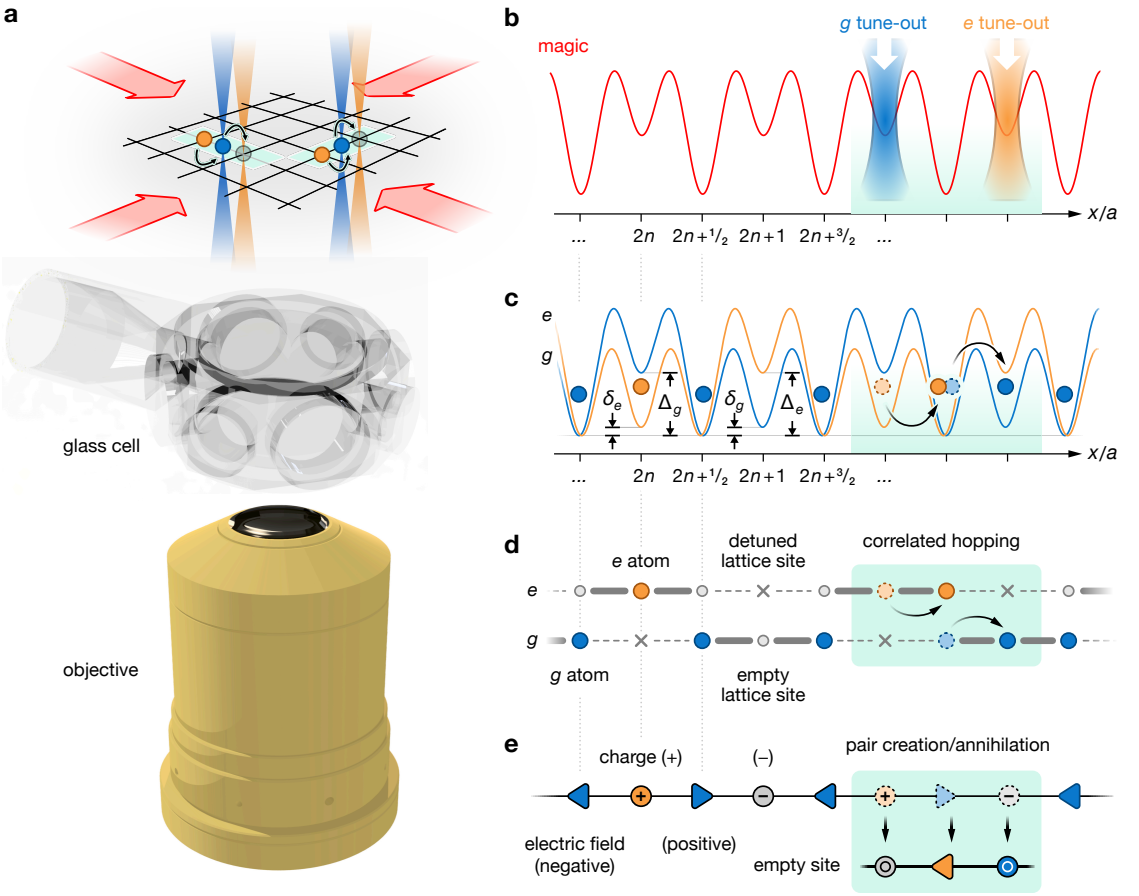

Figure 5.2 | LGTs on a hybrid quantum simulator. (**a**) Schematic of hybrid system necessary for the simulation of LGTs in our experiment. Atoms are loaded into a magic 759 nm lattice produced in our glass cell and tweezer arrays operating at the $|g\rangle$ and $|e\rangle$ tune-out are superimposed onto this lattice through our high resolution objective. (**b**) By projecting the $|g\rangle$ ($|e\rangle$) tune-out tweezers onto alternating shallow sites of a 1D magic superlattice-type potential, a series of triple wells is produced for the $|g\rangle$ ($|e\rangle$) state. (**c**) First order tunneling is inhibited by adding a detuning $\delta_g(\delta_e)$ on the middle site of each triple well. The dominant tunneling process is now given by correlated hopping of $|g\rangle$ (blue circles) and $|e\rangle$ (orange circles). (**d**) A simplified representation of the alternating triple well potential landscape, together with the correlated hopping processes described previously. (**e**) This system maps onto a chain of positive and negative charges (circles) linked by gauge fields (triangles), where the sign of the field is given by the direction of the triangle. Integer sites, where only $|g\rangle$ or $|e\rangle$ are allowed to reside, are interpreted as matter sites. Half-integers sites, where both states are allowed, are referred to as gauge sites. The distribution of charges and fields along the chain must obey Gauss' law. Correlated hopping dynamics results in the simulation of processes such as pair creation. This figure is adapted from Ref. [92].

assigned half-integer values, $n + 1/2$. Even (odd) gauge sites that host an atom in state $|g\rangle$ represent a positive (negative) electric field and vice versa for atoms in $|e\rangle$:

$$U_{n,n+1} = \begin{cases} a_{n+1/2} b^{\dagger}_{n+1/2}, & n \text{ odd} \\ b_{n+1/2} a^{\dagger}_{n+1/2}, & n \text{ even} \end{cases} \tag{5.16}$$

$$E_{n,n+1} = \frac{(-1)^n}{2} \left(a^{\dagger}_{n+1/2} a_{n+1/2} - b^{\dagger}_{n+1/2} b_{n+1/2} \right), \tag{5.17}$$

where we have introduced the ladder operators a and b for $|g\rangle$ and $|e\rangle$ atoms respectively. Matter sites are arranged according to the staggered fermion description. Even matter sites host either an $|e\rangle$ atom or a vacancy and odd matter sites either a $|g\rangle$ atom or a vacancy:

$$\psi = \begin{cases} a_n, & n \text{ odd} \\ b_n, & n \text{ even.} \end{cases} \tag{5.18}$$

The mapping so described is illustrated schematically in Figs. 5.2(c) and 5.2(d). To ensure that $|g\rangle$ and $|e\rangle$ obey the above described lattice site assignments, we will engineer a series of alternating triple well potentials. Each triple well is designed to host one of the two states. Alternating wells overlap on the first and third lattice sites, thus creating the gauge sites described previously. To engineer the correct gauge-invariant dynamics in this system, first-order tunneling processes of individual atoms must be suppressed. Rather, what is required is second-order, correlated tunneling of atoms in the lattice. The movement of an atom from its initial lattice site n onto an already occupied lattice site $n + 1/2$ must be accompanied by a correlated movement of the atom initially residing on site $n + 1/2$ to its neighboring site $n + 1$ [see Figs. 5.2(c) and 5.2(d)]. Correlated processes of this kind can be engineered by introducing a judiciously chosen detuning of the matter sites, $\delta_{e,g}$, with respect to the neighboring gauge sites. In a simulation of the Schwinger model, this correlated hopping would realize pair production processes of electrons and positrons [Figs. 5.2(d) and 5.2(e)].

5.3.1 Engineering the potentials

To create this triple well landscape, we plan to exploit the hybrid tweezer-lattice architecture of our experiment, along with the state-dependent control of the clock states presented in Chapter 4. In the simplest case, we can think of projecting state-dependent tweezers in an alternating fashion on matter sites of a square magic lattice. More concretely, a tweezer operating at the $|g\rangle$ tune-out wavelength on lattice site n would be followed by a $|e\rangle$ tune-out tweezer on site $n + 1$, followed again by a $|g\rangle$ tune-out tweezer on site $n + 2$, and so forth. In combination with the introduction of an additional small detuning between lattice sites, this allows for correlated tunneling of the kind described previously. The advantages of this setup are its relative simplicity and its robustness with respect to inhomogeneities or fluctuations in the tweezer intensities. However, a distinct drawback of this approach is its failure to scale properly to two spatial dimensions. In 2D the required potential landscape is constituted of

alternating cross-shaped blocks, outside of which tunneling is prohibited [92]. These cannot be efficiently created merely by regular arrays of tweezers projected onto a square lattice.

One way to attain the correct 2D landscape involves using an optical lattice consisting of alternating shallow and deep lattice sites [Fig. 5.2(b)]. Commonly, these kinds of potentials are realized in optical superlattices. A superlattice can be created by superposing a long and short lattice of two separate wavelengths, λ_l and λ_s, where $\lambda_l = 2\lambda_s$. To circumvent the need for two wavelengths per lattice axis, a superlattice potential can also be produced by interfering two running-wave beams of the same wavelength at an appropriate angle. In either case, however, the demands on the relative phase stability of the lattices makes superlattices difficult to engineer. An alternative approach is to use a chequerboard-type lattice which can be made to be intrinsically phase-stable by a suitable path length geometry [279, 280]. To complete the system, tune-out tweezers for $|g\rangle$ and $|e\rangle$ are projected in an alternating fashion onto the shallow lattice sites to offset the potential in a state-dependent fashion [Fig. 5.2(b)]. In this way, tunneling of $|g\rangle$ and $|e\rangle$ can be switched on and off in a local and state-dependent manner by turning on or off the desired optical tweezer at a particular lattice site. Finally, we might think of returning to our original square magic lattice and using a SLM or DMD to project tweezers onto the correct lattice sites. This approach has the additional benefit of being able to create arbitrary potential landscapes by programming the SLM or DMD in the appropriate fashion.

5.3.2 Preparing the initial state

Two prominent challenges exist when preparing the initial state for our quantum simulation of LGTs. Firstly, the atoms must occupy the low-entropy motional ground state within the triple well potentials so as to enable correct and controlled tunneling dynamics. Secondly, the initial state must be prepared in a locally gauge-invariant fashion. This requires precise control over the spatial and electronic degrees of freedom of each atom. To meet these challenges, one possibility is to load $|g\rangle$ atoms directly from a MOT into a single layer of our 3D optical lattice and subsequently to arrange the atoms into the desired lattice sites using, for example, our 532 nm tweezers. The same tweezers can then be used to induce a local light shift so that, upon exposure to a global clock pulse, these atoms remain in the $|g\rangle$ state, while the remainder are excited into the $|e\rangle$ state. Alternatively, atoms could be loaded from our MOT into a 532 nm tweezer array, as demonstrated in Section 3.5. From there, the atoms could then be cooled in the tweezers and implanted directly into the optical lattice in a controlled fashion [210]. The required cooling can be provided by sideband cooling (of the type discussed in Section 3.3.2) or, in the case of fermionic ytterbium, by Raman sideband cooling. The latter has been demonstrated to work quickly and effectively for ytterbium atoms trapped in magic optical tweezers [138] and is expected to extend analogously to optical lattices of the same wavelength.

5.3.3 Challenges

One of the keys to the success of any LGT simulation hinges on its the ability to maintain Gauss' law over relevant dynamical timescales (e.g. tunneling). Inevitably, this is a losing battle. Sooner or later, violations in the Gauss' law constraint will emerge and lead to leakage

into other gauge sectors i.e. into states designated as „unphysical“ under the rubric of Eq. (5.2). To what degree these gauge-breaking errors prohibit a sensible simulation is an ongoing area of research [281–283]. Violations of Gauss' law can arise on different experimental timescales. For time intervals significantly shorter than individual runs of the experiment, fluctuations in the lattice and tweezer array intensities may lead to heating and dissipation. The same can be said for variations in the relative positions between lattice sites and indiviudal tweezers. To minimize these fast dissipative processes, sufficient intensity stabilization is required. This can be achieved either in a passive way, by employing monolithic optical components, dispensing with redunant degrees of freedom and reducing optical path lengths, or, in an active fashion, by using appropiate intensity servos and feedback loops. On timescales approximating those of individual runs, variations in laser intensity or inhomogeneities in the tweezer array can lead to disordered potential landscapes, where, for example, every run of the experiment sees a different set of staggered detunings $\delta_{e,g}$ or tunneling energies, w. On very long timescales, thermal drifts and ambient pressure changes may cause gradual misalignment in various optical paths. This can create additional disorder in the system, for example, via the misalignment of tweezers relative to the optical lattice. This can be compensated by recalibrating each sub-system (e.g. the optical lattice alignment) intermittently. Another problem is caused by entropy, introduced into the system through an imperfect preparation of the inital state. More specifically, entropy is caused by a misplaced atom on a particular lattice site or the absence of an atom from a site which is meant to be occupied. To curtail this issue, atoms could initially be loaded into a very deep optical lattice so that any and all tunneling processes are inhibited, before adiabatically ramping up to a shallower initial state lattice. In addition, careful intensity balancing of optical tweezers might also be helpful in this situation, though the requirements are stringent. Given typical tunneling rates on the order of 10s-100s of Hz and tweezer depths on the order of 10s-100s of kHz, sub-percent level intensity homogenization is necessary [92, 284].

5.3.4 Outlook and perspectives

To conclude this chapter, we briefly touch on a number of prospective research directions which our LGT quantum simulation platform might be suited to exploring. To benchmark our LGT simulator, we will initially work in 1D systems to realize the pair production described by the Schwinger model in Section 5.1.2. Here, we can use the architecture of our simulator to our advantage, by parallelizing this simulation in many 1D chains within our 2D geometry.

Our experimental platform is naturally suited to the simulation of higher dimensional non-abelian theories thanks to the presence of nuclear spin degrees of freedom in fermionic Yb. Non-abelian theories are particularly interesting given the role they play in the Standard Model of particle phyiscs. In this model, the strong nuclear force adheres to an SU(3) local gauge symmetry, while the elektroweak force possesses a $\mathrm{SU}(2)\otimes\mathrm{U}(1)$ symmetry. As discussed in Chapter 1, ^{171}Yb has a nuclear spin of $I = 1/2$, and therefore features SU(2)-symmetric interactions. In our experiment, we have already successfully demonstrated the loading and trapping of this isotope in a MOT and an optical lattice. We have also shown that relevant spectroscopic methods can be extended to this isotope as needed (see Appendix C). Furthermore, the isotope shift between ^{174}Yb and ^{171}Yb is small enough ($\sim 1-2\,\mathrm{GHz}$) [285, 286]

so that the state-dependent control outlined in this chapter is expected to be extendable to ^{171}Yb with minimal effort. All of this indicates that the simulation of SU(2) LGTs represents an experimentally feasible research direction in our experiment.

Maintaing the 1D architecture described in Section 5.3, a novel research direction concerns the simulation of particle scattering experiments. Over the course of many decades, particle collider experiments have proven enormously successful at furthering our understanding of the Standard Model of particle physics [287, 288]. In these experiments, subatomic particles are accelerated to relativistic speeds and caused to collide with one another. The products of these high energy scattering events are recorded and their behavior used to infer something about the underlying theories. Recently, several ideas for very elementary particle scattering experiments of this type have been proposed for quantum computers and simulators [289–292]. By only observing the end products of scattering events, particle colliders are in some sense bound to the time $t \to \infty$ limit. By contrast, cold atom simulators offer the tantalizing possibility of resolving the entire time evolution of such scattering processes. While these experiments would be extremely simplified and rudimentary approximations to the zoo of particles encountered in high-ernergy accelerators, they nevertheless raise the possibility of new insights.

As described in Section 5.3.1, it is straightforward to extend our experiment to two spatial dimensions. Here, initial experimental investigations might focus on basic unanswered questions regarding the nature of the ground state phase diagram of QED in (2+1)D [293–295]. Does (2+1)D QED on a lattice allow for both confined and deconfined states? If so, what kind of phase transition can we expect and into what universality class does it fall?

Conclusions and outlook

In this thesis, we designed and built a new hybrid quantum simulation platform for cold ytterbium atoms featuring both an optical lattice and a tweezer array. We used this platform to perform measurements on three state-dependent wavelengths for the ground $\left({}^1S_0\right)$ and metastable excited $\left({}^3P_0\right)$ states in ^{174}Yb, and discussed our intentions of using these wavelengths in combination with our hybrid architecture to simulate LGTs in our experiment.

As part of the construction process, we designed and assembled a compact, yet accessible ultra-high vacuum system, commanding vacuum lifetimes on the order of several tens of seconds. We also incorporated a number of magnetic field coils into this system, designed for fast and flexible current switching. Trapping and cooling of atoms is facilitated by numerous laser setups of varying wavelengths, three of which have been frequency stabilized to a high-finesse reference cavity using an offset locking scheme. Together with the remote controlled infrastructure of the lab, these systems allow for sub-second cycle times and the concomitant collection of large amounts of data on short timescales.

We used this platform to implement a number of standard experimental methods (Chapter 3). Our experiment is capable of performing both absorption and fluoresence imaging, and to state-selectively image ground and excited states using a dedicated repumping transition. We managed to load atoms from a MOT into a 759 nm magic optical lattice and therein probe the atoms using either Rabi, sideband or modulation spectroscopy. We also realized sideband cooling in a 1D lattice. Additionally, we managed to load, cool and image individual atoms in a 532 nm tweezer arrays using orthogonal AODs in combination with our high resolution microscope objective.

In Chapter 4, we applied these methods to measure state-dependent wavelengths for the ground and excited states of the clock transition in ^{174}Yb. In particular, we made use of high-resolution, magnetically induced, optical clock (Rabi) spectroscopy to determine two magic wavelengths at 459.6 nm and 552.6 nm. In addition, we made use of a method previously developed in Ref. [91] to determine the ground state tune-out wavelength at 553.3 nm. We then used our knowledge of this wavelength to determine the excited state polarizability at that value and benchmarked a numerical model for the polarizability of both states using our experimental data. Finally, we briefly sketched the ongoing challenges in measuring the excited state tune-out wavelength in our lab. The measurement of these wavelengths offers novel perspectives for state-selective addressing and cooling, thus providing a valuable tool for advanced quantum simulation [141, 296, 297] and computation schemes [51, 153, 298]. In our own experiment, we look to use tweezer arrays operating at tune-out wavelengths to engineer a state-dependent triple well potential for the simulation of LGTs.

In its current state, the experiment is capable of loading and cooling atoms in either the lattice or the tweezer array. The major outstanding challenge is to combine both of these elements to function as a cohesive whole. Here, we envisage the ability to address individual lattice sites in a targeted fashion using individiual tweezers, to dynamically re-arrange atoms in the lattice and to hand over atoms from the tweezers to the lattice and vice versa [210, 299]. This will require the following steps:

- Isolating a single layer of our 3D lattice.
- Single-site resolved fluoresence imaging (quantum gas microscopy) in the lattice.
- Efficient cooling to the motional ground state in the lattice, either by extending the sideband cooling scheme described in Section 3.3.2 to more than one dimension and/or by implementing Raman sideband cooling.
- Implementing additional tweezer arrays at both the ground state and excited state tune-out wavelengths [92].

In the introduction to this thesis, we discussed a number of research directions for which a hybrid lattice-tweezer platform might be well-suited. We believe that with the additional upgrades outlined above, our experiment is well positioned to investigate these outstanding issues. Chiefly, we will pursue quantum simulations of QLM LGTs in (1+1)D and (2+1)D. Here, the fermionic isotopes will enable us to explore non-abelian SU(N) LGTs, while our hybrid architecture will permit us to extend our simulations into two spatial dimensions. This in turn will allow us to look at the role and character of confinement in two dimensions. Research is also needed to develop a deeper understanding of thermalization dynamics in LGTs. This long-standing problem has recently begun to gain traction after initial experimental investigations on a cold atom quantum simulator [89, 90]. This is closely related to questions surrounding the effect of constraints in LGTs on localization in quantum many-body systems [300].

In contrast to the analog quantum simulation perspectives outlined above, our apparatus also provides the possibility for investigations into gate-based digital quantum computing strategies. One could imagine collisional gates based on the spin-exchange interactions between ground and excited states in fermionic Yb [298]. These would offer a complementary alternative to the Rydberg-mediated, gate-based approach commonly pursued in neutral atom quantum computing. Spin-exchange interaction could be quickly turned on and off using an optically induced effective magnetic field and thus used to perform precisely controlled entangling operations between nuclear spin qubits.

All in all, we believe our hybrid platform to be in an excellent position for navigating the challenges and opportunities ahead and we look forward to new and exciting insights into the physics of quantum many body systems.

Appendices

Appendix A Atomic beam system

In this appendix we document some of our experience with the AOSense beam source. Ours was the first experiment to work with this atomic beam source for the Yb atom. Due to a number of unforseen circumstances, we have had to replace the oven and subsequently re-bake the system a total of three times. The first two iterations of our oven employed an old nozzle design (stacked microcapillary array) and failed due to clogging. It was also found that the first of these ovens had consumed Yb much faster than anticipated so that by the time of clogging, hardly any Yb remained in the oven. Our current oven is using the newest nozzle design from AOSense (solid block featuring an array of small holes), which is expected to be much less prone to clogging and exhibt a longer lifetime.

A.1 Nozzle clogging

Under day-to-day operation, we turn on the oven in the morning, steadily ramp to a temperature of 420°C, maintain this temperature for $\approx 10-12$hrs and then ramp the oven back down to room temperature at the end of the day. The Zeeman slower hot window is held at a constant 380°C.

Symptoms of clogging.—The clogging of the oven was heralded by a number of different signs including:

- A sustained period of decay in the MOT loading rate over several weeks [see Fig. A.1(a)].
- Coating of the spectroscopy viewports closest to the oven with Yb beyond what is anticipated by line-of-sight [see Fig. A.1(b)]. This prevented us from performing absorption spectroscopy on the atomic beam to confirm our suspicions of nozzle clogging. The smaller spectroscopy viewports after the 2D MOT were also coated.
- Pronounced oscillations in the oven temperature over a range of ±5°C [see Fig. A.1(c)].
- Steadily increasing oven power consumption (this is somewhat speculative. The trend is not well-correlated with the decay in MOT loading time, as it occurs on much longer timescales)

Diagnosis and possible origin.—Having discussed these symptoms with AOSense and looked at other possible culprits (e.g. drifts in optics), we reached the conclusion that the nozzle was most likely clogging. A possible mechanism suggested by AOSense for this issue was the presence of large amounts of hydrogen in the Yb used in the oven. This hydrogen reacts with Yb above 400°C to form YbH_2. Inside the capillaries, this process is exacerbated by the

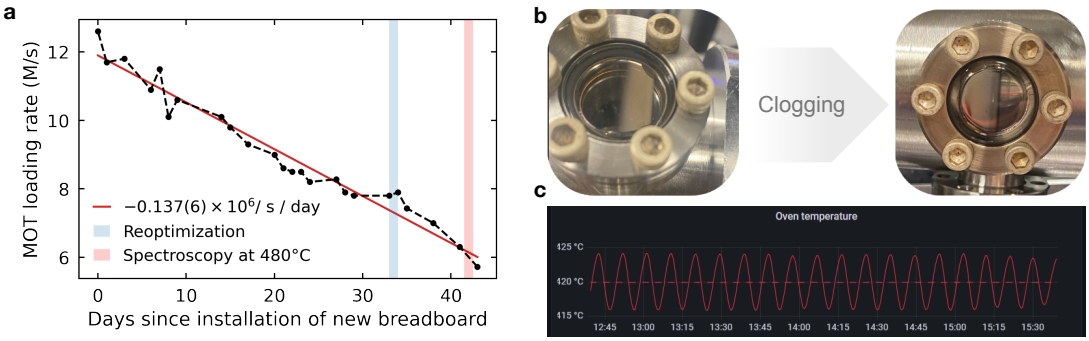

Figure A.1 | Oven clogging. (**a**) Plot of the MOT loading rate over the course of several weeks. The steady decay in the loading rate is a strong indicator of nozzle clogging. The legend label "Reoptimization" corresponds to us scanning several experimental parameters (e.g. laser detuning and magnetic field strengths) to try to find a new optimum loading rate. (**b**) Pictures of the CF16 viewports close the oven before and during clogging, showing an increase in the coated area beyond what is expected from line-of-sight. (**c**) Oven temperature fluctations were found to be more pronounced as the oven was clogging.

restricted gas flow. Once Yb has deposited on the walls of the capillaries and formed this compound, it no longer evaporates away. The cycle is repeated until the capillaries clog.

Solution.—The only course of action was to swap the oven and run it at a lower temperature (our current and newest oven runs at 380°C). For this purpose, AOSense provides detailed instructions on the swapping procedure, including the bake temperatures and the getter reactivation. Here we only note down a few practical tips. Wrapping the beam source in aluminium foil for baking can be tricky, especially around the large 2D MOT viewports. We have found it sufficient to loosely place aluminium foil over this area of the beam source, making sure to leave a small air gap so that the aluminium foil does not touch the viewports and is not crumpled. For baking, we use heating tape and are careful to avoid placing the heating tape over the viewports. The beam source also has numerous pins for electrical connections. These are very delicate and we strongly suggest that aluminium foil be placed in between and around these pins and not on top of them. During the oven swap, we used argon to flood the oven and maintained a flow of argon throught the swap. The pressure was monitored using a pressure regulator. The CF16 viewports used for spectroscopy come in two different thicknesses. The thicker viewports require 8-32, 0.75″ long bolts. When it comes to reactivating the oven, AOSense now recommends *not* to cycle the oven several times. Rather a single ramp-up to 500°C for a few minutes maximum will suffice to burn off any surface-level contaminants.

A.2 Other issues

We typically observe a much larger flux from the oven during the ramp-up phase than expected from the displayed oven temperature. For example, at 410°C a flux value closer to the one expected at 480°C was observed. This likely means a much better thermal contact between the heaters and the reservoir than between the reservoir and the temperature sensor. We therefore reduce the ramp-up speed as we approach the setpoint value, in order to prevent excessive fluxes.

During the installation of the atom source on the main vacuum chamber we accidentally vented the oven to air by not fully closing the gate valve between the beam source and the rest

of the vacuum system. Here, it is critical that the gate valve is closed until a full mechanical stop is felt. This is often accompanied by a clicking sound, after which further rotation is required to reach the mechanical stop.

Appendix B First MOT signal

Our first MOT signal was obtained prior to the installing our microscope objective. Here, we describe the initial steps to obtain a MOT in our system and compare it to the current configuration with our objective.

The presence of two differential pumping stages in our vacuum system made it difficult to channel the atomic beam from the oven into the glass cell. To overcome this challenge, we aligned 399 nm laser light to propagate vertically through the glass cell [i.e. along the z axis - see e.g. Fig. 2.3(b)], with which we looked for any fluoresence in the cell. The fluoresence was capture on a Mako camera in real time. At the same time, we changed the 2D MOT and Zeeman slower alignment to attempt to steer the atomic beam through all the differential pumping stages. We found that changing the vertical alignment of the Zeeman slower and the 2D MOT beam closest to the glass cell had the most significant effect on the strength of the fluoresence. The quarter waveplates had already been tuned to the correct rotation and the horizontal alignment of the Zeeman slower and 2D MOT beams made little to no difference. Also, changing the detuning of the Zeeman slower by 5 MHz in either direction was only found to worsen the visibility of the atomic fluoresence. Once the inital (very weak) fluoresence signal had been detected on the camera, it was a matter of beam walking the 2D MOT and iteratively optimizing the Zeeman slower pointing, to maximize the fluoresence signal in the glass cell until it was observable by eye.

We also tried to play around with the alignment of the crossed slowing beams. Here we observed some strange effects, including the appearance of mysterious fringes and holes in the blue probe beam signal. We thus returned the crossed slowing alignment to the position where the fluoresence signal was found to be most homogeneous.

Sure of the fact that we had atoms in the cell, we turned on the four MOT beams (two retroreflected in the xy-plane and two independent, counterpropagating beams along z). These were set to operate at the maximum power of ≈ 80 mW, while the slowing beams were each set to ≈ 10 mW. The oven at this point was operated at 440°C. The main MOT coils were operating in anti-Helmholtz configuration with a current of 3 A, corresponding to a field gradient of $\approx 5.85\,\mathrm{G/cm}$. These conditions were maintained for 30 s a piece, within which we almost immediately saw a diffuse green cloud appearing in the center of our glass cell. Our first MOT.

Having established our MOT in this way, we optimized the loading rate by scanning a number of experimental parameters (detuning and power of the MOT and slowing beams, the magnetic field strength etc.), while observing the atom number. In this way, we were able to obtain a repeatable maximum loading rate of $\approx 30 \times 10^6$ s. After the installation of our microscope objective, the optimal parameter set changed and the loading rate decreased considerably so that we currently load, at most, $\approx 14 \times 10^6$ s.

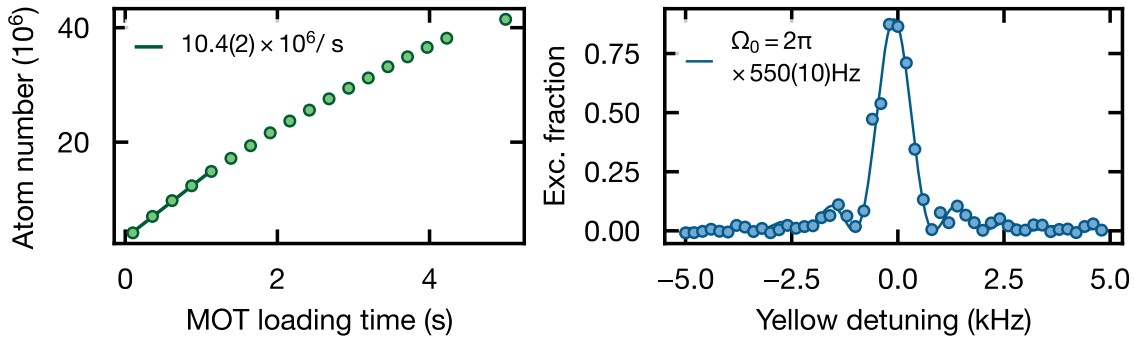

Figure C.1 | **^{171}Yb.** (**a**) MOT loading curve for ^{171}Yb, showing a much reduced loading rate when compared to the $\approx 30 \times 10^6$/ s loading rate of ^{174}Yb. This is due to the lower natural abundance of ^{171}Yb. (**b**) Rabi spectroscopy performed on the $|^1S_0, m_F = +1/2\rangle \leftrightarrow |^3P_0, m_F = -1/2\rangle$ with 1 ms of optical pumping and 30 G external field.

Appendix C Working with ^{171}Yb

In addition to the bosonic isotope ^{174}Yb, we also worked with fermionic ^{171}Yb. This was done after taking data for the state-dependent potentials, but before installing our microscope objective. To perform standard techniques such as MOT loading, cooling and spectroscopy, the frequency of the all our lasers had to be adjusted by to match the corresponding isotope shift (≈ 1.8 GHz [99]). This involved re-optimizing the cavity lock at the new set frequencies for the blue, green and yellow lasers. We also had to tune the ti:sapph frequency to the ^{171}Yb magic frequency.

Due to its lower natural abundance (14% compared to ^{174}Yb's 32%), the MOT loading rate was significantly reduced for ^{171}Yb [see Fig. C.1(a)]. To perfom Rabi spectrosocpy, we implement optical pumping on the $^1S_0 \leftrightarrow {}^3P_1$ transition so that atoms which are excited in the Rabi spectroscopy are not lost in the "dark" hyperfine state. Specifically, for Rabi spectroscopy on the $m_F = +1/2 \leftrightarrow m_F = -1/2$ transition, optical pumping is performed on the $^1S_0\,|F = 1/2, m_F = -1/2\rangle \leftrightarrow {}^3P_1\,|F = 3/2, m_F = +1/2\rangle$ transition. The Rabi spectrum obtained in this way in our 1D magic lattice for an optical pumping duration of 1 ms and applied external magnetic field of 30 G is shown in Fig. C.1(b).

An attempt was also made to perform sideband spectroscopy and cooling. Though we managed to obtain a sideband spectrum, we were hampedered by the presence of technical noise, leading to a very noisy sideband spectrum. At the time we wanted to push our tweezer array forward and install the microscope objective, so no further tests on ^{171}Yb were performed. However, we hope to be able to return to this isotope in due course and improve on the work shown in this short appendix.

References

[1] J. Turner, P. Anderson, T. Lachlan-Cope, S. Colwell, T. Phillips, A. Kirchgaessner, G. J. Marshall, J. C. King, T. Bracegirdle, D. G. Vaughan, V. Lagun, and A. Orr, *Record low surface air temperature at Vostok station, Antarctica*, Journal of Geophysical Research: Atmospheres **114**, https://doi.org/10.1029/2009JD012104 (2009) (see p. 1).

[2] R. P. Feynman, *Simulating physics with computers*, International Journal of Theoretical Physics **21**, 467 (1982) (see pp. 1, 2).

[3] I. Bloch, J. Dalibard, and W. Zwerger, *Many-body physics with ultracold gases*, Rev. Mod. Phys. **80**, 885 (2008) (see pp. 1, 2, 13).

[4] K. G. Wilson, *Confinement of quarks*, Phys. Rev. D **10**, 2445 (1974) (see pp. 1–3, 75, 77).

[5] U.-J. Wiese, *Towards quantum simulating QCD*, Nuclear Physics A **931**, 246 (2014) (see pp. 1, 75).

[6] J. C. Halimeh, M. Aidelsburger, F. Grusdt, P. Hauke, and B. Yang, *Cold-atom quantum simulators of gauge theories*, arXiv:2310.12201 (see pp. 1, 75, 80).

[7] X.-G. Wen, *Colloquium: Zoo of quantum-topological phases of matter*, Rev. Mod. Phys. **89**, 041004 (2017) (see pp. 1, 2).

[8] W. D. Phillips, *Nobel Lecture: Laser cooling and trapping of neutral atoms*, Rev. Mod. Phys. **70**, 721 (1998) (see p. 1).

[9] C. Kittel and H. Kroemer, *Thermal physics*, 2nd ed. (W.H. Freeman, San Francisco, 1980) (see p. 1).

[10] R. Grimm, M. Weidemüller, and Y. B. Ovchinnikov, *Optical Dipole Traps for Neutral Atoms*, in , Vol. 42, edited by B. Bederson and H. Walther, Advances In Atomic, Molecular, and Optical Physics (Academic Press, 2000), 95 (see pp. 1, 9, 10, 13).

[11] P. Jessen and I. Deutsch, *Optical Lattices*, in , Vol. 37, edited by B. Bederson and H. Walther, Advances In Atomic, Molecular, and Optical Physics (Academic Press, 1996), 95 (see p. 1).

[12] M. Greiner and S. Fölling, *Optical lattices*, Nature **453**, 736 (2008) (see p. 1).

[13] A. M. Kaufman and K.-K. Ni, *Quantum science with optical tweezer arrays of ultracold atoms and molecules*, Nat. Phys. **17**, 1324 (2021) (see p. 1).

[14] C. Chin, R. Grimm, P. Julienne, and E. Tiesinga, *Feshbach resonances in ultracold gases*, Rev. Mod. Phys. **82**, 1225 (2010) (see p. 2).

[15] D. Jaksch, C. Bruder, J. I. Cirac, C. W. Gardiner, and P. Zoller, *Cold Bosonic Atoms in Optical Lattices*, Phys. Rev. Lett. **81**, 3108 (1998) (see pp. 2, 13).

[16] M. Lewenstein, A. Sanpera, V. Ahufinger, B. Damski, A. Sen(De), and U. Sen, *Ultracold atomic gases in optical lattices: mimicking condensed matter physics and beyond*, Advances in Physics **56**, 243 (2007) (see pp. 2, 13).

[17] I. Bloch, J. Dalibard, and S. Nascimbène, *Quantum simulations with ultracold quantum gases*, Nat. Phys. **8**, 267 (2012) (see pp. 2, 13).

[18] C. Gross and I. Bloch, *Quantum simulations with ultracold atoms in optical lattices*, Science **357**, 995 (2017) (see pp. 2, 13).

[19] I. Bloch, *Quantum simulations come of age*, Nat. Phys. **14**, 1159 (2018) (see p. 2).

[20] M. C. Gutzwiller, *Effect of Correlation on the Ferromagnetism of Transition Metals*, Phys. Rev. Lett. **10**, 159 (1963) (see p. 2).

[21] J. Hubbard and B. H. Flowers, *Electron correlations in narrow energy bands*, Proceedings of the Royal Society of London. Series A. Mathematical and Physical Sciences **276**, 238 (1963) (see p. 2).

[22] M. Greiner, O. Mandel, T. Esslinger, T. W. Hänsch, and I. Bloch, *Quantum phase transition from a superfluid to a Mott insulator in a gas of ultracold atoms*, Nature **415**, 39 (2002) (see pp. 2, 13).

[23] D. Greif, T. Uehlinger, G. Jotzu, L. Tarruell, and T. Esslinger, *Short-Range Quantum Magnetism of Ultracold Fermions in an Optical Lattice*, Science **340**, 1307 (2013) (see p. 2).

[24] R. A. Hart, P. M. Duarte, T.-L. Yang, X. Liu, T. Paiva, E. Khatami, R. T. Scalettar, N. Trivedi, D. A. Huse, and R. G. Hulet, *Observation of antiferromagnetic correlations in the Hubbard model with ultracold atoms*, Nature **519**, 211 (2015) (see p. 2).

[25] L. W. Cheuk, M. A. Nichols, K. R. Lawrence, M. Okan, H. Zhang, E. Khatami, N. Trivedi, T. Paiva, M. Rigol, and M. W. Zwierlein, *Observation of spatial charge and spin correlations in the 2D Fermi-Hubbard model*, Science **353**, 1260 (2016) (see p. 2).

[26] P. A. Lee, N. Nagaosa, and X.-G. Wen, *Doping a Mott insulator: Physics of high-temperature superconductivity*, Rev. Mod. Phys. **78**, 17 (2006) (see p. 2).

[27] N. Goldman, J. C. Budich, and P. Zoller, *Topological quantum matter with ultracold gases in optical lattices*, Nat. Phys. **12**, 639 (2016) (see p. 2).

[28] W. S. Bakr, J. I. Gillen, A. Peng, S. Fölling, and M. Greiner, *A quantum gas microscope for detecting single atoms in a Hubbard-regime optical lattice*, Nature **462**, 74 (2009) (see p. 2).

[29] J. F. Sherson, C. Weitenberg, M. Endres, M. Cheneau, I. Bloch, and S. Kuhr, *Single-atom-resolved fluorescence imaging of an atomic Mott insulator*, Nature **467**, 68 (2010) (see p. 2).

[30] M. F. Parsons, F. Huber, A. Mazurenko, C. S. Chiu, W. Setiawan, K. Wooley-Brown, S. Blatt, and M. Greiner, *Site-Resolved Imaging of Fermionic* ^{6}Li *in an Optical Lattice*, Phys. Rev. Lett. **114**, 213002 (2015) (see p. 2).

[31] L. W. Cheuk, M. A. Nichols, M. Okan, T. Gersdorf, V. V. Ramasesh, W. S. Bakr, T. Lompe, and M. W. Zwierlein, *Quantum-Gas Microscope for Fermionic Atoms*, Phys. Rev. Lett. **114**, 193001 (2015) (see p. 2).

[32] M. Miranda, R. Inoue, Y. Okuyama, A. Nakamoto, and M. Kozuma, *Site-resolved imaging of ytterbium atoms in a two-dimensional optical lattice*, Phys. Rev. A **91**, 063414 (2015) (see p. 2).

[33] E. Haller, J. Hudson, A. Kelly, D. A. Cotta, B. Peaudecerf, G. D. Bruce, and S. Kuhr, *Single-atom imaging of fermions in a quantum-gas microscope*, Nat. Phys. **11**, 738 (2015) (see p. 2).

[34] G. J. A. Edge, R. Anderson, D. Jervis, D. C. McKay, R. Day, S. Trotzky, and J. H. Thywissen, *Imaging and addressing of individual fermionic atoms in an optical lattice*, Phys. Rev. A **92**, 063406 (2015) (see p. 2).

[35] R. Yamamoto, J. Kobayashi, T. Kuno, K. Kato, and Y. Takahashi, *An ytterbium quantum gas microscope with narrow-line laser cooling*, New Journal of Physics **18**, 023016 (2016) (see pp. 2, 8).

[36] M. Endres, M. Cheneau, T. Fukuhara, C. Weitenberg, P. Schauß, C. Gross, L. Mazza, M. C. Bañuls, L. Pollet, I. Bloch, and S. Kuhr, *Single-site- and single-atom-resolved measurement of correlation functions*, Applied Physics B **113**, 27 (2013) (see p. 2).

[37] M. Rispoli, A. Lukin, R. Schittko, S. Kim, M. E. Tai, J. Léonard, and M. Greiner, *Quantum critical behaviour at the many-body localization transition*, Nature **573**, 385 (2019) (see p. 2).

[38] A. Lukin, M. Rispoli, R. Schittko, M. E. Tai, A. M. Kaufman, S. Choi, V. Khemani, J. Léonard, and M. Greiner, *Probing entanglement in a many-body–localized system*, Science **364**, 256 (2019) (see p. 2).

[39] J. Koepsell, D. Bourgund, P. Sompet, S. Hirthe, A. Bohrdt, Y. Wang, F. Grusdt, E. Demler, G. Salomon, C. Gross, and I. Bloch, *Microscopic evolution of doped Mott insulators from polaronic metal to Fermi liquid*, Science **374**, 82 (2021) (see p. 2).

[40] Y.-G. Zheng et al., *Efficiently Extracting Multi-Point Correlations of a Floquet Thermalized System*, arXiv:2210.08556 (see p. 2).

[41] A. D. Ludlow, M. M. Boyd, J. Ye, E. Peik, and P. O. Schmidt, *Optical atomic clocks*, Rev. Mod. Phys. **87**, 637 (2015) (see pp. 2, 55).

[42] T. Bothwell, C. J. Kennedy, A. Aeppli, D. Kedar, J. M. Robinson, E. Oelker, A. Staron, and J. Ye, *Resolving the gravitational redshift across a millimetre-scale atomic sample*, Nature **602**, 420 (2022) (see p. 2).

[43] N. Schlosser, G. Reymond, I. Protsenko, and P. Grangier, *Sub-poissonian loading of single atoms in a microscopic dipole trap*, Nature **411**, 1024 (2001) (see pp. 2, 13).

[44] A. Cooper, J. P. Covey, I. S. Madjarov, S. G. Porsev, M. S. Safronova, and M. Endres, *Alkaline-Earth Atoms in Optical Tweezers*, Phys. Rev. X **8**, 041055 (2018) (see pp. 2, 13).

[45] M. A. Norcia, A. W. Young, and A. M. Kaufman, *Microscopic Control and Detection of Ultracold Strontium in Optical-Tweezer Arrays*, Phys. Rev. X **8**, 041054 (2018) (see pp. 2, 13).

[46] D. Barredo, S. de Léséleuc, V. Lienhard, T. Lahaye, and A. Browaeys, *An atom-by-atom assembler of defect-free arbitrary two-dimensional atomic arrays*, Science **354**, 1021 (2016) (see pp. 2, 13).

[47] D. Barredo, V. Lienhard, S. de Léséleuc, T. Lahaye, and A. Browaeys, *Synthetic three-dimensional atomic structures assembled atom by atom*, Nature **561**, 79 (2018) (see p. 2).

[48] M. Endres, H. Bernien, A. Keesling, H. Levine, E. R. Anschuetz, A. Krajenbrink, C. Senko, V. Vuletic, M. Greiner, and M. D. Lukin, *Atom-by-atom assembly of defect-free one-dimensional cold atom arrays*, Science **354**, 1024 (2016) (see pp. 2, 13).

[49] H. Kim, W. Lee, H.-g. Lee, H. Jo, Y. Song, and J. Ahn, *In situ single-atom array synthesis using dynamic holographic optical tweezers*, Nature Communications **7**, 13317 (2016) (see pp. 2, 13).

[50] A. Kumar, T.-Y. Wu, F. Giraldo, and D. S. Weiss, *Sorting ultracold atoms in a three-dimensional optical lattice in a realization of Maxwell's demon*, Nature **561**, 83 (2018) (see p. 2).

[51] M. A. Norcia et al., *Iterative assembly of ^{171}Yb atom arrays in cavity-enhanced optical lattices*, arXiv:2401.16177 (see pp. 2, 12, 64, 87).

[52] A. Gaëtan, Y. Miroshnychenko, T. Wilk, A. Chotia, M. Viteau, D. Comparat, P. Pillet, A. Browaeys, and P. Grangier, *Observation of collective excitation of two individual atoms in the Rydberg blockade regime*, Nat. Phys. **5**, 115 (2009) (see p. 2).

[53] E. Urban, T. A. Johnson, T. Henage, L. Isenhower, D. D. Yavuz, T. G. Walker, and M. Saffman, *Observation of Rydberg blockade between two atoms*, Nat. Phys. **5**, 110 (2009) (see p. 2).

[54] M. Saffman, T. G. Walker, and K. Mølmer, *Quantum information with Rydberg atoms*, Rev. Mod. Phys. **82**, 2313 (2010) (see p. 2).

[55] T. Wilk, A. Gaëtan, C. Evellin, J. Wolters, Y. Miroshnychenko, P. Grangier, and A. Browaeys, *Entanglement of Two Individual Neutral Atoms Using Rydberg Blockade*, Phys. Rev. Lett. **104**, 010502 (2010) (see p. 2).

[56] H. Labuhn, D. Barredo, S. Ravets, S. de Léséleuc, T. Macrì, T. Lahaye, and A. Browaeys, *Tunable two-dimensional arrays of single Rydberg atoms for realizing quantum Ising models*, Nature **534**, 667 (2016) (see p. 2).

[57] T. M. Graham, M. Kwon, B. Grinkemeyer, Z. Marra, X. Jiang, M. T. Lichtman, Y. Sun, M. Ebert, and M. Saffman, *Rydberg-Mediated Entanglement in a Two-Dimensional Neutral Atom Qubit Array*, Phys. Rev. Lett. **123**, 230501 (2019) (see p. 2).

[58] A. Keesling, A. Omran, H. Levine, H. Bernien, H. Pichler, S. Choi, R. Samajdar, S. Schwartz, P. Silvi, S. Sachdev, P. Zoller, M. Endres, M. Greiner, V. Vuletić, and M. D. Lukin, *Quantum Kibble–Zurek mechanism and critical dynamics on a programmable Rydberg simulator*, Nature **568**, 207 (2019) (see p. 2).

[59] S. Ebadi, T. T. Wang, H. Levine, A. Keesling, G. Semeghini, A. Omran, D. Bluvstein, R. Samajdar, H. Pichler, W. W. Ho, S. Choi, S. Sachdev, M. Greiner, V. Vuletić, and M. D. Lukin, *Quantum phases of matter on a 256-atom programmable quantum simulator*, Nature **595**, 227 (2021) (see pp. 2, 13).

[60] G. Semeghini et al., *Probing topological spin liquids on a programmable quantum simulator*, Science **374**, 1242 (2021) (see pp. 2, 13).

[61] W. J. Eckner, N. Darkwah Oppong, A. Cao, A. W. Young, W. R. Milner, J. M. Robinson, J. Ye, and A. M. Kaufman, *Realizing spin squeezing with Rydberg interactions in an optical clock*, Nature **621**, 734 (2023) (see p. 2).

[62] A. Cao, W. J. Eckner, T. L. Yelin, A. W. Young, S. Jandura, L. Yan, K. Kim, G. Pupillo, J. Ye, N. D. Oppong, and A. M. Kaufman, *Multi-qubit gates and 'Schrödinger cat' states in an optical clock*, arXiv:2402.16289 (see p. 2).

[63] R. Finkelstein, R. B.-S. Tsai, X. Sun, P. Scholl, S. Direkci, T. Gefen, J. Choi, A. L. Shaw, and M. Endres, *Universal quantum operations and ancilla-based readout for tweezer clocks*, arXiv:2402.16220 (see p. 2).

[64] T. Xia, M. Lichtman, K. Maller, A. W. Carr, M. J. Piotrowicz, L. Isenhower, and M. Saffman, *Randomized Benchmarking of Single-Qubit Gates in a 2D Array of Neutral-Atom Qubits*, Phys. Rev. Lett. **114**, 100503 (2015) (see p. 2).

[65] K. M. Maller, M. T. Lichtman, T. Xia, Y. Sun, M. J. Piotrowicz, A. W. Carr, L. Isenhower, and M. Saffman, *Rydberg-blockade controlled-not gate and entanglement in a two-dimensional array of neutral-atom qubits*, Phys. Rev. A **92**, 022336 (2015) (see p. 2).

[66] A. Jenkins, J. W. Lis, A. Senoo, W. F. McGrew, and A. M. Kaufman, *Ytterbium Nuclear-Spin Qubits in an Optical Tweezer Array*, Phys. Rev. X **12**, 021027 (2022) (see pp. 2, 8, 44, 48, 57, 62, 73).

[67] S. Ma, A. P. Burgers, G. Liu, J. Wilson, B. Zhang, and J. D. Thompson, *Universal Gate Operations on Nuclear Spin Qubits in an Optical Tweezer Array of* ^{171}Yb *Atoms*, Phys. Rev. X **12**, 021028 (2022) (see pp. 2, 8, 12).

[68] Y. Wu, S. Kolkowitz, S. Puri, and J. D. Thompson, *Erasure conversion for fault-tolerant quantum computing in alkaline earth Rydberg atom arrays*, Nature Communications **13**, 4657 (2022) (see p. 2).

[69] T. M. Graham et al., *Multi-qubit entanglement and algorithms on a neutral-atom quantum computer*, Nature **604**, 457 (2022) (see p. 2).

[70] K. Barnes et al., *Assembly and coherent control of a register of nuclear spin qubits*, Nature Communications **13**, 2779 (2022) (see pp. 2, 8).

[71] W. Huie, L. Li, N. Chen, X. Hu, Z. Jia, W. K. C. Sun, and J. P. Covey, *Repetitive Readout and Real-Time Control of Nuclear Spin Qubits in* ^{171}Yb *Atoms*, PRX Quantum **4**, 030337 (2023) (see pp. 2, 8, 12).

[72] K. Singh, C. E. Bradley, S. Anand, V. Ramesh, R. White, and H. Bernien, *Mid-circuit correction of correlated phase errors using an array of spectator qubits*, Science **380**, 1265 (2023) (see p. 2).

[73] D. Bluvstein et al., *Logical quantum processor based on reconfigurable atom arrays*, Nature **626**, 58 (2024) (see pp. 2, 13).

[74] H. J. Manetsch, G. Nomura, E. Bataille, K. H. Leung, X. Lv, and M. Endres, *A tweezer array with 6100 highly coherent atomic qubits*, arXiv:2403.12021 (see pp. 2, 13).

[75] S. Saskin, J. T. Wilson, B. Grinkemeyer, and J. D. Thompson, *Narrow-Line Cooling and Imaging of Ytterbium Atoms in an Optical Tweezer Array*, Phys. Rev. Lett. **122**, 143002 (2019) (see p. 2).

[76] C. Robens, J. Zopes, W. Alt, S. Brakhane, D. Meschede, and A. Alberti, *Low-Entropy States of Neutral Atoms in Polarization-Synthesized Optical Lattices*, Phys. Rev. Lett. **118**, 065302 (2017) (see pp. 2, 64).

[77] B. Yang, H. Sun, C.-J. Huang, H.-Y. Wang, Y. Deng, H.-N. Dai, Z.-S. Yuan, and J.-W. Pan, *Cooling and entangling ultracold atoms in optical lattices*, Science **369**, 550 (2020) (see pp. 2, 64).

[78] H. Sun, B. Yang, H.-Y. Wang, Z.-Y. Zhou, G.-X. Su, H.-N. Dai, Z.-S. Yuan, and J.-W. Pan, *Realization of a bosonic antiferromagnet*, Nat. Phys. **17**, 990 (2021) (see pp. 2, 64).

[79] S. Trotzky, P. Cheinet, S. Fölling, M. Feld, U. Schnorrberger, A. M. Rey, A. Polkovnikov, E. A. Demler, M. D. Lukin, and I. Bloch, *Time-Resolved Observation and Control of Superexchange Interactions with Ultracold Atoms in Optical Lattices*, Science **319**, 295 (2008) (see p. 2).

[80] C. Weitenberg, M. Endres, J. F. Sherson, M. Cheneau, P. Schauß, T. Fukuhara, I. Bloch, and S. Kuhr, *Single-spin addressing in an atomic Mott insulator*, Nature **471**, 319 (2011) (see pp. 2, 64).

[81] S. Nascimbène, Y.-A. Chen, M. Atala, M. Aidelsburger, S. Trotzky, B. Paredes, and I. Bloch, *Experimental Realization of Plaquette Resonating Valence-Bond States with Ultracold Atoms in Optical Superlattices*, Phys. Rev. Lett. **108**, 205301 (2012) (see p. 2).

[82] T. Fukuhara, A. Kantian, M. Endres, M. Cheneau, P. Schauß, S. Hild, D. Bellem, U. Schollwöck, T. Giamarchi, C. Gross, I. Bloch, and S. Kuhr, *Quantum dynamics of a mobile spin impurity*, Nat. Phys. **9**, 235 (2013) (see pp. 2, 64).

[83] H.-N. Dai, B. Yang, A. Reingruber, H. Sun, X.-F. Xu, Y.-A. Chen, Z.-S. Yuan, and J.-W. Pan, *Four-body ring-exchange interactions and anyonic statistics within a minimal toric-code Hamiltonian*, Nat. Phys. **13**, 1195 (2017) (see pp. 2, 64, 80).

[84] L. Krinner, M. Stewart, A. Pazmiño, J. Kwon, and D. Schneble, *Spontaneous emission of matter waves from a tunable open quantum system*, Nature **559**, 589 (2018) (see pp. 2, 64).

[85] O. Mandel, M. Greiner, A. Widera, T. Rom, T. W. Hänsch, and I. Bloch, *Controlled collisions for multi-particle entanglement of optically trapped atoms*, Nature **425**, 937 (2003) (see pp. 2, 64).

[86] H. Labuhn, S. Ravets, D. Barredo, L. Béguin, F. Nogrette, T. Lahaye, and A. Browaeys, *Single-atom addressing in microtraps for quantum-state engineering using Rydberg atoms*, Phys. Rev. A **90**, 023415 (2014) (see pp. 2, 64).

[87] H. Levine, A. Keesling, G. Semeghini, A. Omran, T. T. Wang, S. Ebadi, H. Bernien, M. Greiner, V. Vuleti ć, H. Pichler, and M. D. Lukin, *Parallel Implementation of High-Fidelity Multiqubit Gates with Neutral Atoms*, Phys. Rev. Lett. **123**, 170503 (2019) (see pp. 2, 64).

[88] W.-Y. Zhang et al., *Scalable Multipartite Entanglement Created by Spin Exchange in an Optical Lattice*, Phys. Rev. Lett. **131**, 073401 (2023) (see pp. 2, 64).

[89] Z.-Y. Zhou, G.-X. Su, J. C. Halimeh, R. Ott, H. Sun, P. Hauke, B. Yang, Z.-S. Yuan, J. Berges, and J.-W. Pan, *Thermalization dynamics of a gauge theory on a quantum simulator*, Science **377**, 311 (2022) (see pp. 3, 88).

[90] H.-Y. Wang, W.-Y. Zhang, Z. Yao, Y. Liu, Z.-H. Zhu, Y.-G. Zheng, X.-K. Wang, H. Zhai, Z.-S. Yuan, and J.-W. Pan, *Interrelated Thermalization and Quantum Criticality in a Lattice Gauge Simulator*, Phys. Rev. Lett. **131**, 050401 (2023) (see pp. 3, 88).

[91] A. Heinz, A. J. Park, N. Šanti ć, J. Trautmann, S. G. Porsev, M. S. Safronova, I. Bloch, and S. Blatt, *State-Dependent Optical Lattices for the Strontium Optical Qubit*, Phys. Rev. Lett. **124**, 203201 (2020) (see pp. 3, 12, 64, 67, 87).

[92] F. M. Surace, P. Fromholz, N. D. Oppong, M. Dalmonte, and M. Aidelsburger, *Ab Initio Derivation of Lattice-Gauge-Theory Dynamics for Cold Gases in Optical Lattices*, PRX Quantum **4**, 020330 (2023) (see pp. 3, 75, 81, 82, 84, 85, 88).

[93] T. O. Höhn*, E. Staub*, G. Brochier, N. Darkwah Oppong, and M. Aidelsburger, *State-dependent potentials for the $^1S_0$ and $^3P_0$ clock states of neutral ytterbium atoms*, Phys. Rev. A **108**, 053325 (2023) (see pp. 5, 12, 64, 66, 69–71).

[94] J. R. de Laeter, J. K. Böhlke, P. D. Bièvre, H. Hidaka, H. S. Peiser, K. J. R. Rosman, and P. D. P. Taylor, *Atomic weights of the elements. Review 2000 (IUPAC Technical Report)*, Pure and Applied Chemistry **75**, 683 (2003) (see p. 6).

[95] S. Sugawa, R. Yamazaki, S. Taie, and Y. Takahashi, *Bose-Einstein condensate in gases of rare atomic species*, Phys. Rev. A **84**, 011610 (2011) (see p. 6).

[96] S. Sugawa, K. Inaba, S. Taie, R. Yamazaki, M. Yamashita, and Y. Takahashi, *Interaction and filling-induced quantum phases of dual Mott insulators of bosons and fermions*, Nat. Phys. **7**, 642 (2011) (see p. 6).

[97] B. Abeln, K. Sponselee, M. Diem, N. Pintul, K. Sengstock, and C. Becker, *Interorbital interactions in an* SU(2) $\bigotimes$ SU(6)*-symmetric Fermi-Fermi mixture*, Phys. Rev. A **103**, 033315 (2021) (see p. 6).

[98] Y. Takasu, K. Komori, K. Honda, M. Kumakura, T. Yabuzaki, and Y. Takahashi, *Photoassociation Spectroscopy of Laser-Cooled Ytterbium Atoms*, Phys. Rev. Lett. **93**, 123202 (2004) (see pp. 7, 73).

[99] K. Pandey, A. K. Singh, P. V. K. Kumar, M. V. Suryanarayana, and V. Natarajan, *Isotope shifts and hyperfine structure in the 555.8-nm $^1S_0 \rightarrow {}^3P_1$ line of Yb*, Phys. Rev. A **80**, 022518 (2009) (see pp. 7, 93).

[100] S. G. Porsev and A. Derevianko, *Hyperfine quenching of the metastable $^3P_{0,2}$ states in divalent atoms*, Phys. Rev. A **69**, 042506 (2004) (see pp. 7, 8).

[101] J. W. Cho, H.-g. Lee, S. Lee, J. Ahn, W.-K. Lee, D.-H. Yu, S. K. Lee, and C. Y. Park, *Optical repumping of triplet-P states enhances magneto-optical trapping of ytterbium atoms*, Phys. Rev. A **85**, 035401 (2012) (see pp. 7, 8).

[102] J. E. Sansonetti and W. C. Martin, *Handbook of Basic Atomic Spectroscopic Data*, Journal of Physical and Chemical Reference Data **34**, 1559 (2005) (see p. 7).

[103] C. J. Foot, *Atomic Physics* (Oxford University Press, Oxford, 2005) (see p. 7).

[104] K. Blagoev and V. Komarovskii, *Lifetimes of Levels of Neutral and Singly Ionized Lanthanide Atoms*, Atomic Data and Nuclear Data Tables **56**, 1 (1994) (see pp. 7, 72, 73).

[105] N. Hinkley, J. A. Sherman, N. B. Phillips, M. Schioppo, N. D. Lemke, K. Beloy, M. Pizzocaro, C. W. Oates, and A. D. Ludlow, *An Atomic Clock with* 10^{-18} *Instability*, Science **341**, 1215 (2013) (see p. 8).

[106] M. Schioppo, R. C. Brown, W. F. McGrew, N. Hinkley, R. J. Fasano, K. Beloy, T. H. Yoon, G. Milani, D. Nicolodi, J. A. Sherman, N. B. Phillips, C. W. Oates, and A. D. Ludlow, *Ultrastable optical clock with two cold-atom ensembles*, Nature Photonics **11**, 48 (2017) (see p. 8).

[107] W. F. McGrew, X. Zhang, R. J. Fasano, S. A. Schäffer, K. Beloy, D. Nicolodi, R. C. Brown, N. Hinkley, G. Milani, M. Schioppo, T. H. Yoon, and A. D. Ludlow, *Atomic clock performance enabling geodesy below the centimetre level*, Nature **564**, 87 (2018) (see p. 8).

[108] S. Kato, S. Sugawa, K. Shibata, R. Yamamoto, and Y. Takahashi, *Control of Resonant Interaction between Electronic Ground and Excited States*, Phys. Rev. Lett. **110**, 173201 (2013) (see p. 8).

[109] S. Kato, K. Shibata, R. Yamamoto, Y. Yoshikawa, and Y. Takahashi, *Optical magnetic resonance imaging with an ultra-narrow optical transition*, Applied Physics B **108**, 31 (2012) (see p. 8).

[110] K. Shibata, R. Yamamoto, Y. Seki, and Y. Takahashi, *Optical spectral imaging of a single layer of a quantum gas with an ultranarrow optical transition*, Phys. Rev. A **89**, 031601 (2014) (see p. 8).

[111] A. Yamaguchi, S. Uetake, S. Kato, H. Ito, and Y. Takahashi, *High-resolution laser spectroscopy of a Bose–Einstein condensate using the ultranarrow magnetic quadrupole transition*, New Journal of Physics **12**, 103001 (2010) (see p. 8).

[112] O. Onishchenko, S. Pyatchenkov, A. Urech, C.-C. Chen, S. Bennetts, G. A. Siviloglou, and F. Schreck, *Frequency of the ultranarrow* $^1S_0 - ^3P_2$ *transition in* ^{87}Sr, Phys. Rev. A **99**, 052503 (2019) (see p. 8).

[113] J. Trautmann, D. Yankelev, V. Klüsener, A. J. Park, I. Bloch, and S. Blatt, $^1S_0 - ^3P_2$ *magnetic quadrupole transition in neutral strontium*, Phys. Rev. Res. **5**, 013219 (2023) (see p. 8).

[114] A. Pagano, S. Weber, D. Jaschke, T. Pfau, F. Meinert, S. Montangero, and H. P. Büchler, *Error budgeting for a controlled-phase gate with strontium-88 Rydberg atoms*, Phys. Rev. Res. **4**, 033019 (2022) (see p. 8).

[115] G. Unnikrishnan, P. Ilzhöfer, A. Scholz, C. Hölzl, A. Götzelmann, R. K. Gupta, J. Zhao, J. Krauter, S. Weber, N. Makki, H. P. Büchler, T. Pfau, and F. Meiner, *Coherent Control of the Fine-Structure Qubit in a Single Alkaline-Earth Atom*, arXiv:2401.10679 (see p. 8).

[116] S. Pucher, V. Klüsener, F. Spriestersbach, J. Geiger, A. Schindewolf, I. Bloch, and S. Blatt, *Fine-Structure Qubit Encoded in Metastable Strontium Trapped in an Optical Lattice*, arXiv:2401.11054 (see p. 8).

[117] S. G. Porsev, Y. G. Rakhlina, and M. G. Kozlov, *Electric-dipole amplitudes, lifetimes, and polarizabilities of the low-lying levels of atomic ytterbium*, Phys. Rev. A **60**, 2781 (1999) (see p. 8).

[118] M. Foss-Feig, M. Hermele, V. Gurarie, and A. M. Rey, *Heavy fermions in an optical lattice*, Phys. Rev. A **82**, 053624 (2010) (see p. 9).

[119] A. V. Gorshkov, M. Hermele, V. Gurarie, C. Xu, P. S. Julienne, J. Ye, P. Zoller, E. Demler, M. D. Lukin, and A. M. Rey, *Two-orbital SU(N) magnetism with ultracold alkaline-earth atoms*, Nat. Phys. **6**, 289 (2010) (see p. 9).

[120] S. Stellmer, R. Grimm, and F. Schreck, *Detection and manipulation of nuclear spin states in fermionic strontium*, Phys. Rev. A **84**, 043611 (2011) (see p. 9).

[121] S. Taie, R. Yamazaki, S. Sugawa, and Y. Takahashi, *An SU(6) Mott insulator of an atomic Fermi gas realized by large-spin Pomeranchuk cooling*, Nat. Phys. **8**, 825 (2012) (see p. 9).

[122] F. Scazza, C. Hofrichter, M. Höfer, P. C. De Groot, I. Bloch, and S. Fölling, *Observation of two-orbital spin-exchange interactions with ultracold SU(N)-symmetric fermions*, Nat. Phys. **10**, 779 (2014) (see p. 9).

[123] C. Hofrichter, L. Riegger, F. Scazza, M. Höfer, D. R. Fernandes, I. Bloch, and S. Fölling, *Direct Probing of the Mott Crossover in the* SU(N) *Fermi-Hubbard Model*, Phys. Rev. X **6**, 021030 (2016) (see p. 9).

[124] R. Kubo, *The fluctuation-dissipation theorem*, Reports on Progress in Physics **29**, 255 (1966) (see p. 10).

[125] D. A. Steck, *Quantum and Atom Optics*, available online at http://steck.us/teaching (revision 0.15, 21 February 2024) (see pp. 10, 60, 72).

[126] N. Manakov, V. Ovsiannikov, and L. Rapoport, *Atoms in a laser field*, Physics Reports **141**, 320 (1986) (see p. 10).

[127] F. Le Kien, P. Schneeweiss, and A. Rauschenbeutel, *Dynamical polarizability of atoms in arbitrary light fields: general theory and application to cesium*, The European Physical Journal D **67**, 92 (2013) (see p. 10).

[128] V. A. Dzuba and A. Derevianko, *Dynamic polarizabilities and related properties of clock states of the ytterbium atom*, Journal of Physics B: Atomic, Molecular and Optical Physics **43**, 074011 (2010) (see p. 11).

[129] T. Ido and H. Katori, *Recoil-Free Spectroscopy of Neutral Sr Atoms in the Lamb-Dicke Regime*, Phys. Rev. Lett. **91**, 053001 (2003) (see p. 11).

[130] M. Takamoto and H. Katori, *Spectroscopy of the* $^1S_0$–$^3P_0$ *Clock Transition of* ^{87}Sr *in an Optical Lattice*, Phys. Rev. Lett. **91**, 223001 (2003) (see p. 11).

[131] M. Takamoto, F.-L. Hong, R. Higashi, and H. Katori, *An optical lattice clock*, Nature **435**, 321 (2005) (see p. 11).

[132] A. D. Ludlow, M. M. Boyd, T. Zelevinsky, S. M. Foreman, S. Blatt, M. Notcutt, T. Ido, and J. Ye, *Systematic Study of the* ^{87}Sr *Clock Transition in an Optical Lattice*, Phys. Rev. Lett. **96**, 033003 (2006) (see p. 11).

[133] R. Le Targat, X. Baillard, M. Fouché, A. Brusch, O. Tcherbakoff, G. D. Rovera, and P. Lemonde, *Accurate Optical Lattice Clock with* ^{87}Sr *Atoms*, Phys. Rev. Lett. **97**, 130801 (2006) (see p. 11).

[134] J. Ye, H. J. Kimble, and H. Katori, *Quantum State Engineering and Precision Metrology Using State-Insensitive Light Traps*, Science **320**, 1734 (2008) (see p. 11).

[135] Z. W. Barber, J. E. Stalnaker, N. D. Lemke, N. Poli, C. W. Oates, T. M. Fortier, S. A. Diddams, L. Hollberg, C. W. Hoyt, A. V. Taichenachev, and V. I. Yudin, *Optical Lattice Induced Light Shifts in an Yb Atomic Clock*, Phys. Rev. Lett. **100**, 103002 (2008) (see pp. 11, 12, 65, 71, 73).

[136] N. D. Lemke, A. D. Ludlow, Z. W. Barber, T. M. Fortier, S. A. Diddams, Y. Jiang, S. R. Jefferts, T. P. Heavner, T. E. Parker, and C. W. Oates, *Spin-1/2 Optical Lattice Clock*, Phys. Rev. Lett. **103**, 063001 (2009) (see pp. 11, 12).

[137] R. C. Brown, N. B. Phillips, K. Beloy, W. F. McGrew, M. Schioppo, R. J. Fasano, G. Milani, X. Zhang, N. Hinkley, H. Leopardi, T. H. Yoon, D. Nicolodi, T. M. Fortier, and A. D. Ludlow, *Hyperpolarizability and Operational Magic Wavelength in an Optical Lattice Clock*, Phys. Rev. Lett. **119**, 253001 (2017) (see p. 12).

[138] J. W. Lis, A. Senoo, W. F. McGrew, F. Rönchen, A. Jenkins, and A. M. Kaufman, *Midcircuit Operations Using the omg Architecture in Neutral Atom Arrays*, Phys. Rev. X **13**, 041035 (2023) (see pp. 12, 84).

[139] M. A. Norcia et al., *Midcircuit Qubit Measurement and Rearrangement in a* ^{171}Yb *Atomic Array*, Phys. Rev. X **13**, 041034 (2023) (see pp. 12, 65).

[140] W. Yi, A. J. Daley, G. Pupillo, and P. Zoller, *State-dependent, addressable subwavelength lattices with cold atoms*, New Journal of Physics **10**, 073015 (2008) (see p. 12).

[141] F. Gerbier and J. Dalibard, *Gauge fields for ultracold atoms in optical superlattices*, New Journal of Physics **12**, 033007 (2010) (see pp. 12, 87).

[142] L. J. LeBlanc and J. H. Thywissen, *Species-specific optical lattices*, Phys. Rev. A **75**, 053612 (2007) (see pp. 12, 64).

[143] B. Arora, M. S. Safronova, and C. W. Clark, *Tune-out wavelengths of alkali-metal atoms and their applications*, Phys. Rev. A **84**, 043401 (2011) (see p. 12).

[144] Y. Cheng, J. Jiang, and J. Mitroy, *Tune-out wavelengths for the alkaline-earth-metal atoms*, Phys. Rev. A **88**, 022511 (2013) (see p. 12).

[145] C. D. Herold, V. D. Vaidya, X. Li, S. L. Rolston, J. V. Porto, and M. S. Safronova, *Precision Measurement of Transition Matrix Elements via Light Shift Cancellation*, Phys. Rev. Lett. **109**, 243003 (2012) (see p. 12).

[146] F. Schmidt, D. Mayer, M. Hohmann, T. Lausch, F. Kindermann, and A. Widera, *Precision measurement of the* ^{87}*Rb tune-out wavelength in the hyperfine ground state* $F = 1$ *at 790 nm*, Phys. Rev. A **93**, 022507 (2016) (see p. 12).

[147] A. Ratkata, P. D. Gregory, A. D. Innes, J. A. Matthies, L. A. McArd, J. M. Mortlock, M. S. Safronova, S. L. Bromley, and S. L. Cornish, *Measurement of the tune-out wavelength for* ^{133}Cs *at 880 nm*, Phys. Rev. A **104**, 052813 (2021) (see p. 12).

[148] R. H. Leonard, A. J. Fallon, C. A. Sackett, and M. S. Safronova, *High-precision measurements of the* ^{87}Rb *D-line tune-out wavelength*, Phys. Rev. A **92**, 052501 (2015) (see pp. 12, 64).

[149] W. F. Holmgren, R. Trubko, I. Hromada, and A. D. Cronin, *Measurement of a Wavelength of Light for Which the Energy Shift for an Atom Vanishes*, Phys. Rev. Lett. **109**, 243004 (2012) (see p. 12).

[150] B. M. Henson, R. I. Khakimov, R. G. Dall, K. G. H. Baldwin, L.-Y. Tang, and A. G. Truscott, *Precision Measurement for Metastable Helium Atoms of the 413 nm Tune-Out Wavelength at Which the Atomic Polarizability Vanishes*, Phys. Rev. Lett. **115**, 043004 (2015) (see p. 12).

[151] B. M. Henson, J. A. Ross, K. F. Thomas, C. N. Kuhn, D. K. Shin, S. S. Hodgman, Y.-H. Zhang, L.-Y. Tang, G. W. F. Drake, A. T. Bondy, A. G. Truscott, and K. G. H. Baldwin, *Measurement of a helium tune-out frequency: an independent test of quantum electrodynamics*, Science **376**, 199 (2022) (see p. 12).

[152] I. M. Georgescu, S. Ashhab, and F. Nori, *Quantum simulation*, Rev. Mod. Phys. **86**, 153 (2014) (see p. 12).

[153] A. J. Daley, M. M. Boyd, J. Ye, and P. Zoller, *Quantum Computing with Alkaline-Earth-Metal Atoms*, Phys. Rev. Lett. **101**, 170504 (2008) (see pp. 12, 64, 87).

[154] L. Henriet, L. Beguin, A. Signoles, T. Lahaye, A. Browaeys, G.-O. Reymond, and C. Jurczak, *Quantum computing with neutral atoms*, Quantum **4**, 327 (2020) (see p. 12).

[155] R. Bause, M. Li, A. Schindewolf, X.-Y. Chen, M. Duda, S. Kotochigova, I. Bloch, and X.-Y. Luo, *Tune-Out and Magic Wavelengths for Ground-State* ^{23}Na^{40}K *Molecules*, Phys. Rev. Lett. **125**, 023201 (2020) (see p. 12).

[156] A. M. Kaufman, B. J. Lester, and C. A. Regal, *Cooling a Single Atom in an Optical Tweezer to Its Quantum Ground State*, Phys. Rev. X **2**, 041014 (2012) (see p. 13).

[157] J. D. Thompson, T. G. Tiecke, A. S. Zibrov, V. Vuleti ć, and M. D. Lukin, *Coherence and Raman Sideband Cooling of a Single Atom in an Optical Tweezer*, Phys. Rev. Lett. **110**, 133001 (2013) (see p. 13).

[158] B. Zhang, P. Peng, A. Paul, and J. D. Thompson, *Scaled local gate controller for optically addressed qubits*, Optica **11**, 227 (2024) (see p. 13).

[159] H. Bernien, S. Schwartz, A. Keesling, H. Levine, A. Omran, H. Pichler, S. Choi, A. S. Zibrov, M. Endres, M. Greiner, V. Vuletić, and M. D. Lukin, *Probing many-body dynamics on a 51-atom quantum simulator*, Nature **551**, 579 (2017) (see p. 13).

[160] S. J. Evered, D. Bluvstein, M. Kalinowski, S. Ebadi, T. Manovitz, H. Zhou, S. H. Li, A. A. Geim, T. T. Wang, N. Maskara, H. Levine, G. Semeghini, M. Greiner, V. Vuletić, and M. D. Lukin, *High-fidelity parallel entangling gates on a neutral-atom quantum computer*, Nature **622**, 268 (2023) (see p. 13).

[161] S. Wilson and M. Hutley, *The Optical Properties of 'Moth Eye' Antireflection Surfaces*, Optica Acta: International Journal of Optics **29**, 993 (1982) (see p. 17).

[162] D. S. Hobbs, B. D. MacLeod, and J. R. Riccobono, *Update on the development of high performance anti-reflecting surface relief micro-structures*, in Window and dome technologies and materials x, Vol. 6545, edited by R. W. Tustison (International Society for Optics and Photonics, May 2007), 65450Y (see p. 17).

[163] S. Arrhenius, *Über die Dissociationswärme und den Einfluss der Temperatur auf den Dissociationsgrad der Elektrolyte*, Zeitschrift für Physikalische Chemie **4**, 96 (1889) (see p. 19).

[164] M. Li and H. F. Dylla, *Model for the outgassing of water from metal surfaces*, Journal of Vacuum Science & Technology A **11**, 1702 (1993) (see p. 19).

[165] A. Fick, *Ueber Diffusion*, Annalen der Physik **170**, 59 (1855) (see p. 19).

[166] K. Jousten, *Handbuch Vakuumtechnik*, edited by K. Jousten, 12th ed., Springer Reference Technik (Springer Vieweg, Wiesbaden, 2018) (see pp. 19, 20).

[167] J. Crank and P. Nicolson, *A practical method for numerical evaluation of solutions of partial differential equations of the heat-conduction type*, Mathematical Proceedings of the Cambridge Philosophical Society **43**, 50 (1947) (see p. 20).

[168] D. Grant, D. Cummings, and D. Blackburn, *Hydrogen in 316 steel — diffusion, permeation and surface reaction*, Journal of Nuclear Materials **152**, 139 (1988) (see p. 20).

[169] J. A. Fedchak, J. K. Scherschligt, S. Avdiaj, D. S. Barker, S. P. Eckel, B. Bowers, S. O'Connell, and P. Henderson, *Outgassing rate comparison of seven geometrically similar vacuum chambers of different materials and heat treatments*, Journal of Vacuum Science & Technology B **39**, 024201 (2021) (see p. 20).

[170] D. S. Barker, B. P. Acharya, J. A. Fedchak, N. N. Klimov, E. B. Norrgard, J. Scherschligt, E. Tiesinga, and S. P. Eckel, *Precise quantum measurement of vacuum with cold atoms*, Review of Scientific Instruments **93**, 121101 (2022) (see p. 20).

[171] R. Grinham and A. Chew, *A Review of Outgassing and Methods for its Reduction*, Applied Science and Convergence Technology **26**, 95 (2017) (see p. 20).

[172] T. Bergeman, G. Erez, and H. J. Metcalf, *Magnetostatic trapping fields for neutral atoms*, Phys. Rev. A **35**, 1535 (1987) (see p. 25).

[173] A. Thabuis, X. Ren, T. Duong, and Y. Perriard, *Exploring Beyond the Helmholtz Coils for Uniform Magnetic Field Generation With Topology Optimization*, IEEE Transactions on Magnetics **58**, 1 (2022) (see p. 25).

[174] N. Poli, Z. W. Barber, N. D. Lemke, C. W. Oates, L. S. Ma, J. E. Stalnaker, T. M. Fortier, S. A. Diddams, L. Hollberg, J. C. Bergquist, A. Brusch, S. Jefferts, T. Heavner, and T. Parker, *Frequency evaluation of the doubly forbidden* $^1S_0 \rightarrow {}^3P_0$ *transition in bosonic* ^{174}Yb, Phys. Rev. A **77**, 050501 (2008) (see pp. 25, 61).

[175] H. Wheeler, *Simple Inductance Formulas for Radio Coils*, Proceedings of the Institute of Radio Engineers **16**, 1398 (1928) (see p. 26).

[176] P. Horowitz and W. Hill, *The Art of Electronics*, 3rd ed. (Cambridge University Press, Cambridge, 2015) (see p. 27).

[177] N. D. Lemke, *Optical Lattice Clock with Spin-1/2 Ytterbium Atoms*, Ph.D. thesis, University of Colorado (2012).

[178] T. A. Savard, K. M. O'Hara, and J. E. Thomas, *Laser-noise-induced heating in far-off resonance optical traps*, Phys. Rev. A **56**, R1095 (1997) (see pp. 33, 68).

[179] R. W. P. Drever, J. L. Hall, F. V. Kowalski, J. Hough, G. M. Ford, A. J. Munley, and H. Ward, *Laser phase and frequency stabilization using an optical resonator*, Appl. Phys. B **31**, 97 (1983) (see p. 34).

[180] E. D. Black, *An introduction to Pound–Drever–Hall laser frequency stabilization*, American Journal of Physics **69**, 79 (2001) (see pp. 34, 39).

[181] J. I. Thorpe, K. Numata, and J. Livas, *Laser frequency stabilization and control through offset sideband locking to optical cavities*, Opt. Express **16**, 15980 (2008) (see pp. 34, 40).

[182] N. Hodgson and H. Weber, *Laser Resonators and Beam Propagation*, 2nd ed. (Springer, Berlin, 2005) (see p. 35).

[183] M. J. Martin, *Quantum Metrology and Many-Body Physics: Pushing the Frontier of the Optical Lattice Clock*, Ph.D. thesis, University of Colorado (2013).

[184] D. R. Huber and J. B. Carroll, *Time domain response of an optically frequency swept Fabry-Perot interferometer*, Appl. Opt. **25**, 2386 (1986) (see p. 36).

[185] G. Brochier, *Measures of the magic & tune-out wavelengths of cold Ytterbium atoms*, Semester report, Ludwig-Maximilians-Universität (2022).

[186] T. Legero, T. Kessler, and U. Sterr, *Tuning the thermal expansion properties of optical reference cavities with fused silica mirrors*, J. Opt. Soc. Am. B **27**, 914 (2010) (see pp. 37, 38).

[187] E. Hecht, *Optics*, 5th ed. (Pearson, London, 2017) (see p. 41).

[188] M. Born and E. Wolf, *Principles of Optics*, 7th ed. (Cambridge University Press, Cambridge, 1999) (see p. 42).

[189] D. Gröters, *Diffraction-limited Imaging and Trapping of Ultracold Ytterbium Atoms in Optical Tweezer Arrays*, M.Sc. thesis, 2023 (see pp. 42, 43, 62).

[190] N. Darkwah Oppong, *Towards a degenerate Fermi gas of strontium-87 in a 3D optical lattice*, M.Sc. thesis, 2015 (see p. 44).

[191] A. Impertro, *Preparation and Study of 1D and 2D Many-Body Systems with Fermionic Ytterbium*, M.Sc. thesis, 2020 (see p. 46).

[192] B. Plotkin-Swing, A. Wirth, D. Gochnauer, T. Rahman, K. E. McAlpine, and S. Gupta, *Crossed-beam slowing to enhance narrow-line ytterbium magneto-optic traps*, Review of Scientific Instruments **91**, 093201 (2020) (see pp. 47, 54).

[193] M. Fox, *Optical properties of solids*, 2nd ed., Oxford master series in physics ; 3. Condensed matter physics (Oxford University Press, Oxford, 2010) (see p. 50).

[194] G. Reinaudi, T. Lahaye, Z. Wang, and D. Guéry-Odelin, *Strong saturation absorption imaging of dense clouds of ultracold atoms*, Opt. Lett. **32**, 3143 (2007) (see p. 51).

[195] K. Hueck, N. Luick, L. Sobirey, J. Siegl, T. Lompe, H. Moritz, L. W. Clark, and C. Chin, *Calibrating high intensity absorption imaging of ultracold atoms*, Opt. Express **25**, 8670 (2017) (see p. 51).

[196] D. Guéry-Odelin, J. Söding, P. Desbiolles, and J. Dalibard, *Strong evaporative cooling of a trapped cesium gas*, Opt. Express **2**, 323 (1998) (see p. 52).

[197] E. L. Raab, M. Prentiss, A. Cable, S. Chu, and D. E. Pritchard, *Trapping of Neutral Sodium Atoms with Radiation Pressure*, Phys. Rev. Lett. **59**, 2631 (1987) (see p. 53).

[198] H. J. Metcalf and P. Straten, *Laser Cooling and Trapping* (Springer New York, New York, 2012) (see pp. 53–55).

[199] A. M. Steane, M. Chowdhury, and C. J. Foot, *Radiation force in the magneto-optical trap*, J. Opt. Soc. Am. B **9**, 2142 (1992) (see p. 55).

[200] W. Petrich, M. H. Anderson, J. R. Ensher, and E. A. Cornell, *Behavior of atoms in a compressed magneto-optical trap*, J. Opt. Soc. Am. B **11**, 1332 (1994) (see p. 55).

[201] C. G. Townsend, N. H. Edwards, C. J. Cooper, K. P. Zetie, C. J. Foot, A. M. Steane, P. Szriftgiser, H. Perrin, and J. Dalibard, *Phase-space density in the magneto-optical trap*, Phys. Rev. A **52**, 1423 (1995) (see p. 55).

[202] S. N. Lea, *Limits to time variation of fundamental constants from comparisons of atomic frequency standards*, Reports on Progress in Physics **70**, 1473 (2007) (see p. 55).

[203] X. Zhang, K. Beloy, Y. S. Hassan, W. F. McGrew, C.-C. Chen, J. L. Siegel, T. Grogan, and A. D. Ludlow, *Subrecoil Clock-Transition Laser Cooling Enabling Shallow Optical Lattice Clocks*, Phys. Rev. Lett. **129**, 113202 (2022) (see p. 56).

[204] C. Monroe, D. M. Meekhof, B. E. King, S. R. Jefferts, W. M. Itano, D. J. Wineland, and P. Gould, *Resolved-Sideband Raman Cooling of a Bound Atom to the 3D Zero-Point Energy*, Phys. Rev. Lett. **75**, 4011 (1995) (see p. 57).

[205] S. Blatt, J. W. Thomsen, G. K. Campbell, A. D. Ludlow, M. D. Swallows, M. J. Martin, M. M. Boyd, and J. Ye, *Rabi spectroscopy and excitation inhomogeneity in a one-dimensional optical lattice clock*, Phys. Rev. A **80**, 052703 (2009) (see p. 57).

[206] A. V. Taichenachev, V. I. Yudin, C. W. Oates, C. W. Hoyt, Z. W. Barber, and L. Hollberg, *Magnetic Field-Induced Spectroscopy of Forbidden Optical Transitions with Application to Lattice-Based Optical Atomic Clocks*, Phys. Rev. Lett. **96**, 083001 (2006) (see p. 60).

[207] Z. W. Barber, C. W. Hoyt, C. W. Oates, L. Hollberg, A. V. Taichenachev, and V. I. Yudin, *Direct Excitation of the Forbidden Clock Transition in Neutral* ^{174}Yb *Atoms Confined to an Optical Lattice*, Phys. Rev. Lett. **96**, 083002 (2006) (see p. 60).

[208] M. Baumann and G. Wandel, *gJ Factors of the 6s6p 3P1 and 6s6p 1P1 states of ytterbium*, Physics Letters A **28**, 200 (1968) (see pp. 60, 62).

[209] M. M. Boyd, T. Zelevinsky, A. D. Ludlow, S. Blatt, T. Zanon-Willette, S. M. Foreman, and J. Ye, *Nuclear spin effects in optical lattice clocks*, Phys. Rev. A **76**, 022510 (2007) (see p. 61).

[210] A. W. Young, W. J. Eckner, N. Schine, A. M. Childs, and A. M. Kaufman, *Tweezer-programmable 2D quantum walks in a Hubbard-regime lattice*, Science **377**, 885 (2022) (see pp. 62, 84, 88).

[211] K. M. Jones, E. Tiesinga, P. D. Lett, and P. S. Julienne, *Ultracold photoassociation spectroscopy: Long-range molecules and atomic scattering*, Rev. Mod. Phys. **78**, 483 (2006) (see p. 63).

[212] D. González-Cuadra, D. Bluvstein, M. Kalinowski, R. Kaubruegger, N. Maskara, P. Naldesi, T. V. Zache, A. M. Kaufman, M. D. Lukin, H. Pichler, B. Vermersch, J. Ye, and P. Zoller, *Fermionic quantum processing with programmable neutral atom arrays*, Proceedings of the National Academy of Sciences **120**, e2304294120 (2023) (see p. 64).

[213] L. Riegger, N. Darkwah Oppong, M. Höfer, D. R. Fernandes, I. Bloch, and S. Fölling, *Localized Magnetic Moments with Tunable Spin Exchange in a Gas of Ultracold Fermions*, Phys. Rev. Lett. **120**, 143601 (2018) (see p. 64).

[214] N. Darkwah Oppong, G. Pasqualetti, O. Bettermann, P. Zechmann, M. Knap, I. Bloch, and S. Fölling, *Probing Transport and Slow Relaxation in the Mass-Imbalanced Fermi-Hubbard Model*, Phys. Rev. X **12**, 031026 (2022) (see p. 64).

[215] M. E. Gehm, K. M. O'Hara, T. A. Savard, and J. E. Thomas, *Dynamics of noise-induced heating in atom traps*, Phys. Rev. A **58**, 3914 (1998) (see p. 68).

[216] R. Jáuregui, N. Poli, G. Roati, and G. Modugno, *Anharmonic parametric excitation in optical lattices*, Phys. Rev. A **64**, 033403 (2001) (see p. 70).

[217] R. Cowan, *The Theory of Atomic Structure and Spectra*, Los Alamos Series in Basic and Applied Sciences (University of California Press, Berkeley, 1981) (see p. 72).

[218] Yuri Ralchenko, *Atomic Spectroscopy - Different Coupling Schemes*, available online at https://www.nist.gov/pml/atomic-spectroscopy-compendium-basic-ideas-notation-data-and-formulas/atomic-spectroscopy-2 (updated 2023) (see p. 72).

[219] K. Beloy, *Experimental constraints on the polarizabilities of the* $6s^2\ {}^1S_0$ *and* $6s6p\ {}^3P_0^o$ *states of Yb*, Phys. Rev. A **86**, 022521 (2012) (see p. 73).

[220] M. Baumann, M. Braun, A. Gaiser, and H. Liening, *Radiative lifetimes and gJ factors of low-lying even-parity levels in the Yb I spectrum*, Journal of Physics B: Atomic and Molecular Physics **18**, L601 (1985) (see p. 73).

[221] N. D. Lemke, J. von Stecher, J. A. Sherman, A. M. Rey, C. W. Oates, and A. D. Ludlow, *p-Wave Cold Collisions in an Optical Lattice Clock*, Phys. Rev. Lett. **107**, 103902 (2011) (see p. 73).

[222] A. D. Ludlow, N. D. Lemke, J. A. Sherman, C. W. Oates, G. QuÃ©mÃ©ner, J. von Stecher, and A. M. Rey, *Cold-collision-shift cancellation and inelastic scattering in a Yb optical lattice clock*, Phys. Rev. A **84**, 10.1103/physreva.84.052724 (2011) (see p. 73).

[223] A. Rey, A. Gorshkov, C. Kraus, M. Martin, M. Bishof, M. Swallows, X. Zhang, C. Benko, J. Ye, N. Lemke, and A. Ludlow, *Probing many-body interactions in an optical lattice clock*, Annals of Physics **340**, 311 (2014) (see p. 73).

[224] J. L. Siegel, W. F. McGrew, Y. S. Hassan, C.-C. Chen, K. Beloy, T. Grogan, X. Zhang, and A. D. Ludlow, *Excited-Band Coherent Delocalization for Improved Optical Lattice Clock Performance*, Phys. Rev. Lett. **132**, 133201 (2024) (see p. 73).

[225] T. Akatsuka, M. Takamoto, and H. Katori, *Three-dimensional optical lattice clock with bosonic* ^{88}Sr *atoms*, Phys. Rev. A **81**, 023402 (2010) (see p. 73).

[226] S. L. Campbell, R. B. Hutson, G. E. Marti, A. Goban, N. D. Oppong, R. L. McNally, L. Sonderhouse, J. M. Robinson, W. Zhang, B. J. Bloom, and J. Ye, *A Fermi-degenerate three-dimensional optical lattice clock*, Science **358**, 90 (2017) (see p. 73).

[227] L. Riegger, *Interorbital spin exchange in a state-dependent optical lattice*, Ph.D. thesis, University of Munich (2019).

[228] S. Weinberg, *The Quantum Theory of Fields* (Cambridge University Press, Cambridge, 1995) (see p. 75).

[229] M. D. Schwartz, *Quantum Field Theory and the Standard Model* (Cambridge University Press, Cambridge, 2013) (see p. 75).

[230] A. Einstein, *Die Feldgleichungen der Gravitation*, Sitzungsberichte der Königlich Preussischen Akademie der Wissenschaften zu Berlin, 844 (1915) (see p. 75).

[231] A. Einstein, *Erklärung der Perihelbewegung des Merkur aus der allgemeinen Relativitätstheorie*, Sitzungsberichte der Königlich Preussischen Akademie der Wissenschaften zu Berlin, 831 (1915) (see p. 75).

[232] B. P. Abbott et al. (LIGO Scientific Collaboration), *Observation of Gravitational Waves from a Binary Black Hole Merger*, Phys. Rev. Lett. **116**, 061102 (2016) (see p. 75).

[233] K. Akiyama et al. (The Event Horizon Telescope Collaboration), *First M87 Event Horizon Telescope Results. I. The Shadow of the Supermassive Black Hole*, The Astrophysical Journal Letters **875**, L1 (2019) (see p. 75).

[234] T. Maudlin, *Philosophy of Physics: Space and Time* (Princeton University Press, Princeton, 2012) (see p. 75).

[235] G. Belot, *Symmetry and Equivalence*, in *The oxford handbook of philosophy of physics*, edited by R. Batterman (Oxford University Press, 2013), 318 (see p. 75).

[236] C. Rovelli, *Why Gauge?* Foundations of Physics **44**, 91 (2014) (see p. 75).

[237] H. Gomes, B. W. Roberts, and J. Butterfield, *The Gauge Argument: A Noether Reason*, in *The physics and philosophy of noether's theorems*, edited by J. Read and N. J. Teh (Cambridge University Press, 2022), 354 (see p. 75).

[238] J. Kogut and L. Susskind, *Hamiltonian formulation of Wilson's lattice gauge theories*, Phys. Rev. D **11**, 395 (1975) (see pp. 75, 77, 79).

[239] J. B. Kogut, *An introduction to lattice gauge theory and spin systems*, Rev. Mod. Phys. **51**, 659 (1979) (see p. 75).

[240] H. J. Rothe, *Lattice Gauge Theories : An Introduction*, 4th ed., Vol. 43 (World Scientific Publishing Company, Singapore, 2012) (see p. 75).

[241] M. Creutz, L. Jacobs, and C. Rebbi, *Monte Carlo computations in lattice gauge theories*, Physics Reports **95**, 201 (1983) (see p. 75).

[242] J. Bender, P. Emonts, and J. I. Cirac, *Variational Monte Carlo algorithm for lattice gauge theories with continuous gauge groups: A study of* $(2+1)$*-dimensional compact QED with dynamical fermions at finite density*, Phys. Rev. Res. **5**, 043128 (2023) (see p. 75).

[243] M. C. Bañuls, K. Cichy, J. I. Cirac, and K. Jansen, *The mass spectrum of the Schwinger model with matrix product states*, Journal of High Energy Physics **2013**, 158 (2013) (see p. 75).

[244] B. Buyens, J. Haegeman, K. Van Acoleyen, H. Verschelde, and F. Verstraete, *Matrix Product States for Gauge Field Theories*, Phys. Rev. Lett. **113**, 091601 (2014) (see p. 75).

[245] T. Pichler, M. Dalmonte, E. Rico, P. Zoller, and S. Montangero, *Real-Time Dynamics in U(1) Lattice Gauge Theories with Tensor Networks*, Phys. Rev. X **6**, 011023 (2016) (see p. 75).

[246] X.-G. Wen, *Quantum Field Theory of Many-Body Systems: From the Origin of Sound to an Origin of Light and Electrons* (Oxford University Press, Oxford, 2007) (see p. 75).

[247] M. Troyer and U.-J. Wiese, *Computational Complexity and Fundamental Limitations to Fermionic Quantum Monte Carlo Simulations*, Phys. Rev. Lett. **94**, 170201 (2005) (see p. 75).

[248] E. A. Martinez, C. A. Muschik, P. Schindler, D. Nigg, A. Erhard, M. Heyl, P. Hauke, M. Dalmonte, T. Monz, P. Zoller, and R. Blatt, *Real-time dynamics of lattice gauge theories with a few-qubit quantum computer*, Nature **534**, 516 (2016) (see pp. 75, 81).

[249] D. Banerjee, M. Bögli, M. Dalmonte, E. Rico, P. Stebler, U.-J. Wiese, and P. Zoller, *Atomic Quantum Simulation of* $\mathbf{U}(N)$ *and* $\mathrm{SU}(N)$ *Non-Abelian Lattice Gauge Theories*, Phys. Rev. Lett. **110**, 125303 (2013) (see p. 75).

[250] U.-J. Wiese, *Ultracold quantum gases and lattice systems: quantum simulation of lattice gauge theories*, Annalen der Physik **525**, 777 (2013) (see pp. 75, 81).

[251] E. Zohar and M. Burrello, *Formulation of lattice gauge theories for quantum simulations*, Phys. Rev. D **91**, 054506 (2015) (see p. 75).

[252] E. Zohar, J. I. Cirac, and B. Reznik, *Quantum simulations of lattice gauge theories using ultracold atoms in optical lattices*, Reports on Progress in Physics **79**, 014401 (2015) (see p. 75).

[253] T. V. Zache, F. Hebenstreit, F. Jendrzejewski, M. K. Oberthaler, J. Berges, and P. Hauke, *Quantum simulation of lattice gauge theories using Wilson fermions*, Quantum Science and Technology **3**, 034010 (2018) (see p. 75).

[254] J. Bender, E. Zohar, A. Farace, and J. I. Cirac, *Digital quantum simulation of lattice gauge theories in three spatial dimensions*, New Journal of Physics **20**, 093001 (2018) (see p. 75).

[255] F. M. Surace, P. P. Mazza, G. Giudici, A. Lerose, A. Gambassi, and M. Dalmonte, *Lattice Gauge Theories and String Dynamics in Rydberg Atom Quantum Simulators*, Phys. Rev. X **10**, 021041 (2020) (see p. 75).

[256] L. Homeier, C. Schweizer, M. Aidelsburger, A. Fedorov, and F. Grusdt, $\mathbb{Z}_2$ *lattice gauge theories and Kitaev's toric code: A scheme for analog quantum simulation*, Phys. Rev. B **104**, 085138 (2021) (see pp. 75, 80).

[257] E. Zohar, *Quantum simulation of lattice gauge theories in more than one space dimension—requirements, challenges and methods*, Philosophical Transactions of the Royal Society A: Mathematical, Physical and Engineering Sciences **380**, 20210069 (2022) (see p. 75).

[258] L. Homeier, A. Bohrdt, S. Linsel, E. Demler, J. C. Halimeh, and F. Grusdt, *Realistic scheme for quantum simulation of* $\mathbb{Z}_2$ *lattice gauge theories with dynamical matter in (2+1)D*, Communications Physics **6**, 127 (2023) (see p. 75).

[259] G. Pardo, T. Greenberg, A. Fortinsky, N. Katz, and E. Zohar, *Resource-efficient quantum simulation of lattice gauge theories in arbitrary dimensions: Solving for Gauss's law and fermion elimination*, Phys. Rev. Res. **5**, 023077 (2023) (see p. 75).

[260] E. Noether, *Invariante Variationsprobleme*, Nachrichten von der Gesellschaft der Wissenschaften zu Göttingen, Mathematisch-Physikalische Klasse **1918**, 235 (1918) (see p. 76).

[261] E. Fradkin and L. Susskind, *Order and disorder in gauge systems and magnets*, Phys. Rev. D **17**, 2637 (1978) (see p. 76).

[262] H. Nielsen and M. Ninomiya, *A no-go theorem for regularizing chiral fermions*, Physics Letters B **105**, 219 (1981) (see p. 77).

[263] D. B. Kaplan, *Chiral Gauge Theory at the Boundary between Topological Phases*, Phys. Rev. Lett. **132**, 141603 (2024) (see p. 77).

[264] D. B. Kaplan and S. Sen, *Weyl Fermions on a Finite Lattice*, Phys. Rev. Lett. **132**, 141604 (2024) (see p. 77).

[265] R. Loudon, *The Quantum Theory of Light*, 3rd ed. (Oxford University Press, Oxford, 2000) (see p. 79).

[266] S. Sachdev, *Topological order, emergent gauge fields, and Fermi surface reconstruction*, Reports on Progress in Physics **82**, 014001 (2018) (see p. 80).

[267] J. Schwinger, *Gauge Invariance and Mass*, Phys. Rev. **125**, 397 (1962) (see p. 80).

[268] J. Schwinger, *Gauge Invariance and Mass. II*, Phys. Rev. **128**, 2425 (1962) (see p. 80).

[269] S. Coleman, *More about the massive Schwinger model*, Annals of Physics **101**, 239 (1976) (see p. 80).

[270] F. Sauter, *Über das Verhalten eines Elektrons im homogenen elektrischen Feld nach der relativistischen Theorie Diracs*, Zeitschrift für Physik **69**, 742 (1931) (see p. 80).

[271] W. Heisenberg and H. Euler, *Folgerungen aus der Diracschen Theorie des Positrons*, Zeitschrift für Physik **98**, 714 (1936) (see p. 80).

[272] J. Schwinger, *On Gauge Invariance and Vacuum Polarization*, Phys. Rev. **82**, 664 (1951) (see p. 80).

[273] S. Kühn, J. I. Cirac, and M.-C. Bañuls, *Quantum simulation of the Schwinger model: A study of feasibility*, Phys. Rev. A **90**, 042305 (2014) (see p. 80).

[274] S. Chandrasekharan and U.-J. Wiese, *Quantum link models: A discrete approach to gauge theories*, Nuclear Physics B **492**, 455 (1997) (see pp. 80, 81).

[275] B. Yang, H. Sun, R. Ott, H.-Y. Wang, T. V. Zache, J. C. Halimeh, Z.-S. Yuan, P. Hauke, and J.-W. Pan, *Observation of gauge invariance in a 71-site Bose–Hubbard quantum simulator*, Nature **587**, 392 (2020) (see p. 81).

[276] J. C. Halimeh, I. P. McCulloch, B. Yang, and P. Hauke, *Tuning the Topological θ-Angle in Cold-Atom Quantum Simulators of Gauge Theories*, PRX Quantum **3**, 040316 (2022) (see p. 81).

[277] W.-Y. Zhang et al., *Observation of microscopic confinement dynamics by a tunable topological θ-angle*, arXiv:2306.11794 (see p. 81).

[278] C. Schweizer, F. Grusdt, M. Berngruber, L. Barbiero, E. Demler, N. Goldman, I. Bloch, and M. Aidelsburger, *Floquet approach to $\mathbb{Z}_2$ lattice gauge theories with ultracold atoms in optical lattices*, Nat. Phys. **15**, 1168 (2019) (see p. 81).

[279] J. Sebby-Strabley, M. Anderlini, P. S. Jessen, and J. V. Porto, *Lattice of double wells for manipulating pairs of cold atoms*, Phys. Rev. A **73**, 033605 (2006) (see p. 84).

[280] P. T. Brown, D. Mitra, E. Guardado-Sanchez, P. Schauß, S. S. Kondov, E. Khatami, T. Paiva, N. Trivedi, D. A. Huse, and W. S. Bakr, *Spin-imbalance in a 2D Fermi-Hubbard system*, Science **357**, 1385 (2017) (see p. 84).

[281] J. C. Halimeh and P. Hauke, *Reliability of Lattice Gauge Theories*, Phys. Rev. Lett. **125**, 030503 (2020) (see p. 85).

[282] J. C. Halimeh, H. Lang, J. Mildenberger, Z. Jiang, and P. Hauke, *Gauge-Symmetry Protection Using Single-Body Terms*, PRX Quantum **2**, 040311 (2021) (see p. 85).

[283] J. C. Halimeh, L. Homeier, C. Schweizer, M. Aidelsburger, P. Hauke, and F. Grusdt, *Stabilizing lattice gauge theories through simplified local pseudogenerators*, Phys. Rev. Res. **4**, 033120 (2022) (see p. 85).

[284] B. M. Spar, E. Guardado-Sanchez, S. Chi, Z. Z. Yan, and W. S. Bakr, *Realization of a Fermi-Hubbard Optical Tweezer Array*, Phys. Rev. Lett. **128**, 223202 (2022) (see p. 85).

[285] D. Das, S. Barthwal, A. Banerjee, and V. Natarajan, *Absolute frequency measurements in Yb with* 0.08 ppb *uncertainty: Isotope shifts and hyperfine structure in the* 399−nm $^1S_0 \rightarrow ^1P_1$ *line*, Phys. Rev. A **72**, 032506 (2005) (see p. 85).

[286] P. E. Atkinson, J. S. Schelfhout, and J. J. McFerran, *Hyperfine constants and line separations for the* $^1S_0 - ^3P_1$ *intercombination line in neutral ytterbium with sub-Doppler resolution*, Phys. Rev. A **100**, 042505 (2019) (see p. 85).

[287] G. Aad et al. (ATLAS Collaboration), *Observation of a new particle in the search for the Standard Model Higgs boson with the ATLAS detector at the LHC*, Physics Letters B **716**, 1 (2012) (see p. 86).

[288] S. Chatrchyan et al. (CMS Collaboration), *Observation of a new boson at a mass of 125 GeV with the CMS experiment at the LHC*, Physics Letters B **716**, 30 (2012) (see p. 86).

[289] Y. Chai, A. Crippa, K. Jansen, S. Kühn, V. R. Pascuzzi, F. Tacchino, and I. Tavernelli, *Fermionic wave packet scattering: a quantum computing approach*, arXiv:2312.02272 (see p. 86).

[290] G.-X. Su, J. Osborne, and J. C. Halimeh, *A Cold-Atom Particle Collider*, arXiv:2401.05489 (see p. 86).

[291] Z. Davoudi, C.-C. Hsieh, and S. V. Kadam, *Scattering wave packets of hadrons in gauge theories: Preparation on a quantum computer*, arXiv:2402.00840 (see p. 86).

[292] E. R. Bennewitz, B. Ware, A. Schuckert, A. Lerose, F. M. Surace, R. Belyansky, W. Morong, D. Luo, A. De, K. S. Collins, O. Katz, C. Monroe, Z. Davoudi, and A. V. Gorshkov, *Simulating Meson Scattering on Spin Quantum Simulators*, arXiv:2403.07061 (see p. 86).

[293] E. Zohar, J. I. Cirac, and B. Reznik, *Simulating* $(2+1)$*-Dimensional Lattice QED with Dynamical Matter Using Ultracold Atoms*, Phys. Rev. Lett. **110**, 055302 (2013) (see p. 86).

[294] S. Sachdev, *Emergent gauge fields and the high-temperature superconductors*, Philosophical Transactions of the Royal Society A: Mathematical, Physical and Engineering Sciences **374**, 20150248 (2016) (see p. 86).

[295] T. Hashizume, J. C. Halimeh, P. Hauke, and D. Banerjee, *Ground-state phase diagram of quantum link electrodynamics in* $(2+1)$*-d*, SciPost Phys. **13**, 017 (2022) (see p. 86).

[296] A. González-Tudela and J. I. Cirac, *Cold atoms in twisted-bilayer optical potentials*, Phys. Rev. A **100**, 053604 (2019) (see p. 87).

[297] J. Argüello-Luengo, A. González-Tudela, T. Shi, P. Zoller, and J. I. Cirac, *Analogue quantum chemistry simulation*, Nature **574**, 215 (2019) (see p. 87).

[298] G. Pagano, F. Scazza, and M. Foss-Feig, *Fast and Scalable Quantum Information Processing with Two-Electron Atoms in Optical Tweezer Arrays*, Advanced Quantum Technologies **2**, 1800067 (2019) (see pp. 87, 88).

[299] F. Gyger, M. Ammenwerth, R. Tao, H. Timme, S. Snigirev, I. Bloch, and J. Zeiher, *Continuous operation of large-scale atom arrays in optical lattices*, arXiv:2402.04994 (see p. 88).

[300] M. Brenes, M. Dalmonte, M. Heyl, and A. Scardicchio, *Many-Body Localization Dynamics from Gauge Invariance*, Phys. Rev. Lett. **120**, 030601 (2018) (see p. 88).

Acknowledgements

It has been an absolute pleasure and a great privilege to have spent the last four and a half years pursuing my PhD at the LMU among a wonderful group of friends and colleagues. First and foremost, my thanks goes to Monika Aidelsburger, for giving me the opportunity to take up my PhD in her group and for entrusting me with the responsibility of setting up a new experiment. Your enthusiasm and passion for this project won me over from day one. I am extremely grateful for all your support throught my PhD. Your openness and willingness to discuss all of my questions was greatly appreciated and always made me feel like I was free to explore and pursue my own ideas.

I also want to thank all the SQM team, past and present. Tim Höhn, who has been with me from the beginning and with whom I saw the lab transition from an empty room into the beautifully tangled mess of cables and wires it is today. Thank you for your support throughout our time together and your patience with me when things didn't go according to plan (usually involving a water leak of some sort). It's been a fun journey and I wish you all the best for the remainder of your PhD. To our newest PhD student René Villela. I've really enjoyed our brief time together as office mates and I'm happy to know that the lab is in good hands for the forseeable future. Thank you also for introducing me to the culinary delights of Tobasco sauce. I would also like to thank our new PostDoc Ronen Kroeze for bringing a new and critical eye to the lab, which led to many improvements. Thank you also for your willingness to discuss my thesis, or when that had run its course, cycling, cheese and baseball. A massive thank you goes to Nelson Darkwah Oppong, who spent a year as our first PostDoc during the early stages of the lab. Without your expertise and hard work this experiment would not have progressed half as quickly as it has. Your positive attitude really inspired me to give it my best and I am deeply appreciatve of your willingness to help at all times. To our Master students Daniel Adler, Martí Cladera, Dalila Robledo, David Gröters and Leonardo Bezzo, for all their wonderful contributions to the lab and the fun times spent in the lab. I also want to thank a number of very talented interns who have joined us over the years and contributed a number of vital technical systems to the lab. Tobias Marozsak, Guillaume Brochier and Semyon Zarutskiy. To everyone in the group at LMU and MPQ. It's been truly wonderful to get to know and work with so many talented, motivated and kind-hearted people over the years. Thank your for the camaraderie over countless lunch breaks and coffee conversations, and all your support throughout my PhD.

A very special thanks goes to all those who took the time to read and correct parts of my thesis. Ronen Kroeze, Nelson Darkwah Oppong, Oriana Dießel, Felix Palm, Lukas Homeier, Alex Impertro, Tim Höhn and Julian Wienand. It was incredibly helpful to get your feedback on various parts of my thesis.

I would also particularly like to thank the administrative staff and engineers at the LMU and MPQ. Ildiko Kecskesi for the fun conversations and her magic ability to handle all things administrative with ease so that we are free to pursue our research. Bodo Hecker and Reinhard Grottenthaler for helping with all things electronics related and for taking the time to explain things to a curious PhD student. Thank you also to all the staff at the LMU and MPQ workshop for their fine work over the years and especially to Anton Mayer for helping us with many mechanical designs in the early stages of our experiment.

To all those I am lucky enough to call my friends, both near and far. Thank you for sustaining me with interesting conversations, welcome distractions and your support througout. I owe all of you a deep debt of gratitude.

My final thanks goes to my family, for your encouragement and advice when the going got tough and for the love and support I experience every day.